Durham University

Durham E-Theses

An Examination of Subsidence in North-East England due to the Dissolution of Sub-Surface Gypsum using the Shallow Seismic Reflection Technique

Colin Sargent

How to cite:

Sargent, Colin (2009) An Examination of Subsidence in North-East England due to the Dissolution of Sub-Surface Gypsum using the Shallow Seismic Reflection Technique. Doctoral thesis, Durham University.

Use policy

The full-text may be used and/or reproduced, and given to third parties in any format or medium, without prior permission or charge, for personal research or study, educational, or not-for-profit purposes provided that:

- a full bibliographic reference is made to the original source
- a https://etheses.durham.ac.uk/id/eprint/1338/ is made to the metadata record in Durham E-Theses
- the full-text is not changed in any way

The full-text must not be sold in any format or medium without the formal permission of the copyright holders.

Please consult the full Durham E-Theses policy for further details.

Academic Support Office, The Palatine Centre, Durham University, Stockton Road, Durham, DH1 3LE
e-mail: e-theses.admin@durham.ac.uk Tel: +44 0191 334 6107
https://etheses.durham.ac.uk

An Examination of Subsidence in North-East England due to the Dissolution of Sub-Surface Gypsum using the Shallow Seismic Reflection Technique

By

Colin Sargent

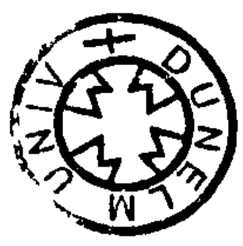
A thesis submitted in partial fulfilment of the requirements for the degree of Doctor of Philosophy

Department of Earth Sciences

Durham University
2009

Volume One

The copyright of this thesis rests with the author or the university to which it was submitted. No quotation from it, or information derived from it may be published without the prior written consent of the author or university, and any information derived from it should be acknowledged.



25 MAR 2009

Declaration

The content of this thesis are the original work of the author and has not previously been submitted for a degree at this or any other university. The work of other people is acknowledged by reference.

Colin Sargent
Durham University

Abstract

Along a narrow swath from Nottingham through to Hartlepool, broad shallow depressions up to 100m in diameter and, more rarely, scarp-edged subsidence hollows are observed. These topographical features coincide with the sub-crop of the Permian strata beneath the Quaternary deposits and are attributed to the dissolution of sub-surface gypsum. Boreholes (<150 m deep) prove the existence of several layers of gypsum within the Permian geological succession.

The objective of the work reported here is to image the shallow sub-surface geology at several locations in north-east England, and to detect any structures related to gypsum dissolution, such as faulting, foundering and voids. The purpose is to promote the use of the seismic reflection technique for site investigation to assess the subsidence hazard for new industrial and residential development.

A total of thirty-two 2D seismic profiles were acquired over a period of three years at seven different sites near to Darlington, Church Fenton and Ripon in County Durham and North Yorkshire. Based on the results of the 2D surveys and additional geological information, 3D seismic volumes were collected at three of the sites. The seismic source was a buffalo gun with the signal recorded by vertical geophones of 30 Hz resonant frequency. Raw data were collected in SEG-2 format on a 16-bit, 24-channel Geometrics SmartSeis recording system. Standard digital seismic data processing techniques were employed to transform the raw field data into interpretable seismic sections and volumes.

Gypsum beds between 5 m and 25 m thick are imaged at depths ranging from 30 m to 70 m below the reference datum, the water table. The processed seismic data show metre-scale detail of foundering features in shallow limestone beds overlying the gypsum beds. These features are interpreted as the consequence of gypsum dissolution, and many of them do not have a surface expression. Two mechanisms of gypsum dissolution are inferred from the relationships between the local geology, sub-surface foundering and the difference in seismic character of the gypsum surfaces: firstly, karstifaction of the upper gypsum surface by water percolating down through the overlying strata, and secondly, dissolution of the base of the gypsum bed by water flowing through an underlying artesian aquifer. However, no rectilinear maze cave systems within the gypsum beds were imaged.

3D seismic technology can delineate small areas different geological character that can be missed by a network of 2D seismic profiles, even when supplemented by boreholes.

Acknowledgements

Firstly, I would like to thank my supervisor Professor Neil Goulty for devising this interesting project, for helping out in the entire three seasons of field work and research guidance, and also for securing some monies for this project under the NERC Knowledge Transfer Programme, contract reference NE/D000955/1.

I am grateful to all the landowners, who granted permission for us to conduct seismic surveys on their land: Mr. Alan Fell at Hell Kettles, Mr. Nigel Swinbank at Neasham Fen, The Darlington Cattle Mart at Parkside, Mr. David Metcalffe at Hutton Hill, Mr. Dominic Dale at Sharow, Harrogate Borough Council at Ure Bank, and Mr. Carl Clayton at Ulleskelf Mires. Natural England also granted permission to acquire data at Hell Kettles and Neasham Fen, both designated Sites of Special Scientific Interest.

The keen interest in this research by Jim Gallagher and Stuart Muckle of Darlington Borough Council and the access to confidential borehole information granted by British Gypsum Limited were also very welcome.

I must thank Dr. Richard Hobbs for configuring the computing facilities to enable the processing of the raw 2D and 3D seismic data into geologically interpretable images. I am also grateful to Dave Stevenson and Gary Wilkinson for maintaining all of the Earth Sciences IT services, and to Alan Burchell who helped with maintenance of the SmartSeis seismograph.

The assistance of undergraduates in some of the field work, sometimes in rather inclement conditions, is very much appreciated. In particular I thank Will Kemp, Ahmed Al-Ghamdi, Ammar Balila, Emad Al-Matrafi, Saeed Al-Zahrani, Lucy Johnson and Peter Holt.

Contents

DECLARATION I

ABSTRACT II

ACKNOWLEDGEMENTS IV

CONTENTS V

LIST OF FIGURES IX

LIST OF TABLES XVII

1.0 INTRODUCTION 1

1.1 Synopsis 1

1.2 Motivation and objectives 2

1.3 Geophysical method selection 7

2.0 GEOLOGY 12

2.1 The Permian sequence in north-east England 12

2.2 Geology at Darlington 22

2.3 Geology at Church Fenton 27

2.4 Geology at Ripon 33

3.0 ACQUISITION 38

3.1 2D seismic acquisition parameters and survey design 38

3.2 3D seismic acquisition parameters and survey design 46

3.3 Fieldwork procedures and equipment 52
3.3.1 2D seismic profile and 3D seismic grid positioning 52
3.3.2 Source 53
3.3.3 Receivers and the roll-along switch 54
3.3.4 Seismograph 57

4.0 PROCESSING 60

4.1 ProMAX digital data processing software 60

4.2 Hell Kettles 2D seismic processing flow design 61
4.2.1 Pre-conditioning 63

4.2.2 Shot record polarity and filtering 66
4.2.3 Field statics 70
4.2.3.1 Plus-minus method 72
4.2.3.2 Field static calculations 74
4.2.3.3 Quality control of the field statics solution 79
4.2.4 Velocity analysis 79
4.2.5 Gain recovery 85
4.2.6 Noise muting on shot records 89
4.2.7 Improving the temporal resolution 90
4.2.8 Surface-consistent residual statics 95
4.2.9 Remnant noise suppression 99
4.2.10 Stack 102
4.2.11 Time migration 102

4.3 Hell Kettles 3D seismic processing 107

5.0 HELL KETTLES 113

5.1 Site description 113

5.2 Acquisition 119
5.2.1 Tests of seismic acquisition parameters 123
5.2.1.1 Comparison of single geophones and groups 123
5.2.1.2 Comparison of shallow and deep shots 130
5.2.1.3 Near-surface guided waves 135
5.2.1.4 Comparison of different size charges 139
5.2.1.5 Ground roll elimination by the stack array 144
5.2.1.6 Robustness of the field statics solution 146

5.3 Interpretation 148
5.3.1 Borehole tie line 148
5.3.2 The Seaham Formation and evidence for sub-surface gypsum 152
5.3.3 Sub-surface foundering 156
5.3.4 Analysis of the 3D seismic volume 166
5.3.5 Comparison of 2D/3D seismic imaging 171
5.3.6 Mechanisms of gypsum dissolution 175

6.0 PARKSIDE 178

6.1 Site description 178

6.2 Acquisition 183
6.2.1 Tests of seismic acquisition parameters 183
6.2.1.1 Comparison of different size charges 183

6.3 Processing 186

6.4 Interpretation 189
6.4.1 Reflections from the Permian formations 189
6.4.2 Shallow Intra-Quaternary reflections 199
6.4.3 Mechanisms of gypsum dissolution 200

7.0 NEASHAM FEN 204

7.1 Site description 204

7.2 Acquisition 210

7.3 Processing....212

7.4 Interpretation....215
7.4.1 Negative results on profile 02....215
7.4.2 Foundered geology....217
7.4.3 Mechanisms of gypsum dissolution....220

8.0 ULLESKELF MIRES....222

8.1 Site description....222

8.2 Acquisition....224

8.3 Processing....226

8.4 Interpretation....231
8.4.1 Brotherton Formation and sub-surface foundering....231
8.4.2 Evidence for sub-surface gypsum....238
8.4.3 Mechanisms of gypsum dissolution....243

9.0 URE BANK....245

9.1 Site description....245

9.2 Acquisition....248

9.3 Processing....252

9.4 Interpretation....256
9.4.1 Shallow reflections....256

10.0 HUTTON HILL....260

10.1 Site description....260

10.2 Acquisition and processing....262

10.3 Interpretation....267
10.3.1 Near surface refractors....267

11.0 SHAROW HALL....270

11.1 Site description....270

11.2 Acquisition....272

11.3 Processing....276

11.4 Interpretation....280
11.4.1 Sub-surface geology....280
11.4.2 3D Swath....285
11.4.3 Foundering....288

12.0 DISCUSSION AND CONCLUSIONS....291

12.1 Suggestions on improving the final outcome....291

12.2 Suggestions for improving the standard acquisition 296

12.3 Novelty, uses and further research 298

12.4 Comments on gypsum dissolution in the survey areas 299

12.5 A wider geographical view of karstic subsidence 301

12.6 Conclusions 307

13.0 REFERENCES 308

List of Figures

Figure 1.1: Subsidence hollows near Ripon, North Yorkshire. 3

Figure 1.2: Simplified geological map of England and Wales. 5

Figure 1.3: Gypsum caves at Houtsay, Cumbria. 6

Figure 2.1: Nomenclature and spatial distribution of the English Zechstein Cycles. 12

Figure 2.2: Palaeogeography of the EZ1 carbonate phase. 14

Figure 2.3: Palaeogeography of the EZ1 sulphate evaporite phase. 16

Figure 2.4: Distribution of the EZ3 evaporites. 18

Figure 2.5: Distribution of the EZ4 evaporites. 20

Figure 2.6: Sonic and natural gamma logs from the deep Seal Sands borehole. 21

Figure 2.7: Solid geology beneath Darlington. 23

Figure 2.8: Hurworth Place borehole geological succession. 25

Figure 2.9: Superficial deposits at Darlington. 26

Figure 2.10: Solid geology beneath Church Fenton 28

Figure 2.11: Ulleskelf Nurseries borehole geological succession 29

Figure 2.12: Superficial deposits at Church Fenton. 32

Figure 2.13: Solid geology beneath Ripon. 34

Figure 2.14: Superficial deposits at Ripon. 35

Figure 2.15: Burtree Park Caravan Site borehole geological succession. 37

Figure 3.1: Aerial photograph taken in 1988 of the Parkside survey site. 39

Figure 3.2: Geneva borehole geological succession. 39

Figure 3.3: Trial wave test at the Parkside survey site 40

Figure 3.4: Parkside survey 2D seismic profiles layout 45

Figure 3.5: Parkside 2D seismic profiles shooting template. 45

Figure 3.6: Final time migrated section of Parkside 2D profile 04. 47

Figure 3.7: Parkside 3D seismic volume layout. 48

Figure 3.8: Parkside 3D seismic volume shooting template. 49

Figure 3.9: Parkside 3D shot and receiver station layout. 51

Figure 3.10: Different shot trigger delays. 55

Figure 3.11: Effect of wind noise on shot record data quality. 56

Figure 3.12: Electrical cross-feed on a shot record caused by damp conditions..... 56

Figure 3.13: Picture montage of the field acquisition equipment. 58

Figure 4.1: ProMAX flow builder user interface. 61

Figure 4.2: Aerial photograph taken in 2000 of the Hell Kettles survey site..... 62

Figure 4.3: Hell Kettles 2D profile 04 shooting template. 63

Figure 4.4: Acquisition geometry QC stacking chart. 64

Figure 4.5: Brute stack. 65

Figure 4.6: North Oxen-le-Fields borehole geological succession..... 66

Figure 4.7: A selection of raw shot records. 67

Figure 4.8: Shot ensemble bandpass filter scan..... 68

Figure 4.9: Bandpass filtered stack..... 69

Figure 4.10: Bandpass filtered stack, expanded..... 71

Figure 4.11: Outline of the plus-minus refraction inversion method..... 72

Figure 4.12: First break picking..... 75

Figure 4.13: Computed plus and minus graphs..... 76

Figure 4.14: Extension of the plus-minus refraction inversion method. 77

Figure 4.15: Field statics stack. 78

Figure 4.16: Computed field static values for shots and receivers. 80

Figure 4.17: Near-trace field statics calculations QC plot. 81

Figure 4.18: ProMAX interactive velocity analysis. 83

Figure 4.19: Field statics stack with multiple point stacking velocity field. 84

Figure 4.20: Surface-consistent amplitude shot and receiver balancing near trace QC plot. . 86

Figure 4.21: Shot and receiver amplitude balanced stack..... 88

Figure 4.22: Surgical noise muting on shot ensembles..... 89

Figure 4.23: Noise mute stack. 90

Figure 4.24: Deconvolution type test panels on a single shot record. 92

Figure 4.25: Zero-phase spiking deconvolution stack..... 94

Figure 4.26:QC of the surface-consistent residual statics..... 96

Figure 4.27: Surface-consistent residual statics stack. 98

Figure 4.28:QC of the f-x deconvolution filtering on a CMP supergather..... 100

Figure 4.29: F-X deconvolution stack..... 101

Figure 4.30: Final stack. 103

Figure 4.31: Hell Kettles survey seismic data processing flow. 104

Figure 4.32: Final time migrated stack. 106

Figure 4.33: Hell Kettles 3D seismic volume shooting template. 108

Figure 4.34: Hell Kettles 3D seismic volume shot and receiver station layout. 109

Figure 4.35: Reduction of the acquisition footprint in 3D receiver statics. 111

Figure 4.36: Individual 3D Sub-line refraction velocities. 112

Figure 5.1: Superficial geology at the Hell Kettles survey site..... 114

Figure 5.2: Solid geology beneath the Hell Kettles survey site..... 115

Figure 5.3: Spatial distribution of 2D profiles and 3D volume at Hell Kettles. 116

Figure 5.4: Monk End borehole geological succession. 118

Figure 5.5: Surface depressions identified at Hell Kettles. 118

Figure 5.6: Variations in the geophone spreads used in the Hell Kettles 2D profiles. 120

Figure 5.7: Final migrated stack section for Hell Kettles profile 02. 124

Figure 5.8: Final migrated stack section for Hell Kettles profile 03. 125

Figure 5.9: Geophone array comparison: shot records from single and array geophone..... 126

Figure 5.10: Geophone array comparison: sections post field static corrections. 127

Figure 5.11: Geophone array comparison: final stacked sections. 128

Figure 5.12: Geophone array comparison: trial time migrated sections..... 129

Figure 5.13: Shallow and deep shot comparison. 131

Figure 5.14: Shallow and deep shot comparisons with bandpass filtering. 132

Figure 5.15: Shallow and deep shot comparisons with bandpass filtering. 133

Figure 5.16: Shallow and deep shot comparison with zero-phase spiking deconvolution. ... 134

Figure 5.17: Ground roll muted raw deep trial shot..... 136

Figure 5.18: Near-channel travel time graph. 137

Figure 5.19: A raw and bandpass filtered shot in dry ground from Hell Kettles profile 02. ... 138

Figure 5.20: A raw and bandpass filtered shot in wet ground from Hell Kettles profile 02.... 138

Figure 5.21: Raw shot charge size comparison at Hell Kettles. 141

Figure 5.22: Muted bandpass filtered shot charge size comparison at Hell Kettles. 142

Figure 5.23: Muted bandpass filtered shot charge size comparison at Hell Kettles. 143

Figure 5.24: Simulated stack array sections..... 145

Figure 5.25: Very brute stack section of Hell Kettles profile 05. 146

Figure 5.26: Stack sections of Hell Kettles profile 05 with varying amounts of additive noise. 147

Figure 5.27: Interpreted final migrated stack section of profile 07, the borehole tie line..... 150

Figure 5.28: Final stack section of Hell Kettles profile 07, the borehole tie line. 151

Figure 5.29: Interpreted final migrated stack section of Hell Kettles profile 08..... 153

Figure 5.30: Interpreted interactive velocity analyses from Hell Kettles profile 08. 154

Figure 5.31: Hell Kettles seismically interpreted geological succession. 155

Figure 5.32: Interpreted final migrated stack section of Hell Kettles profile 03..... 157

Figure 5.33: Interpreted final migrated stack section of Hell Kettles profile 01..... 158

Figure 5.34: Interactive velocity analysis at points on profiles 01 and 03. 159

Figure 5.35: Interpreted final migrated stack section of Hell Kettles profile 09..... 160

Figure 5.36: Interpreted final migrated stack section of Hell Kettles profile 11..... 161

Figure 5.37: Final stack section of Hell Kettles profile 05..... 162

Figure 5.38: Interpreted final migrated stack section of Hell Kettles profile 05..... 163

Figure 5.39: Interpreted final migrated stack section of Hell Kettles profile 06..... 164

Figure 5.40: Interpreted final migrated stack section of Hell Kettles profile 10..... 165

Figure 5.41: Interpreted final migrated stack section of Hell Kettles profile 16..... 166

Figure 5.42: Hell Kettles 3D top Seaham Formation horizon slice. 167

Figure 5.43: Top Seaham Formation horizon slice quadratic polynomial regression plot..... 168

Figure 5.44: Top Seaham Formation horizon slice difference plot. 169

Figure 5.45: Arbitrary time sections through the Hell Kettles 3D volume..... 170

Figure 5.46: Arbitrary time section through the Hell Kettles 3D seismic volume. 171

Figure 5.47: 2D and 3D comparison sections parallel to the silage field southern fenceline. 173

Figure 5.48: 2D and 3D comparison sections through the silage field shallow depression. . 174

Figure 5.49: Distribution of sub-surface foundering imaged at Hell Kettles. 176

Figure 5.50: A breccia pipe in cross-section..... 177

Figure 6.1: Aerial photograph taken in 1988 of the Parkside survey site..... 179

Figure 6.2: Superficial geology at the Parkside survey site..... 180

Figure 6.3: Solid geology beneath the Parkside survey site..... 181

Figure 6.4:Geneva borehole geological succession. 182

Figure 6.5: Shot charge size comparison at Parkside..... 184

Figure 6.6: Filtered and muted shot charge size comparison at Parkside. 185

Figure 6.7: Parkside survey seismic data processing flow..... 186

Figure 6.8: Shot record deconvolution type scan on Parkside data..... 187

Figure 6.9: Improvement in reflection continuity with surface-consistent residual statics..... 188

Figure 6.10: Bandpass filtered shot records from the Parkside survey profile 04. 189

Figure 6.11: Interpreted final migrated section of Parkside profile 04..... 191

Figure 6.12: Interpreted interactive velocity analysis at CMP 85 on Parkside profile 04. 192

Figure 6.13: Interpreted final migrated section of Parkside profile 01..... 193

Figure 6.14: Interpreted final migrated section of Parkside profile 02..... 194

Figure 6.15: Interpreted final migrated section of Parkside profile 03..... 195

Figure 6.16: Parkside 3D in-line-profile stack and time migrated comparison. 196

Figure 6.17: Parkside 3D top Ford Formation horizon slice. 196

Figure 6.18: Parkside 3D top Hartlepool Anhydrite Formation horizon slice. 197

Figure 6.19: Thickness variation of the Edlington Formation over the Parkside 3D volume. 198

Figure 6.20: Interactive velocity analysis centred at CMP 35 on Parkside profile 04. 199

Figure 6.21: Top Hartlepool Anhydrite horizon slice quadratic polynomial regression plot... 201

Figure 6.22: Top Hartlepool Anhydrite horizon slice difference plot. 202

Figure 6.23: A series of in-line sections through the Parkside time migrated 3D volume..... 203

Figure 7.1: Aerial photograph taken in 2000 of the Neasham Fen survey site..... 205

Figure 7.2: Panoramic view to the north-west across Neasham Fen. 205

Figure 7.3: Shallow corings across Neasham Fen. 206

Figure 7.4: Neasham borehole geological succession..... 207

Figure 7.5: Solid geology beneath the Neasham Fen survey site. 208

Figure 7.6: Superficial geology at the Neasham Fen survey site. 209

Figure 7.7: Ordnance Survey map of Neasham Fen. 210

Figure 7.8: Neasham Fen 2D seismic profiles shooting template..... 212

Figure 7.9: Raw and bandpass filtered shots from Neasham Fen profile 03. ..... *213*

Figure 7.10: The effect of AGC shot balancing on the Neasham Fen data..... *214*

Figure 7.11: Neasham Fen survey seismic data processing flow..... *215*

Figure 7.12: Raw shots from Neasham Fen profile 02..... *216*

Figure 7.13: Interpreted final time migrated section of Neasham Fen profile 03...... *218*

Figure 7.14: Interpreted final time migrated section of Neasham Fen profile 01...... *219*

Figure 7.15: The Macksville Sinkhole, Kansas. *221*

Figure 8.1: Aerial photograph taken in 1976 of the Ulleskelf Mires survey site...... *222*

Figure 8.2: Superficial geology at the Ulleskelf Mires survey site..... *223*

Figure 8.3: Ulleskelf Mires wave test shot record. *225*

Figure 8.4: Ulleskelf Mires 2D profiles shooting template. *225*

Figure 8.5: Near-trace field statics quality control...... *227*

Figure 8.6: Shot record field statics quality control. *228*

Figure 8.7: Raw shots from different shooting mediums along Ulleskelf Mires profile 03..... *229*

Figure 8.8: Shots records in different shooting mediums bandpass filtered..... *229*

Figure 8.9: Deconvolution shot record test panels from Ulleskelf Mires profile 01...... *230*

Figure 8.10: Ulleskelf Mires survey seismic data processing flow...... *231*

Figure 8.11: Interpreted final time migrated section of Ulleskelf Mires profile 02. ..... *232*

Figure 8.12: Solid geology beneath the Ulleskelf Mires survey site..... *233*

Figure 8.13: BHP 71 and 72 boreholes geological successions..... *234*

Figure 8.14: Interpreted final time migrated section of Ulleskelf Mires profile 01. ..... *236*

Figure 8.15: Interpreted final time migrated section of Ulleskelf Mires profile 03. ..... *237*

Figure 8.16: Aerial photograph taken in 1974 of the western half of Ulleskelf Mires...... *238*

Figure 8.17: Interpreted final time migrated section of Ulleskelf Mires profile 04. ..... *239*

Figure 8.18: BHP 73 and 74 boreholes geological successions..... *240*

Figure 8.19: Interpreted final time migrated section of Ulleskelf Mires profile 05. ..... *242*

Figure 8.20: Interpreted Ulleskelf Mires processed shot records..... *243*

Figure 9.1: Aerial photograph taken in 1994 of the Ure Bank survey site...... *246*

Figure 9.2: River Ure Floodplain borehole geological succession...... *247*

Figure 9.3: Ure Bank 2D profiles 01 and 02 shooting template...... *248*

Figure 9.4: Ure Bank 2D profiles 03, 05 and 06 shooting template. 251

Figure 9.5: Typical shot record from Ure Bank profile 01. 253

Figure 9.6: Stack section of Ure Bank profile 01. 254

Figure 9.7: Bandpass filtered shot records from Ure Bank profile 05. 255

Figure 9.8: Ure Bank survey seismic data processing flow. 255

Figure 9.9: Final stack section of Ure Bank profile 05. 257

Figure 9.10: Interpreted final time migrated section of Ure Bank profile 05. 258

Figure 10.1: Ordnance Survey map of Hutton Hill. 260

Figure 10.2: Aerial photograph taken in 1972 of the Hutton Hill survey site. 261

Figure 10.3: Hutton Hill borehole geological succession. 262

Figure 10.4: Hutton Hill 2D seismic profiles shooting template. 263

Figure 10.5: Raw and bandpass filtered Hutton Hill shot records. 265

Figure 10.6: Stack section of Hutton Hill profile 01. 266

Figure 10.7: Raw shots from Hutton Hill. 266

Figure 10.8: First break intercept-time graph. 268

Figure 10.9: Adjusted first break intercept-time graph. 269

Figure 11.1: Historical Ordnance Survey maps of Sharow Cross. 270

Figure 11.2: Superficial deposits at the Sharow Hall survey site. 271

Figure 11.3: Aerial photograph taken in 1994 of the Sharow Hall survey site. 272

Figure 11.4: Sharow Hall borehole geological succession. 273

Figure 11.5: Sharow Hall wave test shot record. 274

Figure 11.6: Sharow Hall 2D seismic profiles shooting template. 274

Figure 11.7: Ordnance Survey map of Sharow Hall. 276

Figure 11.8: Sharow Hall 3D seismic volume shooting template. 277

Figure 11.9: Shot coupling comparison on data from Sharow Hall 2D profile 02. 279

Figure 11.10: Sharow Hall survey seismic data processing flow. 280

Figure 11.11: Interpreted final time migrated section of Sharow Hall profile 02. 282

Figure 11.12: Solid geology beneath the Sharow Hall survey site. 283

Figure 11.13: Ripon Parks Cliff geological succession. 284

Figure 11.14: Interpreted final time migrated section of Sharow Hall profile 01. 285

Figure 11.15: Raw shots from Sharow Hall 3D sub-line profile 01. ..... *286*

Figure 11.16: Filtered raw shots from Sharow Hall 3D sub-line profile 01. ..... *287*

Figure 11.17: Comparison of 2D and 3D receiver statics solution. *288*

Figure 11.18: Ordnance Survey map overlaid on 1994 aerial photograph of Sharow Hall. .. *289*

Figure 11.19: Contorted bedding at Ripon Parks. *289*

Figure 11.20: Sharow Hall historic Ordnance Survey maps and aerial photographs. *290*

Figure 12.1: Large mechanical rig for drilling shot holes. *293*

Figure 12.2: Extreme variable source statics along Ulleskelf Mires profile 03. ..... *297*

Figure 12.3: Outcrop distribution of rocks prone to karst across the United Kingdom. *302*

Figure 12.4: Major basinwide evaporite deposits. *304*

Figure 12.5: Comparison of aerial extent of Quaternary and ancient evaporite deposits. *304*

Figure 12.6: World distribution of potential carbonate karst. *306*

List of Tables

Table 1.1: Geographical positions of the survey sites..... 11

Table 2.1: Summary of the general geological succession at Darlington. 24

Table 2.2: Summary of the general geological succession at Church Fenton. 30

Table 2.3: Summary of the general geological succession at Ripon. 36

Table 3.1: Parkside 2D profiles acquisition parameters..... 46

Table 3.2: Parkside 3D seismic volume acquisition parameters. 50

Table 4.1: Shot record bandpass filter design. 70

Table 4.2: Deconvolution design..... 95

Table 5.1: Hell Kettles 2D profiles initial acquisition parameters. 121

Table 5.2: Hell Kettles 3D seismic volume acquisition parameters. 122

Table 7.1: Neasham Fen 2D profiles acquisition parameters..... 211

Table 8.1: Ulleskelf Mires 2D profiles acquisition parameters. 226

Table 9.1: Ure Bank 2D profiles initial acquisition parameters. 249

Table 9.2: Ure Bank 2D profile 03 acquisition parameters..... 250

Table 10.1: Hutton Hill 2D profiles acquisition parameters..... 264

Table 11.1: Sharow Hall 2D profiles acquisition parameters..... 275

Table 11.2: Sharow Hall 3D seismic volume acquisition parameters. 278

Table 12.1: World carbonate outcrop area. 305

1.0 Introduction

1.1 Synopsis

Chapter 1 outlines the aims and reasons for this geophysical study of sub-surface gypsum dissolution with an explanation why the investigative technique of choice was the seismic reflection method. Chapter 2 describes the general solid and drift geology in the Darlington, Ripon and Church Fenton areas, where the seismic reflection surveys were acquired. Particular emphasis is placed on the geology of the Permian System in north-east England. Using the Parkside survey site south of Darlington, the data acquisition fieldwork procedures are addressed in chapter 3. Factors that influence the seismic survey design and the effect of the local environmental conditions on the quality of the raw data are considered. Chapter 4 concentrates on digital data processing of the raw shot records through to a time migrated 2D section or 3D volume, the final interpretable image of the sub-surface geology. Using a single 2D profile from the Hell Kettles site near Darlington, each step of the processing sequence is discussed in detail. Chapters 5 through to 11 present the results and geological interpretation of the seismic data at each of the seven survey sites. Possible mechanisms for sub-surface gypsum dissolution are discussed. Conclusions are drawn from the complete body of the project in chapter 12 along with recommendations for future work.

UNIV DURHAM

1.2 Motivation and objectives

Throughout historic times, the eastern side of the City of Ripon, North Yorkshire (Figure 1.1), Ordnance Survey National Grid Reference [SE 310 710], has suffered from active subsidence, including sudden catastrophic events, and so has been the subject of a number of scientific papers and technical reports (Cooper, 1986; Cooper, 1989; Patterson et al., 1995; Thompson et al., 1996; Cooper and Waltham, 1999). Cooper (1986) has researched the historical records from the beginning of 19th Century to chronologically and spatially map the major subsidence events in the vicinity of Ripon, and estimated that subsidence events occur at Ripon at an average rate of one every 3 or 4 years, over an area of more than 30 km^2.

Many shallow sub-circular depressions in the greenbelt to the south and east of Darlington, County Durham [NZ 290 150] have been recorded (Thompson et al., 1996). Subsidence activity in the vicinity of Darlington is quiescent compared to Ripon with the Hell Kettles ponds [NZ 2815 1085] being the only example of sudden collapse sinkholes in the Darlington area.

A few hundred metres to the north of the village of Church Fenton, North Yorkshire [SE 510 370], a swarm of shallow hollows spreads over an area of approximately 2 km^2 (Thompson et al., 1996).

The morphology of ground subsidence at Darlington, Ripon and Church Fenton can be broadly divided into two categories (Figure 1.1). A steep-sided chimney collapse structure is formed where a cylindrical volume of competent rock mass has fallen into a void. Features of this type can occur without warning and are found where the overburden is thin. Where the drift cover is thick, the process of chimney collapse subsidence in the bedrock is the same, but a sub-circular conical depression with diffuse edges is produced at the ground surface as a consequence of the plastic overburden sloughing into the void.

Deep borehole records show that areas of Darlington, Ripon and Church Fenton are underlain by substantial beds of gypsum embedded within the Permian strata of north-east England. Gypsum is an evaporite mineral, the hydrated form of calcium sulphate ($CaO_4.2H_20$), and is readily soluble in water. Laboratory experiments indicate that gypsum is dissolved about 100 times more rapidly than limestone (e.g., Klimchouk, 2000a). The dissolution of a large block of gypsum that fell into the River Ure at Ripon Parks, North

Yorkshire [SE 3088 7513], the only location in England where gypsum is exposed at the surface naturally, was monitored by James et al. (1981) who found that the rate of dissolution of gypsum from the field observations agreed well with the experimental values.



Figure 1.1: Subsidence hollows near Ripon, North Yorkshire.
The upper frame is a sudden collapse of a cylindrical volume of Sherwood Sandstone. The diameter of the shaft is 15 m. The lower frame shows a couple of conical depressions. Both views are from Thompson et al. (1996).

The majority of the surface depressions in the districts of Darlington, Ripon and Church Fenton are attributed to sub-surface dissolution of gypsum. The potential for gypsum karstification and foundering is constrained to a narrow strip a few kilometres wide on the feather edge of the easterly dipping Permian outcrop (Figure 1.2). This narrow strip runs northwards from Nottingham up to Darlington in County Durham, and then curves round to Hartlepool on the North Sea coast.

Lamont-Black et al. (2002) have proposed eight different possible causes of subsidence that may be present in an area underlain by gypsiferous rocks. These include downwashing of overlying unconsolidated sediments into karstic voids, gradual collapse of unconsolidated materials overlying gypsum karst, and sudden collapse of materials into voids. Some of the proposed mechanisms producing shallow depressions do not involve the dissolution of the gypsum beds, such as clay shrinkage due to localised desiccation by large trees. Peat can undergo autocompaction (Hobbs, 1986), lowering the ground surface locally. Clusters of annular surface depressions may be relict features from Late Pleistocene ground ice. The precise interpretation of these relict features is not always clear and may range from collapsed pingos, palsas and lithalsas to sub-glacial or supra-glacial processes (Harris and Ross, 2007). In north-east England, surface hollows may be WWII bomb craters (pers. comm. J. Gallagher, Darlington Borough Council).

From analysis of the orientation of the long axes of hollows around Ripon, it has been hypothesised that a network of caves exists within the gypsum beds (Powell et al., 1992; Cooper and Waltham, 1999). Direct observations of a cave system in gypsum in England have been provided by mining activities at Houtsay, Cumbria (Ryder and Cooper, 1993), where the diameters of the major conduits were of the order of 1 m (Figure 1.3) and aligned to the main joint directions within the gypsum bed. The gypsum cave systems studied in England are very small compared to the vast multi-storey rectilinear gypsum maze caves found in the Western Ukraine (Klimchouk, 2000b). So far, 203 km of passages have been mapped in the largest of several Ukrainian cave systems, Optimistichekaja.

Breccia pipes associated with surface depressions are well known in the Ripon area (Patterson et al., 1995) and are probably the remains of the upward migration of cavities.

Whether individual pipes tend to be located above the intersections of linear caves is open to debate (Cooper and Waltham, 1999).

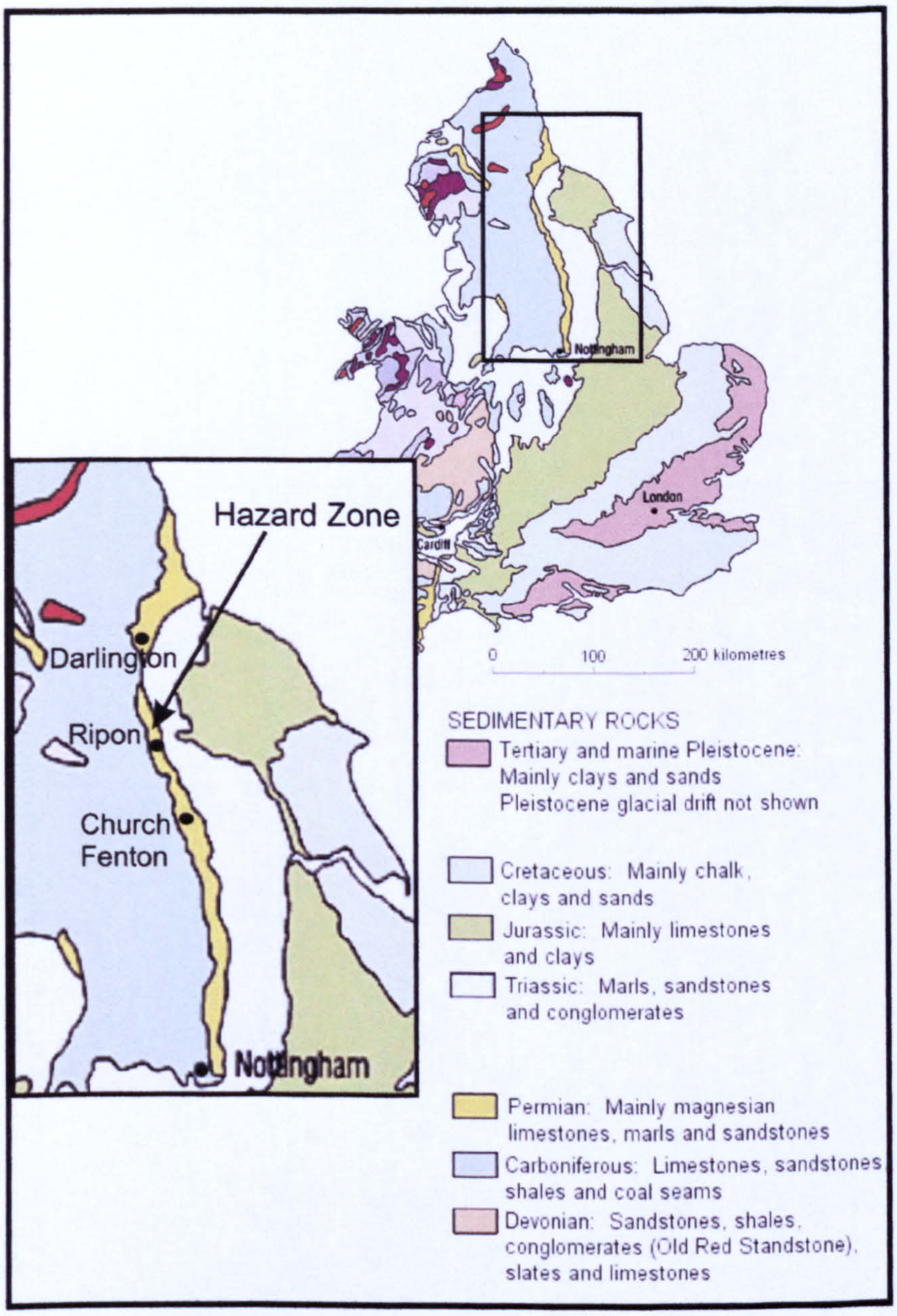
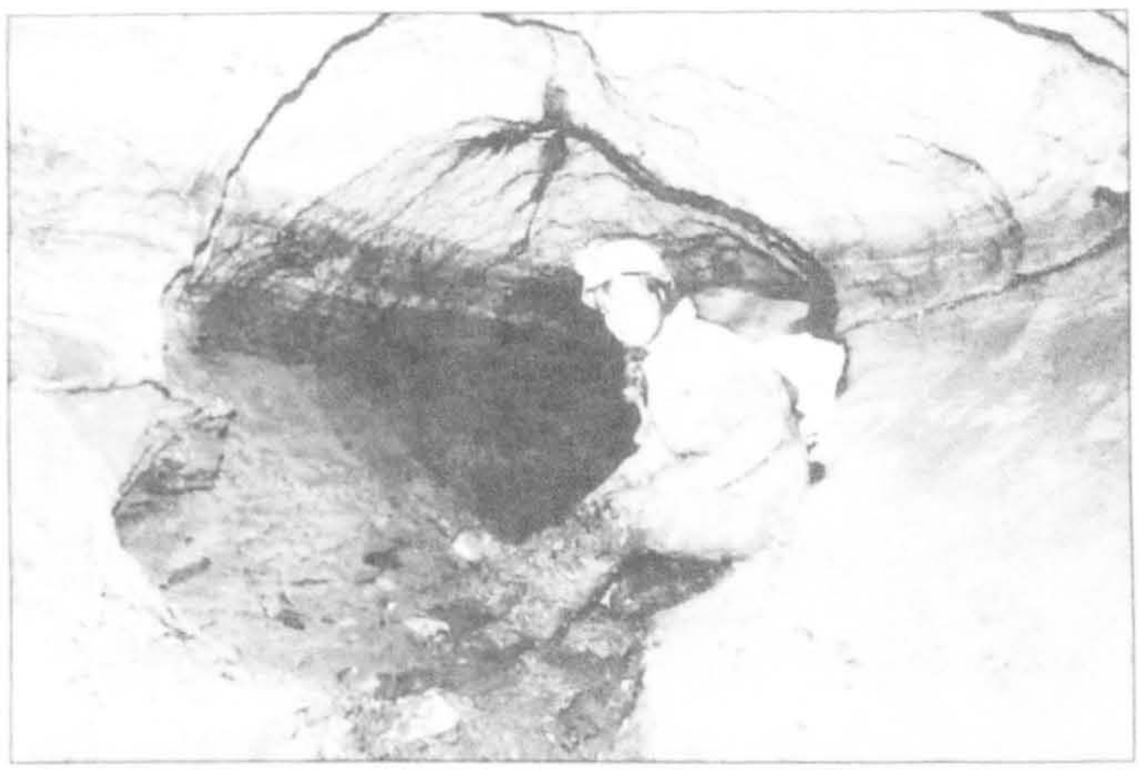


Figure 1.2: Simplified geological map of England and Wales.
The inset shows the extent of north-east England Permian gypsum dissolution hazard zone, and the three areas of investigation reported in this thesis. North is at the top of the map. Map adapted from an original by the British Geological Survey © NERC 1995.



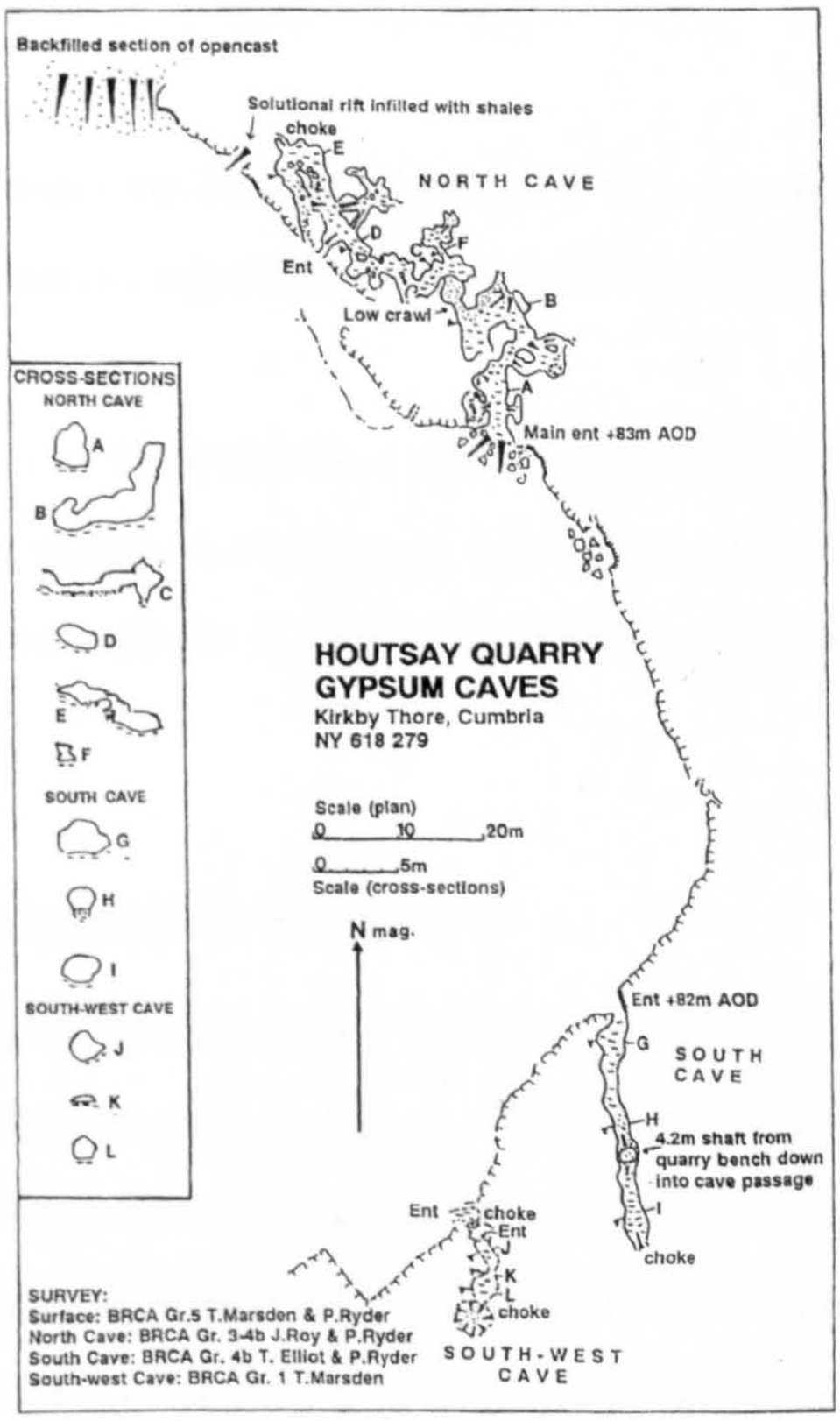


Figure 1.3: Gypsum caves at Houtsay, Cumbria.
Map and photograph are extracted from Ryder and Cooper (1993).

This thesis reports the seismic reflection results from work supported by the Natural Environment Research Council, which awarded a grant for "Location of gypsum dissolution cavities by seismic reflection surveying" to Durham University under its Knowledge Transfer scheme. The main objectives for this research, as described in the grant proposal, were two-fold:

(1) To image sub-surface geological structures that are related to gypsum dissolution, in particular air-filled or water-filled voids that may be an indication of the existence of a rectilinear maze cave system, foundering of geological strata, and faults that might act as routes for the passage of water.

(2) To promote the seismic reflection method as a technique that should be considered by the civil engineering community for use in site investigation.

It is shown in the thesis that the seismic reflection surveys have produced good evidence of foundering of strata above gypsum beds, but the seismic data have not provided evidence for linear cave systems or other dissolution cavities within the gypsum beds themselves.

1.3 Geophysical method selection

Microgravity surveying has been employed successfully in the detection and mapping of karstic terrains and man-made cavities (Styles et al., 2005; Debeglia et al., 2006), including a time lapse project (Branston and Styles, 2003) which monitored an upward progressing body over a period of three years. Rybakov et al. (2001) modelled the gravity anomaly due to a spherical air-filled cavity in unconsolidated alluvial fan deposits. A void of effective radius of 11 m and density contrast of 1.8 g cm^{-3} cannot be detected if its depth is greater than 40 m. If the cavity is water-filled, with approximate density contrast of 0.8 g cm^{-3}, it cannot be detected if its depth is greater than 30 m. The computations assumed a gravity station spacing of 5 m, and a meter accuracy of better than 0.005 mgal.

The alternative potential field method, micromagnetics, can also be discounted, because the sedimentary rocks at the Parkside survey sites have very low magnetic susceptibility, and therefore will not appreciably perturb the main magnetic field.

Ground penetrating radar (GPR) is a relatively recent non-invasive geophysical tool. The raw radar records are digitally processed in a similar manner to seismic reflection data to produce 2D images and 3D volumes of the near-surface geology. Ground penetrating radar has been successful in mapping faults (Tronicke et al., 2006) and voids (Chamberlain et al., 2000), geological features that are often associated with gypsum dissolution, and Daniels (1988) refers to the presence of lava tubes in Hawaiian dry basalt identified by hyperbolic diffractions in a GPR traverse. Field experiments have shown that very fine lateral and vertical sedimentological details could be distinguished down to a depth of 18 m depth with a 400 MHz input signal, increasing to 66 m with an antenna emitting a 12.5 MHz pulse (Smith and Jol, 1995). The test site used for these experiments was a quarry in very clean, quartzose-rich, thick, clastic sediments of low electrical conductivity, ideal conditions for the propagation of the radar signal. However, where thick beds of clays and silts are present combined with a shallow water table, the high electrical conductivity rapidly attenuates the radar signal, decreasing penetration (Benson, 1995).

Electrical resistivity is a popular non-invasive geophysical technique capable of a high speed of execution. Electrical anomalies are generated by the high resistivity contrast that exists between an air-filled cavity and the surrounding country rock. The maximum depth of a detectable empty cave in a perfectly homogeneous medium is approximately four times its diameter (Santos and Afonso, 2005). Detectablility of caves is reduced in areas of complex geology, such as karstic terrains. The technique has been extended as tomographic approach and applied in civil engineering and archaeology to determine the size and depth to voids (van Schoor, 2002; Cardarelli et al., 2006). High resolution is proven with electrical resistivity tomography, but only at shallow depths, generally less than 20 m.

Electromagnetic profiling used in conjunction with a magnetometer survey is an extremely powerful approach to mine shaft detection (McCann et al., 1982). The depth of penetration of the conductivity method is limited by the design of the equipment used. The Geonics EM-31 has a nominal depth of investigation of 6 m, whilst the larger coil spacing of

the EM-34 system enabled the slip-surface of a landslide along a gypsum layer at 50 m depth to be imaged (Bruno and Marillier, 2000); but this method does not have the resolving power to image small scale geological details at depths of 50 m or more.

The use of surface waves to map and characterize the near-surface layers is a recent innovation (Park et al., 1999; Miller et al., 1999). Multi-channel surface wave (MASW) analysis transforms the surface wave portion of a raw shot record into a dispersion curve of phase velocity versus frequency. The dispersion curves of the surface waves may be inverted to estimate the depth structure of the shear wave velocity. Debeglia et al. (2006) gathered all the depth to shear-wave profiles into sequential order to produce a 2D contour plot of the shear-wave velocity field delineate the extent of karstic terrains. This study provided stacked surface wave and shear wave velocity sections with sufficient resolution to interpret zones of karstified and fractured mechanically weak rock. The penetration of surface waves is approximately equal to their wavelength, while the maximum depth that the MASW method can image is about half the longest wavelength measured (Ismail and Anderson, 2007). The usable frequency bandwidth of 15 Hz to 100 Hz equates to a depth range of investigation around 1 m to 20 m.

Seismic refraction datasets are used in the computation of statics corrections to negate the effect of near-surface deposits in seismic reflection surveys. Refraction inversion algorithms such as the plus-minus method (Hagedoorn, 1959) and its extension, the generalised reciprocal method (GRM) (Palmer, 1981), are often employed to delineate the contours at rockhead in environmental and geotechnical studies. By making adjustments for geometric spreading and smoothing out very near-surface inhomogeneities of limited lateral extent, Palmer (2006) has further refined the GRM approach to improve the lateral resolution of the method. The refraction convolution section (Palmer, 2001) in some cases can produce a clearer image of the near-surface geology than seismic reflection profiling (de Franco, 2005). The seismic refraction method is also capable of mapping faulting within a rock mass, if the there is sufficient contrast in the lithology either side of the fault (Goulty and Brabham, 1984). But location of voids using the seismic refraction method is unlikely except where the cavity is close to the surface (McCann et al., 1987).

The seismic reflection method is designed to detect interfaces between rock layers. The amplitude of the reflection depends on the acoustic impedance contrast at an interface. The technique has already been applied to problems relating to gypsum, particularly imaging abandoned mine workings (Kourkafas and Goulty, 1996; Piwakowski et al., 1997; Grandjean et al., 2002). It has also proved to be successful in the location and delineation of near-surface faults (Demanet et al., 2001) and voids (Branham and Steeples, 1988) and for detailed mapping of the topography of shallow reflective boundaries (Brabham et al., 1999; Francese et al., 2005). In good conditions, high-frequency seismic signals in the range 100 Hz to 200 Hz can penetrate to depths of the order of 100 m (Büker et al., 1998; Francese et al., 2005).

A seismic P-wave with a dominant frequency of 200 Hz propagating in rock with P-wave interval velocity of 2000 m s^{-1} has a dominant wavelength of 10 m. These values are typical of a near-surface environment and give a vertical resolution of 2.5 m, based on the classic wedge model experiment of Kalweit and Wood (1982). A horizontal resolution of one-quarter of a wavelength, 2.5 m, is also feasible post-migration (Lindsey, 1989). The presence of small objects or voids in the strata such as conduits within gypsum beds, or discontinuities within the strata due to faults or foundering may be recognised in the unmigrated stacked seismic sections as diffraction events.

After scrutiny of a Department of the Environment technical report (Thompson et al., 1996), British Geological Survey (BGS) databases and Ordnance Survey maps, and visits to prospective sites, seven sites in the vicinity of shallow depressions were identified in the neighbourhood of Darlington, Church Fenton and Ripon (Table 1.1) to investigate the effects of sub-surface gypsum dissolution.

Ultra-shallow seismic reflections have been reported in the scientific literature (Baker et al., 1999). However, due to shot-generated noise, seismic reflections at most sites are only visible at depths greater than 25 m. So where sub-surface geological structures are thought to be at depths of less than 25 m, potential field, electrical, radar and surface wave analysis may be more appropriate geophysical survey methods than seismic reflection because they have high resolution capability in this depth range.

Site	District	National Grid Reference
Hell Kettles	Darlington	NZ 2815 1085
Parkside	Darlington	NZ 2992 1289
Neasham Fen	Darlington	NZ 3315 1155
Ulleskelf Mires	Church Fenton	SE 5195 3844
Ure Bank	Ripon	SE 3164 7332
Hutton Hill	Ripon	SE 3288 7248
Sharow Hall	Ripon	SE 3332 7175

Table 1.1: Geographical positions of the survey sites.

All of the available information indicates that the target gypsum beds are present at 30 m to 80 m below the ground surface at the selected survey sites, with a thick sequence of unconsolidated Quaternary deposits and a shallow water table except at Hutton Hill. Therefore, the environmental and geological constraints suggest that the seismic reflection method is the most suitable geophysical tool to investigate gypsum dissolution at these sites.

All of the selected sites are green field sites. However, with the development of the land-streamer (Van der Veen and Green, 1998, Van der Veen et al., 2001) the acquisition of shallow seismic reflection data is now possible in urban areas.

2.0 Geology

2.1 The Permian sequence in north-east England

The modern classification, nomenclature, correlation and spatial relationships of the English Permian formations (Figure 2.1) are founded on the work of Smith et al. (1986) and are correlated to Permian rocks across northern Europe.

GROUPS	Cycles	YORKSHIRE PROVINCE (OUTCROP AREA)	DURHAM PROVINCE (County Durham, east Tyne and Wear, County Cleveland)	YORKSHIRE PROVINCE (East and North Yorks and Humberside)	NORTH GERMANY AND HOLLAND	Cycles
ESKDALE GROUP	EZ5	ROXBY FORMATION	ROXBY FORMATION	LITTLEBECK ANHYDRITE SLEIGHTS SILTSTONE	OHRE ANHYDRIT UNTERER OHRE TON	Z5
STAINTON-DALE GROUP	EZ4	SHERBURN ANHYDRITE UPGANG FORMATION ROTTEN MARL	SHERBURN ANHYDRITE UPGANG FORMATION ROTTEN MARL	SNEATON HALITE SHERBURN ANHYDRITE UPGANG FORMATION CARNALLITIC MARL	ALLER SALZE PEGMATITANHYDRIT Thin unnamed carbonate ROTER SALZTON	Z4
TEESSIDE GROUP	EZ3	BILLINGHAM ANHYDRITE BROTHERTON FM	BOULBY HALITE BILLINGHAM ANHYDRITE SEAHAM FORMATION	BOULBY HALITE BILLINGHAM ANHYDRITE BROTHERTON FORMATION GRAUER SALZTON	LEINE SALZE HAUPTANHYDRIT PLATTENDOLOMIT GRAUER SALZTON	Z3
AISLABY GROUP	EZ2	EDLINGTON FORMATION	SEAHAM RESIDUE ROKER DOLOMITE AND CONCRETIONARY LIMESTONE	FORDON EVAPORITES KIRKHAM ABBEY FORMATION	STASSFURT SALZE & BASALANHYDRIT HAUPTDOLOMIT AND EQUIVALENTS	Z2
DON GROUP	b EZ1 a	Sprotbrough Member / Wetherby Member } CADEBY FORMATION MARL SLATE	HARTLEPOOL ANHYDRITE FORD FORMATION RAISBY FORMATION MARL SLATE	HAYTON ANHYDRITE CADEBY FORMATION MARL SLATE	WERRAANHYDRIT ZECHSTEINKALK KUPFERSCHIEFER	Z1
		BASAL PERMIAN (YELLOW) SANDS AND BRECCIAS	YELLOW (BASAL PERMIAN) SANDS AND BRECCIAS	BASAL PERMIAN SANDS AND BRECCIAS	ROTLIEGENDES	

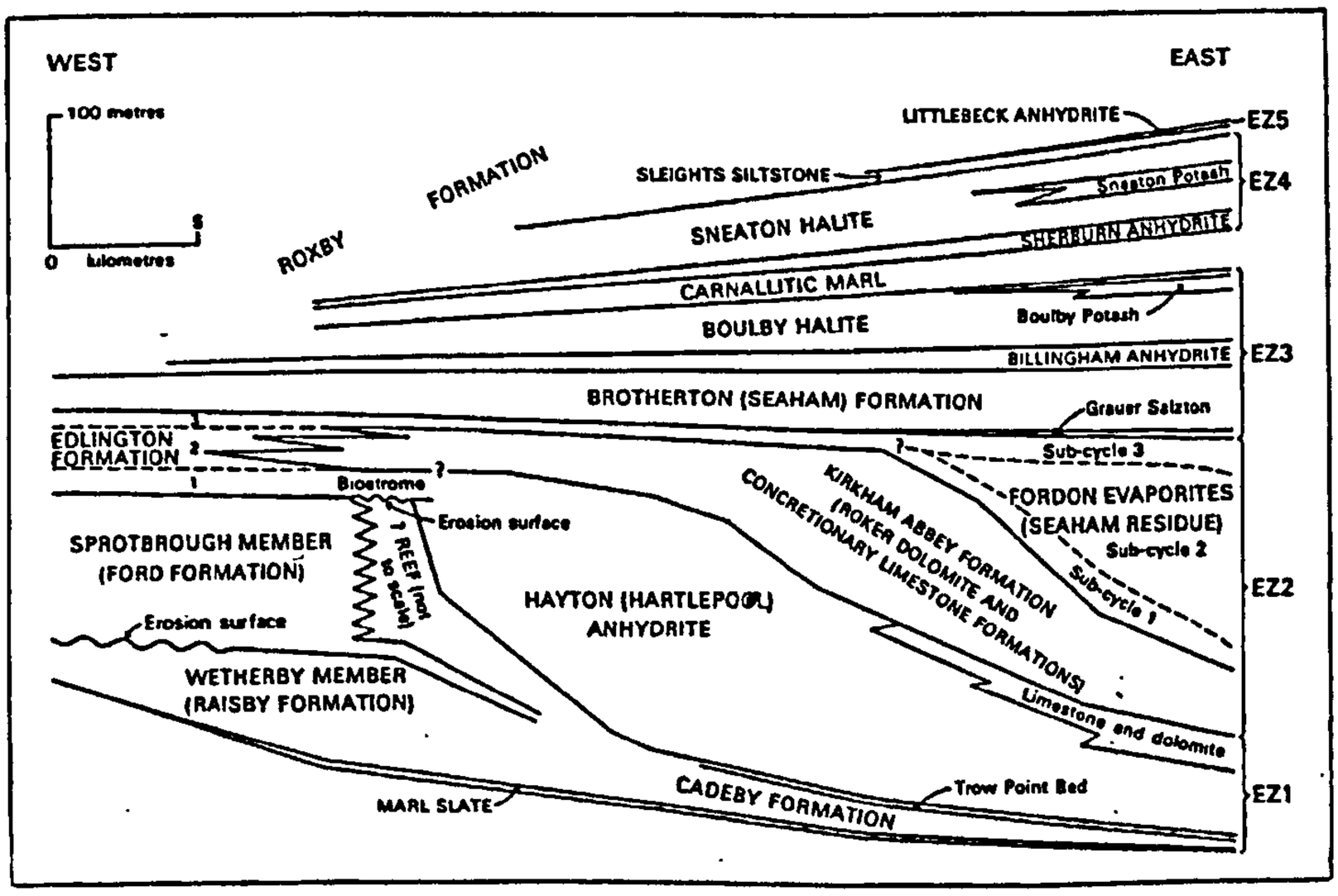


Figure 2.1: Nomenclature and spatial distribution of the English Zechstein Cycles. Diagrams extracted from Smith (1989).

As a consequence of uplift during the final phases of the Hercynian Orogeny (Anderton et al., 1983), a landscape unconformity exists between the Carboniferous and Permian formations. The base of the Permian sequence in north-east England is represented by a thin bed of weakly cemented sands and gravels. These deposits are thought to be the remains of aeolian sand dunes and gravel spreads on a rocky piedmont. The piedmont formed part of the Pangaea super-continent at latitude of around 20 °N, equivalent to Saudi Arabia today, which was experiencing a hot arid climate (Anderton et al., 1983).

The block-faulted basement of the desert environment gradually underwent subsidence, creating a basin below mean sea level. An organic-rich thin bed of Marl Slate lies at the base of the first English Zechstein Cycle, EZ1, probably laid down in quiet, anoxic conditions in a marine environment (Sweeney et al., 1987). The barrier protecting the intra-continental depression was probably breached from the north to create the inland Zechstein Sea. It has been postulated that the initial marine transgression was a consequence of deglaciation in Gondwanaland (Anderton et al., 1983).

Marine life colonised the warm tropical waters of the Zechstein Sea. Massive reefs, gradually constructed on the western edge of the basin, constitute the carbonate phase of EZ1 (Figure 2.2). In the Durham Province of the English Permian stratigraphy, the dolomitized reefs form the Raisby and Ford limestone formations, with a combined maximum thickness of 200 m along a north-south belt in eastern County Durham. The Ford Formation has two main facies, reef and back-reef. The back-reef facies mainly comprises of oolites, whilst the reef facies is constructed of a bryozoan framework less than 800 m wide. Further south, these reefal formations are represented by the dolomitic limestone Cadeby Formation. The Cadeby reaches 100 m thickness east of the outcrop, thinning eastwards and southwards towards the limit of deposition of Permian rocks, along a line from Nottingham to the Wash. At outcrop, the Cadeby Formation can be divided into two members divided by an erosional surface, the Hampole Discontinuity, possibly caused by a period of sub-aerial emergence. The lower Wetherby Member is interpreted as a shallow water carbonate deposit in a semi-restricted lagoon, whilst the upper Sprotbrough Member is mainly oolitic, suggesting a quiet lagoonal environment (Cooper and Burgess, 1993).

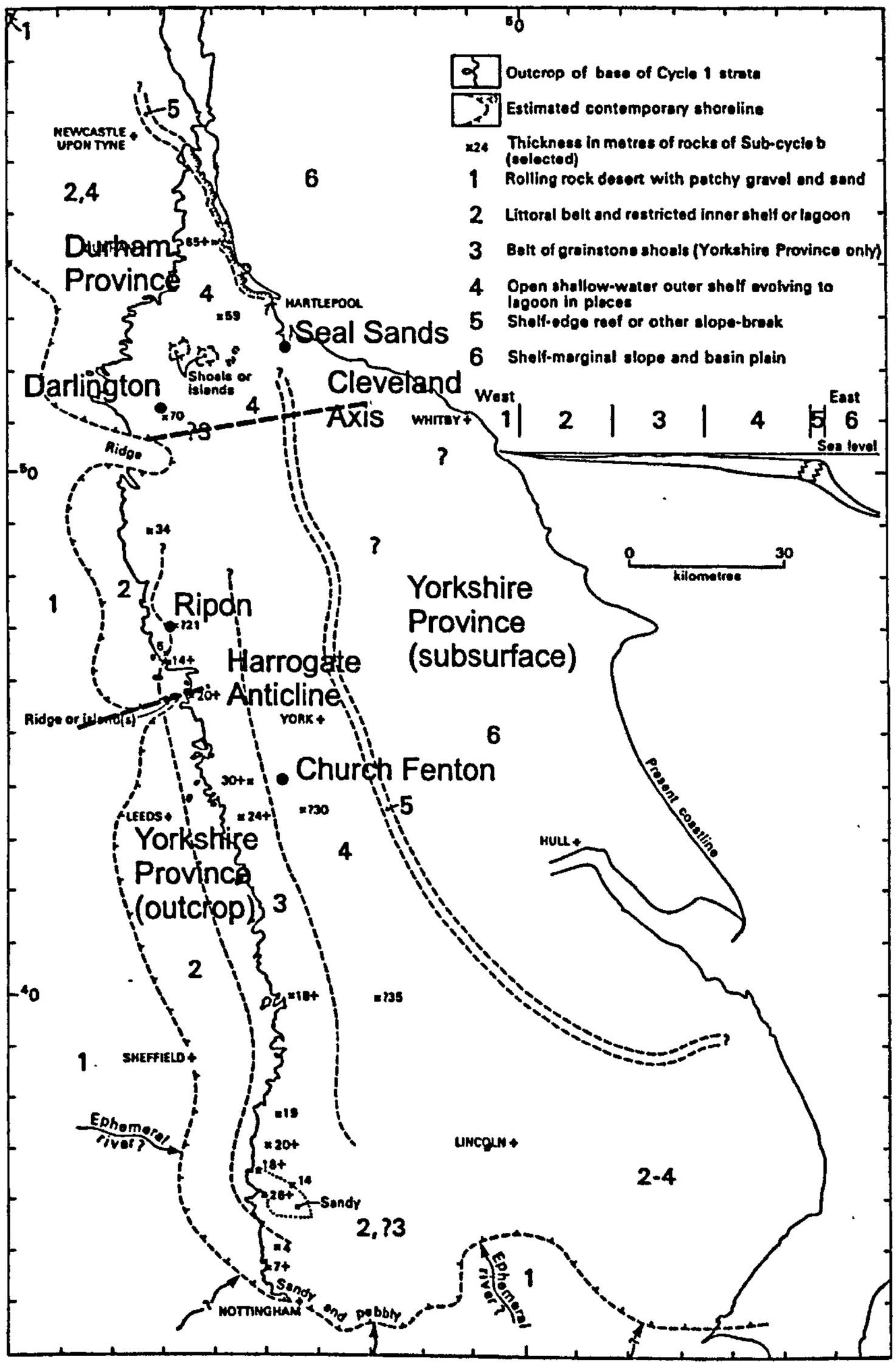


Figure 2.2: Palaeogeography of the EZ1 carbonate phase.
Map adapted from Smith (1989) showing the locations of the investigation areas and the Seal Sands borehole.

The limestone rocks are overlain by the sulphate-rich mineral, gypsum, which is precipitated out of the water column as the salinity of the water increases. The implication is that the Zechstein Sea had become enclosed by the time gypsum started to precipitate.

Laboratory experiments show that in water at a temperature of 38 °C a concentration of only 2 g of gypsum per 1000 g of distilled water is required before precipitation occurs (Ostroff and Metler, 1966). Introducing only small quantities of sodium chloride (NaCl) and magnesium chloride ($MgCl_2$) salts, to simulate seawater, has a marked influence on the precipitation of gypsum from the solution. Saturation occurs with 8 g of gypsum per 1000 g of solution. At sea level, the anhydrous form of gypsum, anhydrite, can only be precipitated out of sea water if the temperature of the solution is greater than 52 °C (Hardie, 1967). Therefore, only under extreme conditions will anhydrite be precipitated out of saline water bodies.

In the Yorkshire Province the EZ1 gypsum deposits are represented by the Hayton Anhydrite Formation, equivalent to the Hartlepool Anhydrite Formation further north. The thickest deposits of EZ1 evaporites, attaining thicknesses of approximately 100 m, were laid down along an axis orientated through Whitby and Beverley, east of the massive reefs (Figure 2.3). Thinner beds of gypsum were laid down in the lagoons behind the reefs, thinning out westwards in the outcrop region of the Permian rocks.

The red-brown mudstones and siltstones, commonly with veins of gypsum, of the Edlington Formation complete the EZ1 cycle. The Edlington mudstones are up to 55 m thick in a narrow belt from York to Retford, thinning rapidly eastwards. The depositional environment of the calcareous mudstones has been interpreted as a rapidly evolving complex of alluvial plains, sabkhas and lagoonal shelf. This formation is only present in the west, deposited behind the reefs protecting the quiet lagoons from the wider Zechstein Sea.

The second English Zechstein Cycle, EZ2, was initiated by a refreshing of the Zechstein Sea. A new layer of carbonate deposits was laid down, known as the Kirkham Abbey Formation in the Yorkshire Province. The Kirkham Abbey carbonates interdigitate and grade westwards, towards the Permian outcrop area, into the Edlington Formation mudstones. Further north, the EZ2 carbonate phase is represented by the parallel-bedded, cream-coloured Roker Dolomite Formation that forms high sea cliffs north of Sunderland. These formations are generally 120 m to 150 m thick, but up to 230 m thick just east of the basinward slope.

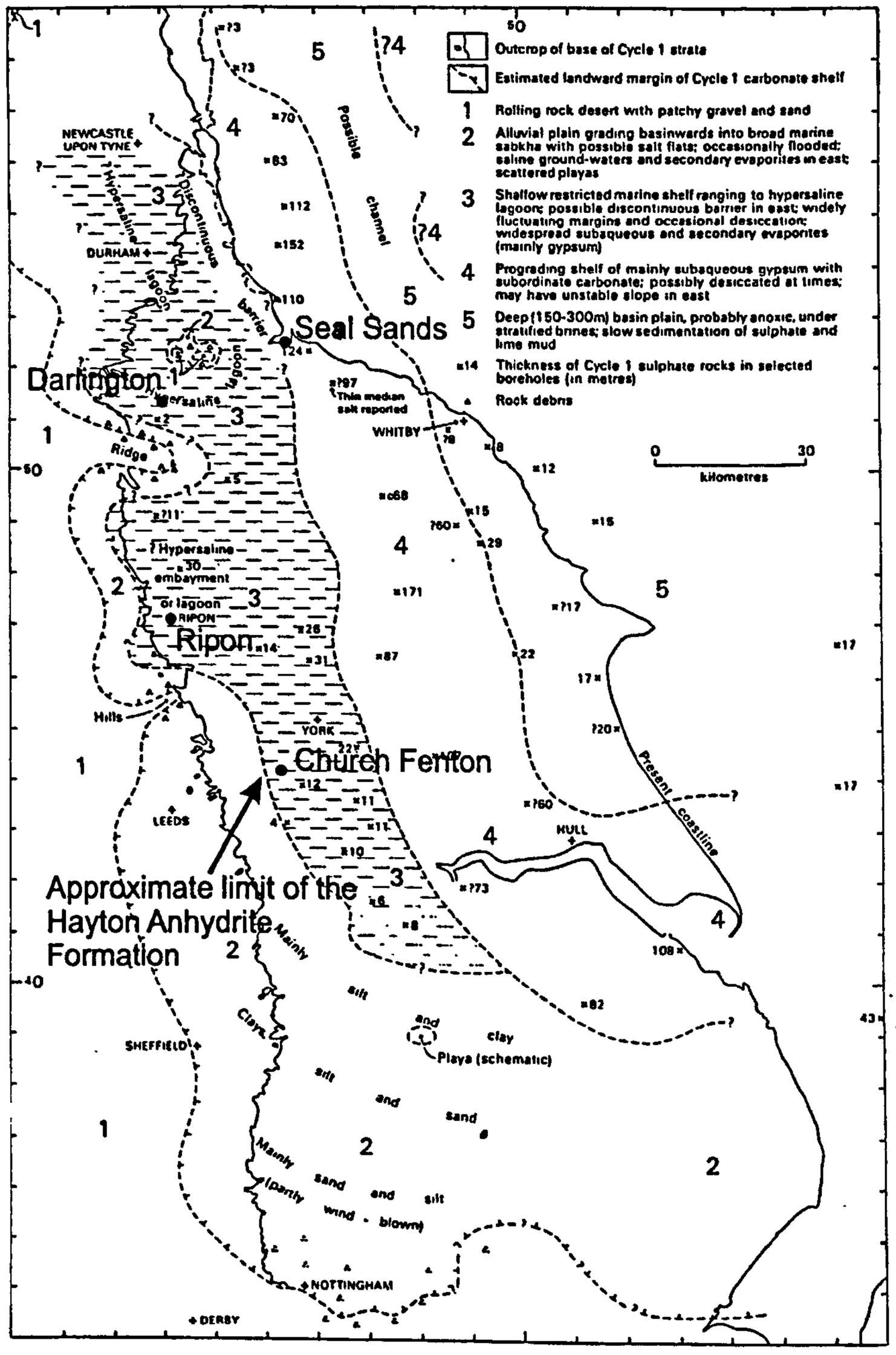


Figure 2.3: Palaeogeography of the EZ1 sulphate evaporite phase.
Map adapted from Smith (1989).

The Fordon Evaporite Formation was deposited along a central axis following approximately the line of the present North Yorkshire coastline, overlapping the Kirkham Abbey Formation. The Fordon Evaporite beds imply that the Zechstein Sea basin was again detached from the wider ocean, with the seawater becoming saturated with respect to gypsum for precipitation to occur. The Fordon Evaporite thins out westwards, pro-grading into the lagoonal deposits of the upper sections of the Edlington Formation.

An extensive gently tapering wedge of carbonate based rocks, showing very little lithological and faunal variation, indicates a second refreshing of the waters of the Zechstein Sea and marks the onset of the third English Zechstein Cycle, EZ3. This bed is called the Brotherton Formation in the Yorkshire Province, and is known as the Seaham Formation in the Durham Province. These formations are interpreted as being laid down on a shallow broad shelf of an almost tideless tropical inland sea.

Differences in the character of rocks of the same type deposited at the same time in the Durham and Yorkshire provinces are caused by an area of high ground in the palaeo-geography of the Permian landscape, the Cleveland Axis. Successive layers of limestones, evaporites and marls filling the Zechstein Basin gradually reduced the height differential and, therefore, the influence of the Cleveland Axis. The Billingham Anhydrite Formation straddles both provinces as an extensive sheet of gypsum (Figure 2.4) laid down in a very shallow marine environment. Eventually, the levels of salinity increased sufficiently for sodium and potassium salts to precipitate, forming the Boulby Halite and Boulby Potash formations.

The siliciclastic silts and clays of the Carnallitic or Rotten Marl are interpreted as deposits in a near-marine, coastal plain environment, slightly above sea level as the shoreline of the Zechstein Sea withdrew far to the east. These marls are considered as a dividing interval between cycles EZ3 and EZ4.

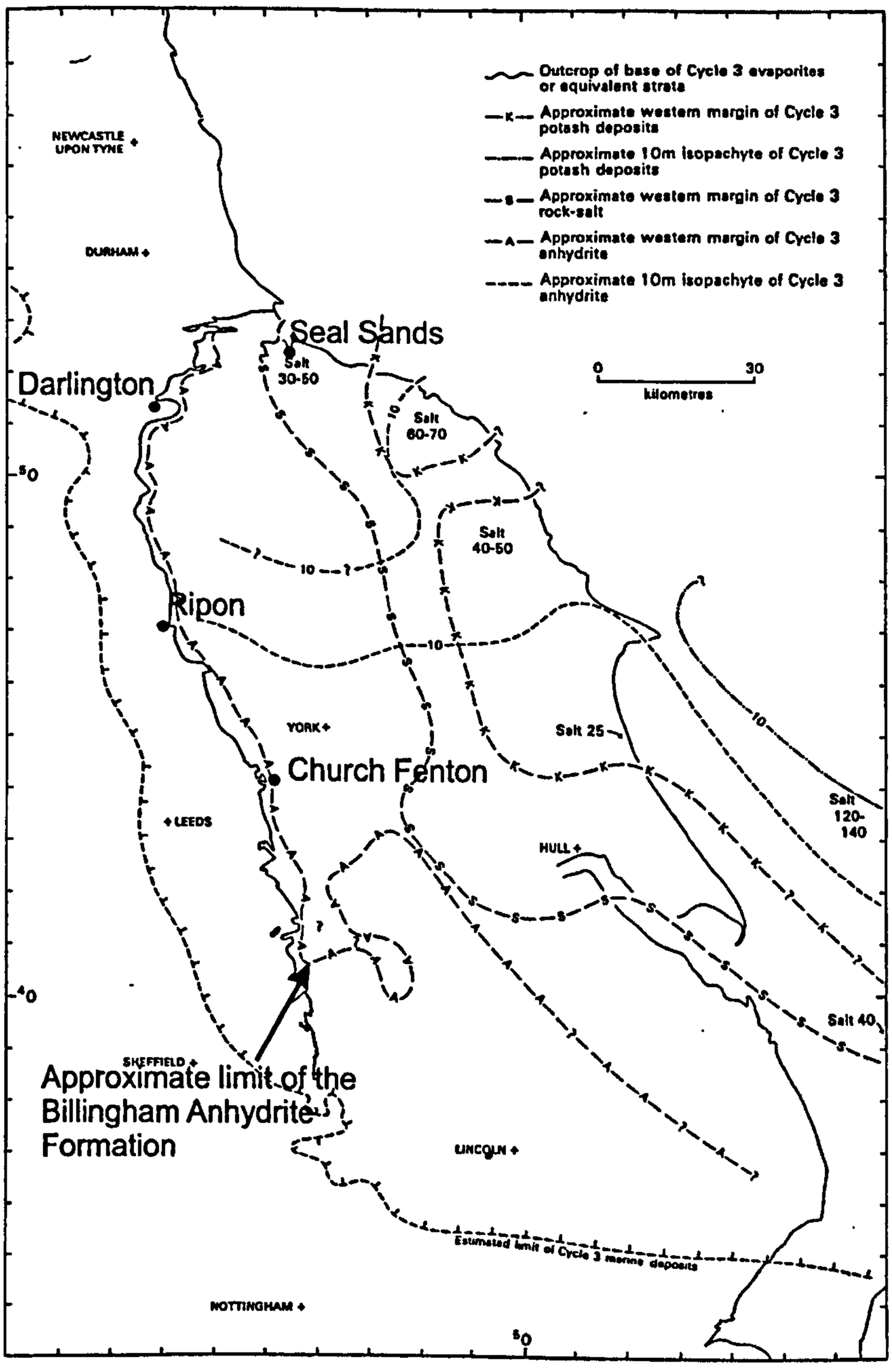


Figure 2.4: Distribution of the EZ3 evaporites.
Map adapted from Smith (1989).

A very thin unfossilerous limestone, the Upgang Formation, signifies the onset of the EZ4 cycle. The late stage Zechstein Sea, comparable to a large salt lake, only required a few metres of sea level rise coupled with differential subsidence to inundate the surrounding coastal plains. The evaporitic Sherburn Anhydrite and Sneaton Halite formations were deposited as the Zechstein Sea once again dried out. These EZ4 beds are centred concentrically about Whitby, with the limit of deposition of the gypsum of the Sherburn Anhydrite approximately 10 km west of York (Figure 2.5).

Sheets of lithologically uniform, water-lain silts and clays, formed on the distal extremities of tidal flats, drape over the Zechstein cycles in the Permian outcrop zone and Durham Province. The marls of the Roxby Formation form EZ5, the last of the Permian English Zechstein cycles to the west and north. To the east, the Roxby Formation marls pass into the Sleights Siltstone, similar to the Carnallitic Marl, which was laid down on the coastal plain as sea receded eastwards. The siltstone is topped by the thin Littlebeck Anhydrite. The local geological succession then passes conformably upwards into the Triassic Sherwood Sandstone Group.

The deep borehole at Seal Sands (Figure 2.6), 26 km east of Darlington, cuts through almost the whole sequence of the English Zechstein in the Durham Province, terminating in the Hartlepool Anhydrite Formation at 6000 m below ground level.

With burial, the onset of dehydration of primary gypsum into anhydrite will depend on the geothermal gradient, composition of the internal water, and the ratio of the lithostatic and hydrostatic pressures (MacDonald, 1953). A one-dimensional finite-difference computer model (Jowett et al., 1993) predicts that gypsum can convert to anhydrite at shallow depths, around 400 m, when overlain by insulating lithologies in a high heat flow region such as a rift zone. In stable cratonic regions, the depth of conversion may be as deep as 4000 m when gypsum is overlain by beds of relatively high thermal conductivity. The complete transformation of gypsum to anhydrite results in two molecules of water expelled from the crystal lattice per molecule of calcium sulphate and a 39% decrease in volume (Hanshaw and Bredehoeft, 1968). The expulsion of large volumes of water may have a significant geological impact (Perry and Lefticariu, 2004).

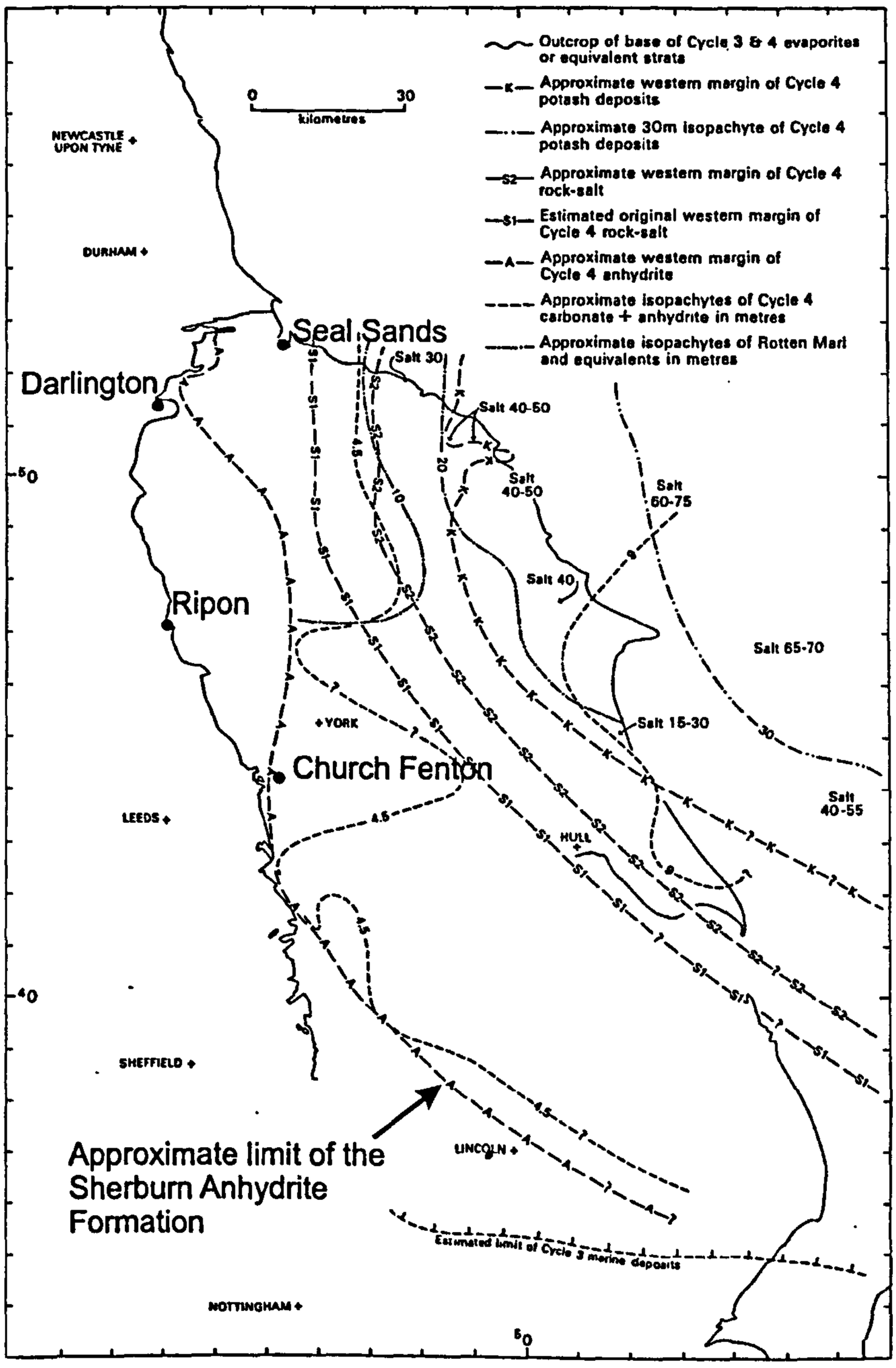


Figure 2.5: Distribution of the EZ4 evaporites.
Map adapted from Smith (1989).

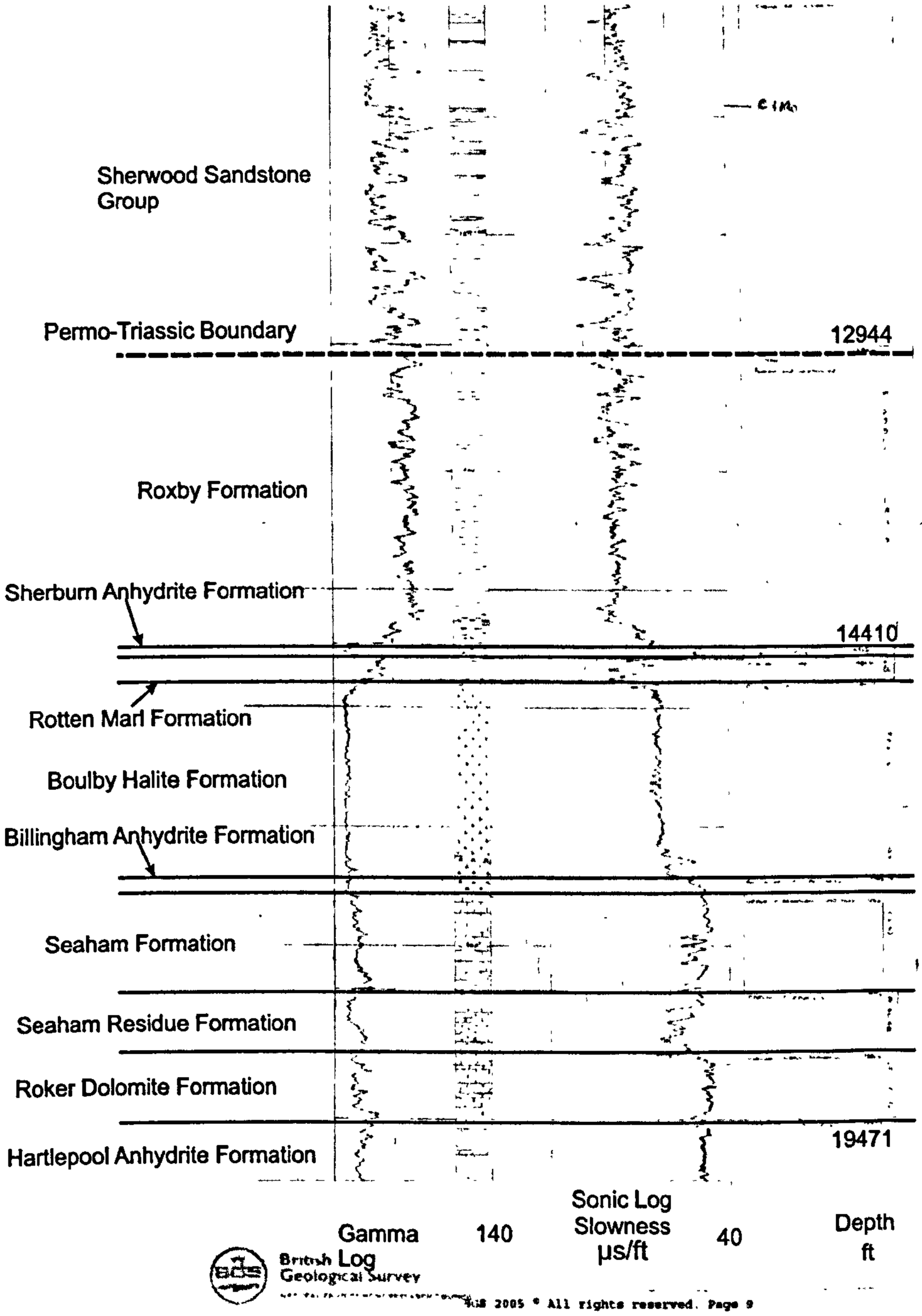


Figure 2.6: Sonic and natural gamma logs from the deep Seal Sands borehole. The national grid reference for Seal Sands is NZ 53796 23805. The graphs have been expanded and annotated for clarity.

2.2 Geology at Darlington

The general structural trend is a gentle dip of approximately 3° to the east-south-east (Figure 2.7). A recent re-evaluation of the entire borehole record collection (Gordon, 2002) revealed that an easterly dipping syncline underlies the urban centre of Darlington. In the same analysis, a major fault striking east-west was delineated to the south of the urban zone. Two lesser faults splay off the main fault towards the south-west and the south-east.

The sequence of Permian rocks beneath Darlington (Table 2.1) is exemplified by the Hurworth Place borehole (Figure 2.8) which penetrates into the Coal Measures. The Coal Measures themselves do not outcrop beneath Darlington, and are known only from borehole records.

The Permian succession at Darlington conforms to the modern classification of English Zechstein cycles in the Durham Province (Smith, 1986). At the base of the Permian sequence, resting unconformably on the Coal Measures, are thin beds of Yellow Sands and Marl Slate, followed by the massive Raisby and Ford formations. The Raisby Limestone is dolomitic, pale grey and yellow, and up to 50 m thick locally. The Ford Limestone was developed in the late 1960s as a local water aquifer (Cairney, 1972), and is a buff-coloured oolitic porous dolomitic limestone, up to 70 m thick.

The quiet lagoonal back-reef red-brown mudstones and siltstones of the Edlington Formation are often recorded with thin bands of gypsum. Thick beds of gypsum, forming the Hartlepool Anhydrite Formation, are found at the base of the Edlington Formation on top of the Ford dolomitic limestone. The thickness of Hartlepool Anhydrite varies rapidly both laterally and vertically, a function of the original geometry of deposition and dissolution.

Overlying the Edlington Formation is the Seaham Formation, typically 15 m to 20 m thick, a thinly bedded pale grey calcitic dolomitic limestone. The Seaham Formation is an artesian aquifer that is commonly tapped by farms. The overlying Billingham Anhydrite Formation reaches a maximum thickness of 10 m, thinning and pinching out westwards. The dissolution of the Billingham Anhydrite and the Hartlepool Anhydrite gypsum layers have been attributed as the cause of the numerous shallow sub-circular hollows to the south and east of Darlington.

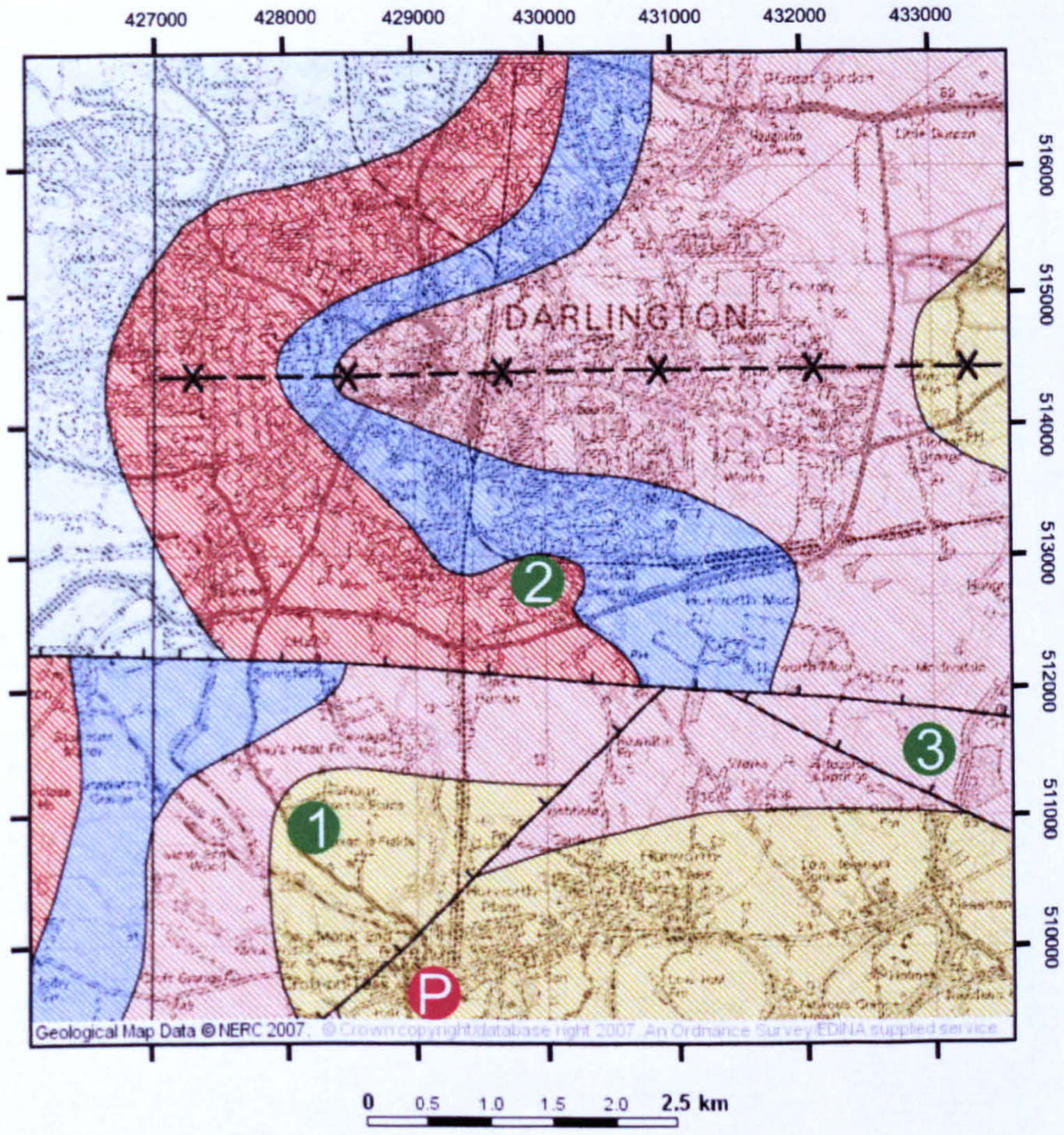


Figure 2.7: Solid geology beneath Darlington.
Data supplied by Ordnance Survey/EDINA service © Crown Copyright Database 2007. Where a fault is at right angles to the strike the outcrops on the upthrow side should be shifted in the direction of dip. Therefore, the direction of throw is wrong on the west-east trending fault. The direction of throw is also wrong for the south-east trending fault splayed off the main west-east fault.

Stratigraphic Unit	General Description	Thickness
Quaternary deposits	Glacial till, laminated clay and alluvial deposits.	5 – 20 m
Sherwood Sandstone Group (Triassic)	Red-brown sandstone. Siltstones and mudstones at the base.	Up to 35 m on the western feather edge.
Roxby Formation (Permian)	Red-brown calcareous mudstone with thin bands of gypsum and anhydrite.	20 – 45 m
Billingham Anhydrite Formation (Permian)	Anhydrite or secondary gypsum, frequently dissolved.	0 – 8 m
Seaham Formation (Permian)	Pale grey calcitic limestone.	14 – 20 m
Edlington Formation (Permian)	Red-brown calcareous mudstone with thin bands of gypsum and anhydrite.	6 – 35 m
Hartlepool Anhydrite Formation (Permian)	Anhydrite or secondary gypsum, commonly dissolved.	0 – 40 m
Ford and Raisby formations (Permian)	Pale grey and yellow dolomitic limestone.	50 – 120 m
Yellow Sands Formation (Permian)	Weakly cemented sands of aeolian origin.	<3 m
Undivided formations (Carboniferous)		

Table 2.1: Summary of the general geological succession at Darlington.

The halite-rich and gypsum-bearing Boulby and Sherburn Anhydrite formations are not found at Darlington. Their restricted ranges of deposition are located further to the east.

The red-brown mudstones of the Roxby Formation, reaching up to 50 m thick locally, are the youngest Permian beds around Darlington. They pass conformably upwards into the Triassic Sherwood Sandstone Group. The base of the Sherwood Sandstone Group comprises siltstones and mudstones laid down in a fluvial environment in the distal region of a large alluvial plain. The transition between the Roxby Formation and the Sherwood Sandstone

Group is difficult to distinguish within the unfossiliferous succession (Smith, 1989). Further up the geologic column, the Sherwood Sandstone Group is made up of poorly cemented fine to medium grained sandstone of a red-brown colour, indicating a harsh arid continental desert environment.

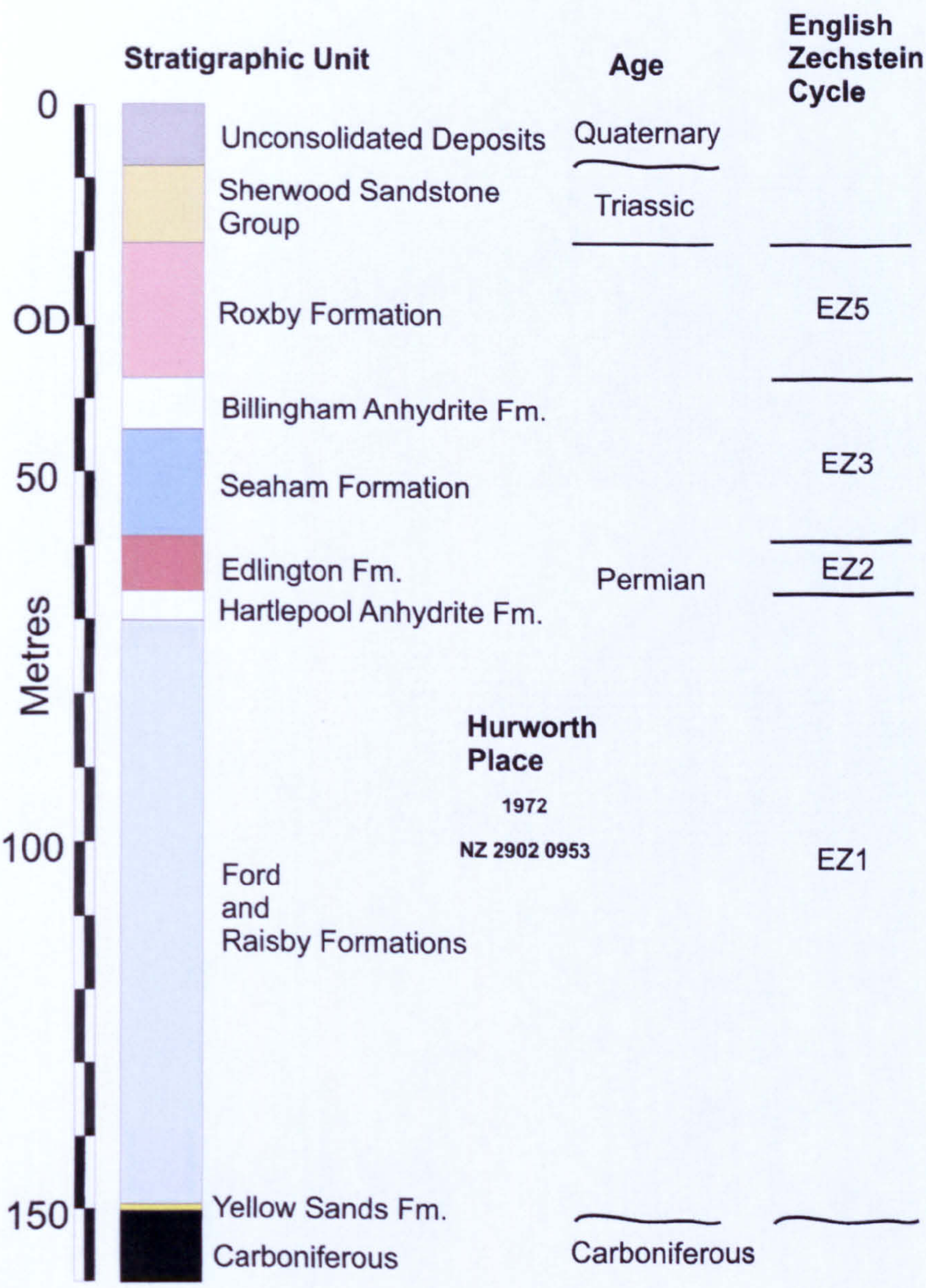


Figure 2.8: Hurworth Place borehole geological succession.

A thick apron of Quaternary deposits of differing origins (Figure 2.9) ranging from 20 m to 50 m in depth, cloaks the solid geology underlying Darlington. Most of these unconsolidated materials consist of Devensian Till. Passing south of Darlington is the River

Tees, a major water course with several associated tributaries including the River Skerne which bisects the centre of Darlington. This river system has reworked the till and generated a vast area of silts, sands and gravels.

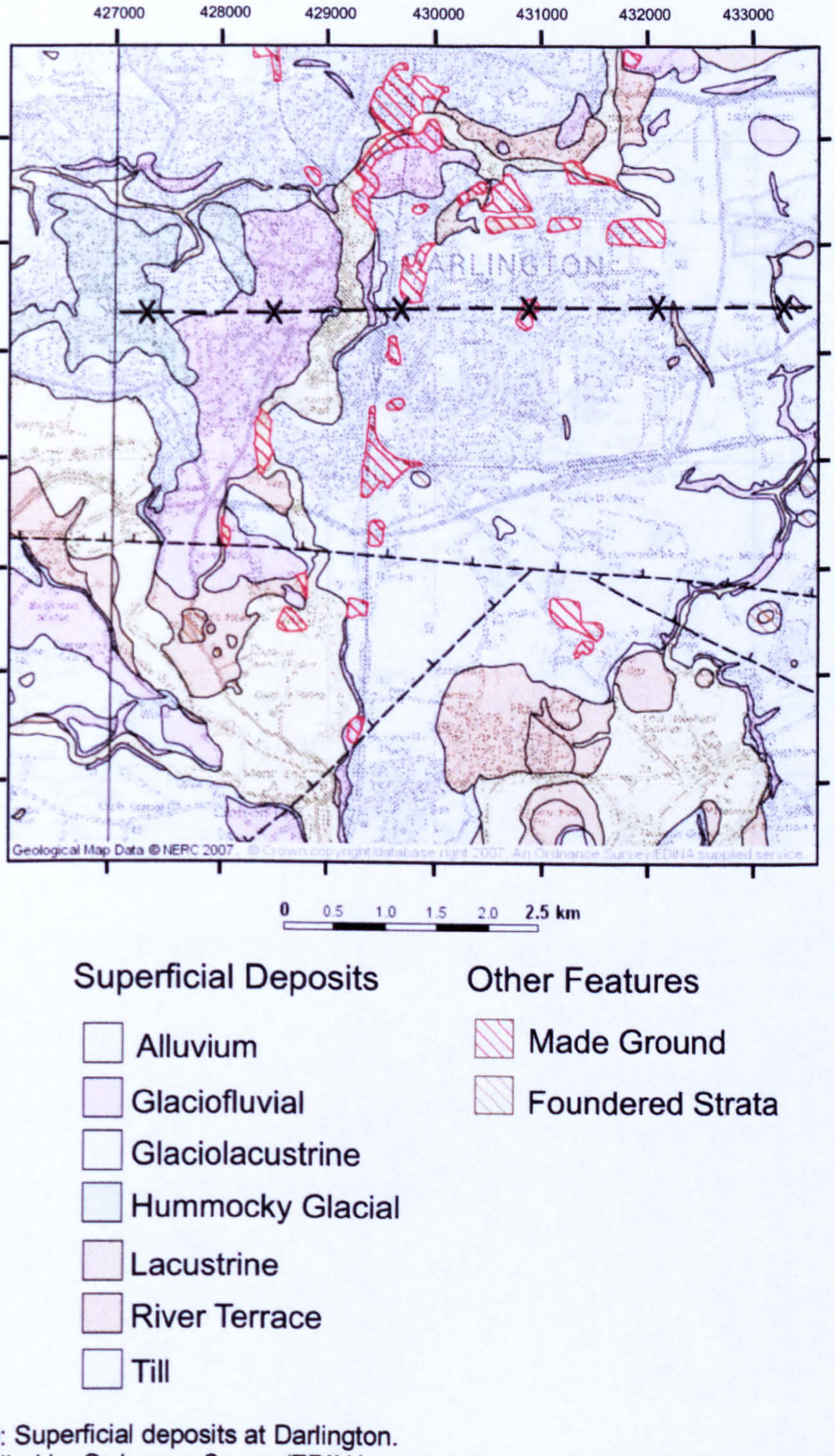


Figure 2.9: Superficial deposits at Darlington.
Data supplied by Ordnance Survey/EDINA service © Crown Copyright Database 2007.

2.3 Geology at Church Fenton

The Permian strata at Church Fenton dip and thicken towards the north-east at a shallow gradient of 1 in 50, and are sliced by a series of parallel SW-NE trending faults (Figure 2.10). Detailed geological observations by Edwards et al. (1950) and the deep 1939 Ulleskelf Nurseries borehole (Figure 2.11, Table 2.2) are re-interpreted to conform to the modern nomenclature for the Permian English Zechstein cycles in the Yorkshire Province.

From the fossil record it is concluded that the Carboniferous rocks at Church Fenton are from the Lower Coal Measures (Edwards et al., 1950). The unconformable Yellow Sands Formation comprises loosely compacted sands of aeolian origin. It is overlain by a thin bed, approximately 3m thick, of grey marl limestone, the Marl Slate Formation.

The massive Cadeby Formation, 60 m thick locally, is comprised of yellow to buff dolomitic limestone. The lower sections are extremely fossiliferous and vug-filled. The upper sections have a compact, tight granular appearance with very few original structures present, and the cream-coloured stone has been used as building material adding much character to the local villages and towns.

Church Fenton is at the western limit of deposition of the EZ1 gypsum-bearing Hayton Anhydrite Formation (Figure 2.3). No evidence for the Hayton Anhydrite gypsum beds resting on top of the Cadeby Formation is recorded in any of the local deep boreholes and it is unlikely to exceed a few metres in thickness locally. The Cadeby Formation is typically overlain by beds of red-brown mudstones and siltstones of the Edlington Formation with a thickness of 20 m to 30 m.

The calcareous mudstones are overlain by the grey, flaggy, hard limestone of the Brotherton Formation, which is about 20 m thick. Both the Cadeby and Brotherton limestones are good aquifers and are tapped for the brewing industry at nearby Tadcaster and by small private borings at farmsteads.

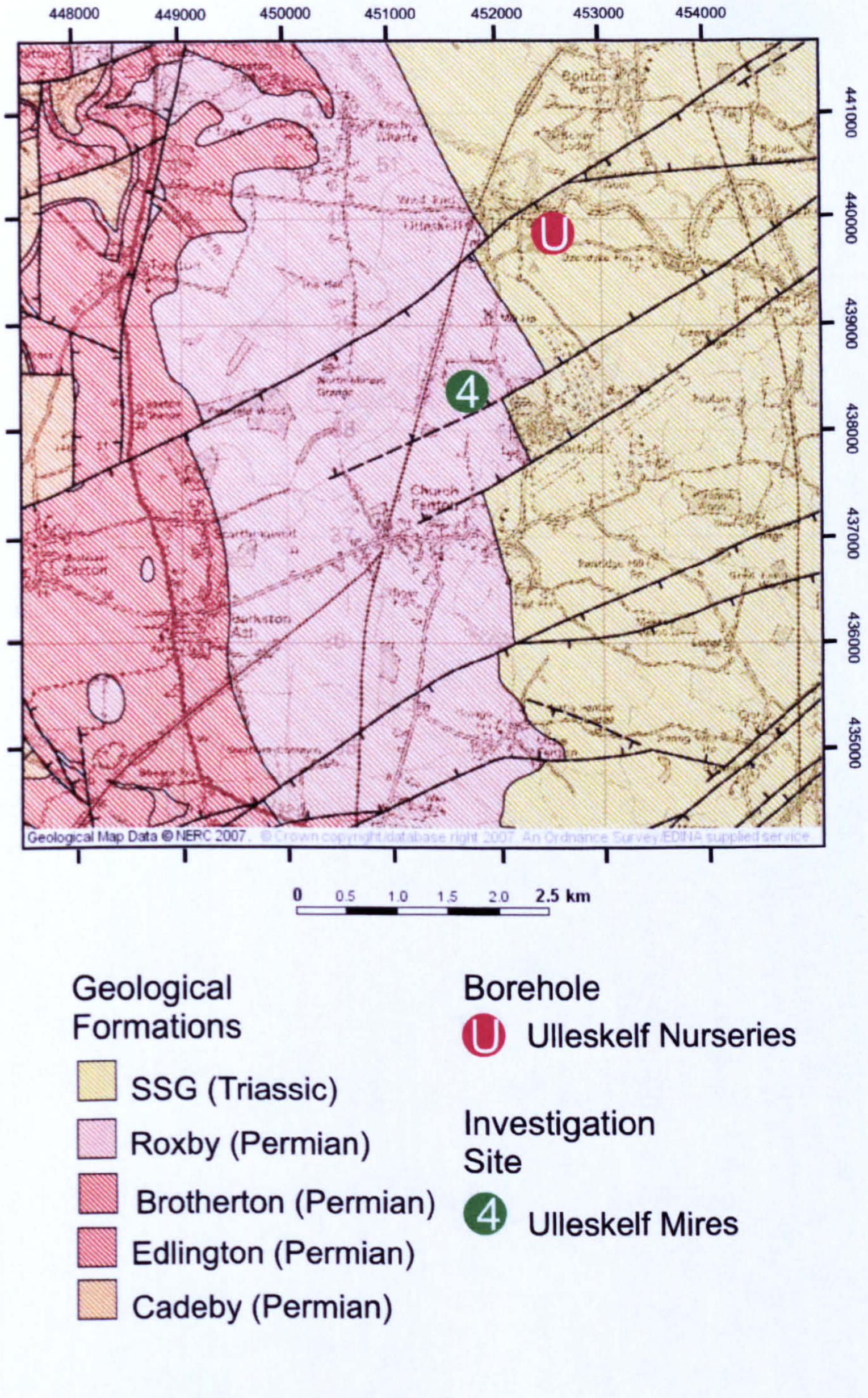


Figure 2.10: Solid geology beneath Church Fenton.
Data supplied by Ordnance Survey/EDINA service © Crown Copyright Database 2007.

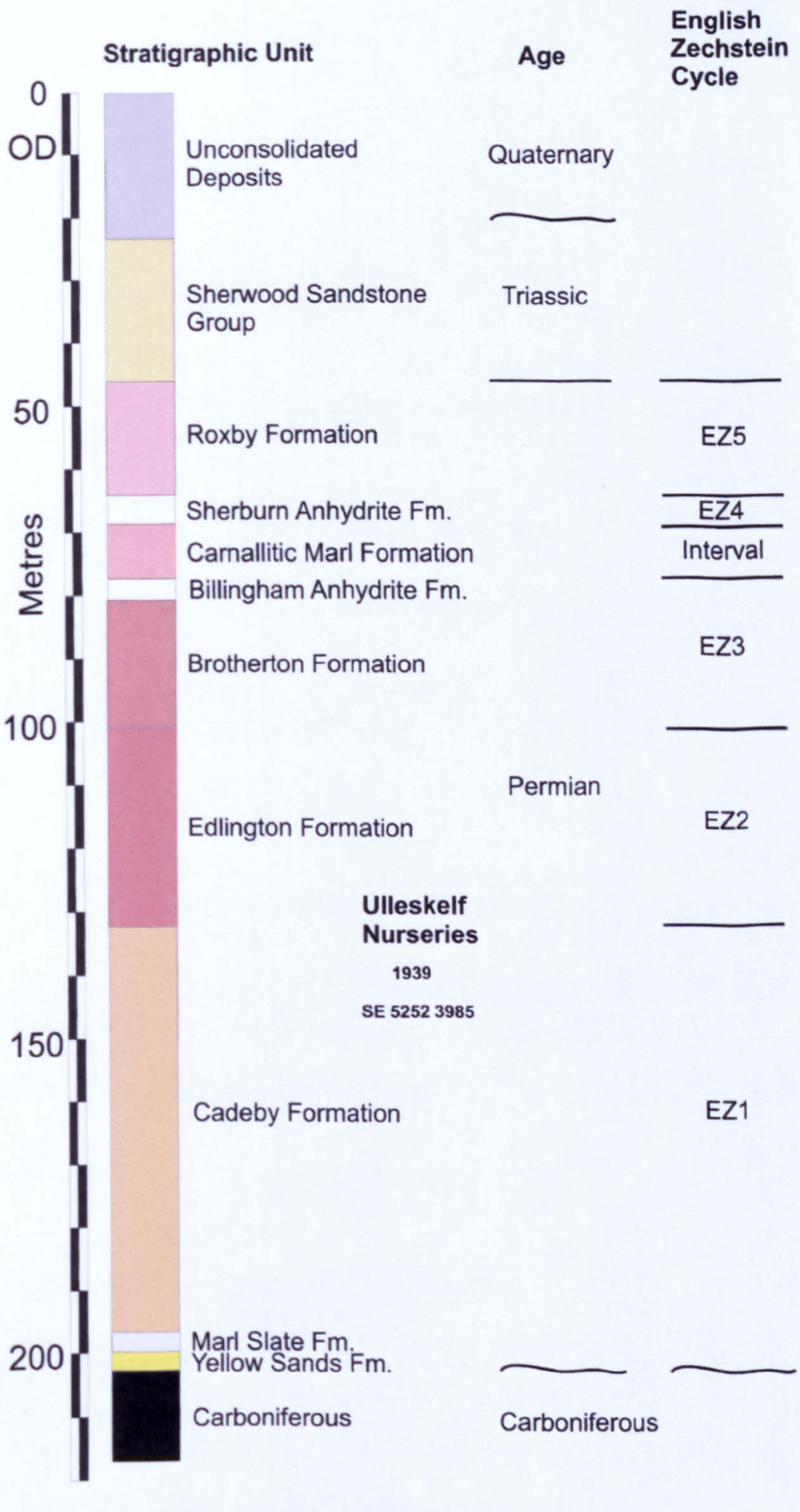


Figure 2.11: Ulleskelf Nurseries borehole geological succession.

Stratigraphic Unit	General Description	Thickness
Quaternary deposits	Fine grained clay glacial lake deposits.	20 – 25 m
Sherwood Sandstone Group (Triassic)	Red-brown sandstone. Siltstones and mudstones at the base.	0 – 20 m
Roxby Formation (Permian)	Red-brown calcareous mudstone with thin bands of gypsum and anhydrite.	2 – 25 m
Sherburn Anhydrite Formation (Permian)	Anhydrite or secondary gypsum, frequently dissolved.	0 – 5 m
Carnallitic Marl Formation (Permian)	Red-brown calcareous mudstone.	0 – 10 m
Billingham Anhydrite Formation (Permian)	Anhydrite or secondary gypsum, frequently dissolved.	0 – 5 m
Brotherton Formation (Permian)	Pale grey calcitic limestone.	15 – 20 m
Edlington Formation (Permian)	Red-brown calcareous mudstone with thin bands of gypsum and anhydrite.	10 – 35 m
Hayton Anhydrite Formation (Permian)	Anhydrite or secondary gypsum, commonly dissolved.	0 – 5 m
Cadeby Formation (Permian)	Pale grey and yellow dolomitic limestone.	50 – 70 m
Marl Slate Formation (Permian)	Evenly laminated, carbonaceous, dolomitic and calcareous siltstone.	<3 m
Yellow Sands Formation (Permian)	Weakly cemented sands of Aeolian origin.	<3 m
Undivided formations (Carboniferous)		

Table 2.2: Summary of the general geological succession at Church Fenton.

A thin bed of gypsum, about 2 m thick, represents the Billingham Anhydrite Formation and forms a veneer on the Brotherton Formation. A further relatively thin gypsum bed, the Sherburn Anhydrite Formation, is present in the Ulleskelf Nurseries borehole at a shallower depth. About 5 km to the south of Church Fenton the Sherburn Anhydrite was sufficiently thick and of good enough quality to be mined commercially until recently (Thompson et al., 1996). The red-brown siliciclastic Carnallitic Marl forms a barrier between the two gypsum beds.

The Permian sequence at Church Fenton is completed by the red-brown marls of the Roxby Formation and is conformable with the overlying Triassic Sherwood Sandstone Group. Both formations are present at rockhead before thinning out up-dip to the south west. A common water table is shared where permeable Quaternary deposits overlie the porous soft red sandstone aquifer.

Two glacial moraines, York and Escrick, lie a few kilometres to the north of Church Fenton. These features represent the most southerly advance of the great ice-sheets of the Devensian stage of the Quaternary Age. As the glaciers melted, the waters were dammed behind a remnant finger of ice across the Humber Gap, forming a large lake. Thick deposits, typically 25 m deep at Church Fenton, of fine-grained material were deposited in the low energy environment. Around Church Fenton clays and silts are predominant (Figure 2.12) whereas further north, towards Ulleskelf village, the content of glacial lake deposits becomes increasing sandy. The fine-grained deposits of glacial origin have recently been incised by the River Wharfe, which has deposited a sinuous band of sands and gravels. Several extensive, irregularly shaped, peat-filled areas are present to the west of RAF Church Fenton.

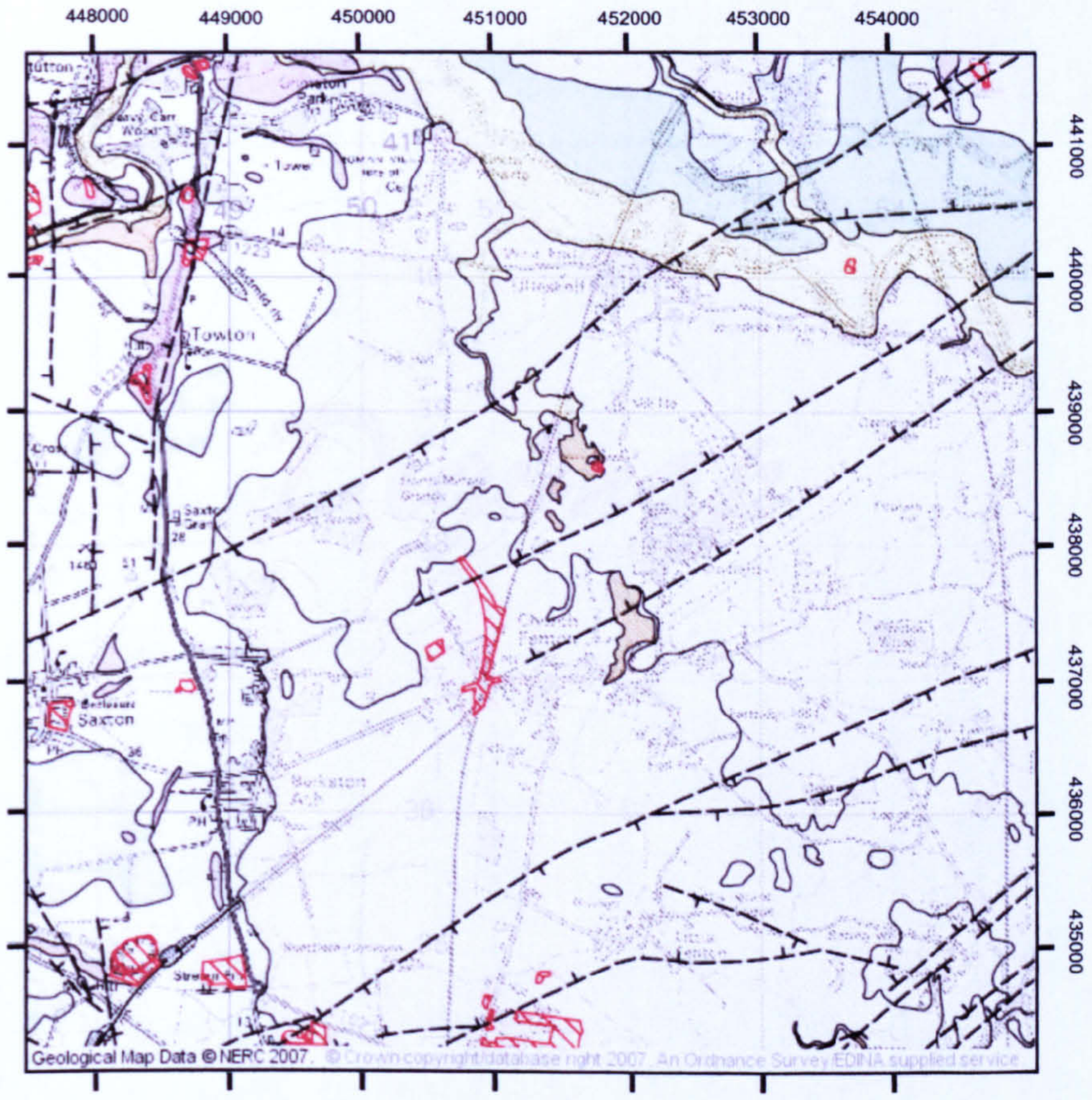


Figure 2.12: Superficial deposits at Church Fenton.
Data supplied by Ordnance Survey/EDINA service © Crown Copyright Database 2007.

2.4 Geology at Ripon

Details of the geology around Ripon are provided by the BGS geological memoirs of Thirsk (Powell et al., 1992) and Harrogate (Cooper and Burgess, 1993). Rocks of Permian and Triassic age form the bedrock around Ripon (Figure 2.13). They dip gently towards the east at approximately 3°, and the thickness of the formations also increases to the east. Faults of small throw cross cut the bedrock with strike directions approximately parallel to the dip of the bedding. A thick blanket of Quaternary drift covers the bedrock (Figure 2.14), whilst the N-S trending channel of the proto-River Ure cuts down into it (Thompson et al., 2006). The centre of the City of Ripon stands on the higher ground on the west bank of the river.

The earliest rocks of Permian age are thin beds, less than 3 m thick, of the Yellow Sands and Marl Slate formations, proved only by boreholes (Table 2.3). These are underlain by Carboniferous rocks of the Westphalian and Namurian stages, consisting of thin cycles of sandstones, mudstones and siltstones, which have been interpreted as being deposited in swamps and lagoons.

During the carbonate depositional phase of the English Zechstein cycle, EZ1, the location of present day Ripon was at the western edge of the Zechstein Sea (Figure 2.2). The paleogeography deduced from the stratigraphy also places Ripon between two capes, to the south, the Harrogate Anticline formed a series of islands or headlands, and another ridge of land protruded into the Zechstein Basin to the north. The centre of deposition gradually moved eastwards within each successive English Zechstein cycle, so only early cycle lithologies plus the overarching Roxby Formation are found at Ripon.

The EZ1 carbonate phase is represented by the Cadeby Formation, a limestone which is grey-buff in colour, 40 m to 65 m thick, and which has been extensively dolomitised destroying many of the original depositional structures.

A thick bed of gypsum, the Hayton Anhydrite Formation rests on top of the Cadeby Limestone. To the north-east of Ripon, 32 m of gypsum are recorded in the Burtree Park Caravan Site borehole (Figure 2.15) and the gypsum is overlain by red-brown mudstones and siltstones of the Edlington Formation. Thin gypsiferous bands are common in the Edlington mudstones, which attain a thickness of 15 m locally.

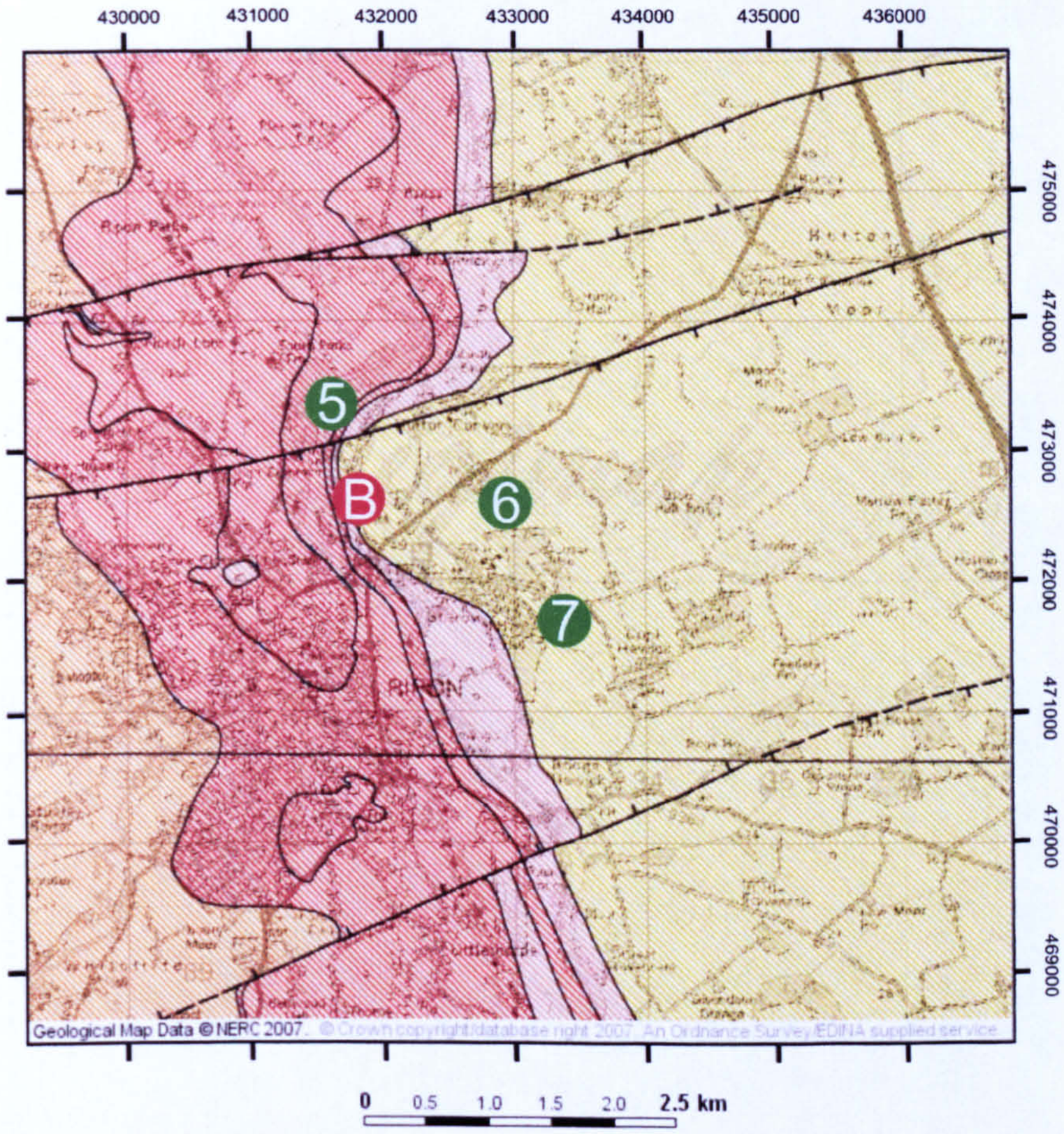


Figure 2.13: Solid geology beneath Ripon.
Data supplied by Ordnance Survey/EDINA service © Crown Copyright Database 2007.

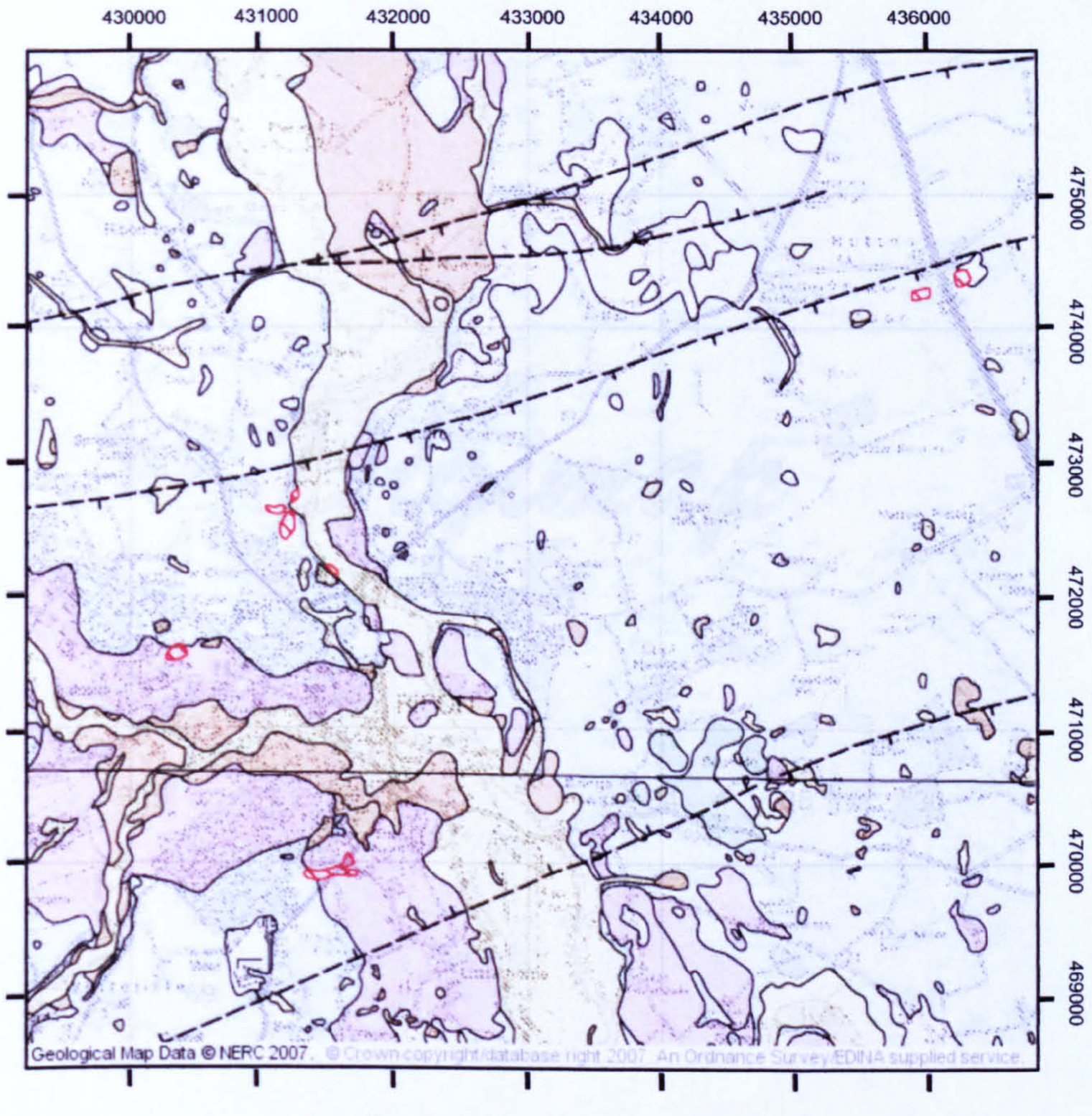


Figure 2.14: Superficial deposits at Ripon.
Data supplied by Ordnance Survey/EDINA service © Crown Copyright Database 2007.

Stratigraphic Unit	General Description	Thickness
Quaternary deposits	Glacial till, laminated clay and alluvial deposits.	5 – 30 m
Sherwood Sandstone Group (Triassic)	Red-brown sandstone. Siltstones and mudstones at the base.	0 – 30 m
Roxby Formation (Permian)	Red-brown calcareous mudstone with thin bands of gypsum and anhydrite.	10 – 20 m
Billingham Anhydrite Formation (Permian)	Anhydrite or secondary gypsum, frequently dissolved.	0 – 8 m
Brotherton Formation (Permian)	Pale grey calcitic limestone.	10 – 20 m
Edlington Formation (Permian)	Red-brown calcareous mudstone with thin bands of gypsum and anhydrite.	10 – 20 m
Hayton Anhydrite Formation (Permian)	Anhydrite or secondary gypsum, commonly dissolved.	0 – 40 m
Cadeby Formation (Permian)	Pale grey and yellow dolomitic limestone.	45 – 65 m
Marl Slate Formation (Permian)	Evenly laminated, carbonaceous, dolomitic and calcareous siltstone.	<3 m
Yellow Sands Formation (Permian)	Weakly cemented sands of Aeolian origin.	<3 m
Undivided formations (Carboniferous)		

Table 2.3: Summary of the general geological succession at Ripon.

The calcareous mudstones of the Edlington Formation are overlain by the Brotherton Formation, which is typically thin bedded, dolomitic, grey to buff coloured, and about 10 m thick. This dolomitic limestone provides a relatively high-yielding aquifer that is commonly tapped as a water supply for farming activities. Outcrops of the Brotherton Limestone exhibit variable dips, probably due to the dissolution of the Hayton Anhydrite. Further to the east of the Ripon study sites, the Billingham Anhydrite Formation gypsum bed overlies the Brotherton Limestone.

The red-brown silty mudstone of the Roxby Formation is 10 m to 18 m thick at outcrop and is the youngest Permian formation at Ripon. It passes conformably and gradationally upwards into the Triassic Sherwood Sandstone Group. Further east the Sherwood Sandstone Group attains thicknesses up to 300 m, and its high porosity makes it a very good aquifer.

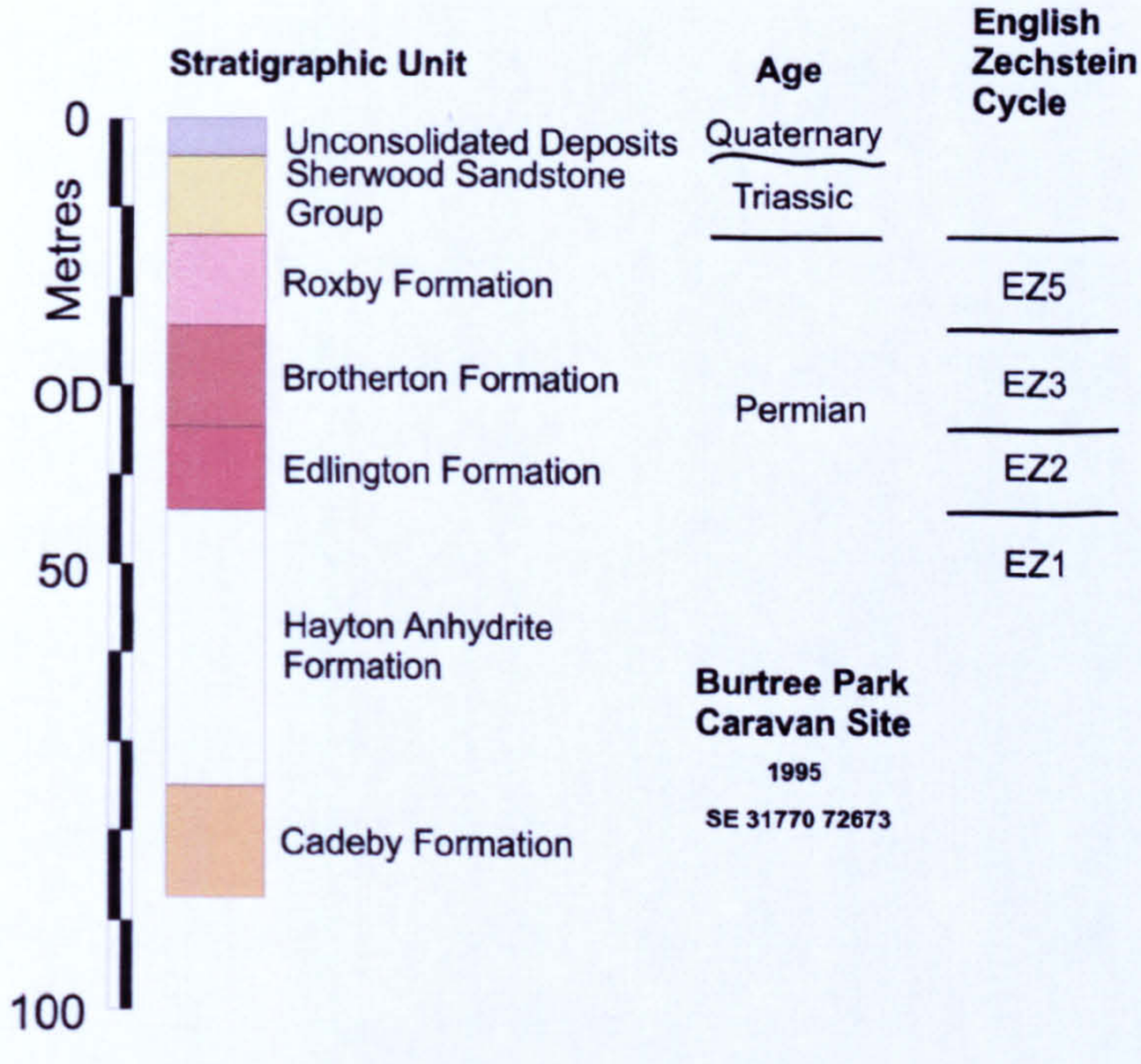


Figure 2.15: Burtree Park Caravan Site borehole geological succession.

A thick undulating mantle of drift cover at Ripon is mostly till of glacial origin from the late Devensian cold stage (Figure 2.14). The most striking Quaternary feature is the sinuous N-S orientated buried river valley which incises the Permo-Triassic bedrock. The age of incision is not very well constrained, with estimates ranging from the Anglian stage, 480,000 years ago, to the latest cold period, the Devensian stage (Thompson et al., 1996). Similarly, the geometry of the buried river valley is poorly known. Superimposed on the alluvium of the buried river valley are glacio-fluvial outwash sediments, the remains of material deposited by melt waters from the last glacial retreat. These sands and gravels have been further reworked by the action of the modern River Ure, which flows along the same path as the buried valley.

3.0 Acquisition

3.1 2D seismic acquisition parameters and survey design

Evison (1952) commented on the shortcomings of applying the seismic reflection technique to shallow targets, and in particular to the problem of reflections being obscured by low-frequency shot-generated noise. Since then, the development of the acquisition of the shallow seismic reflection technique has tracked the trends set by the use of the seismic method in the exploration for hydrocarbon reserves, resulting in a succession of incremental improvements in data quality.

The main field parameters required for shallow seismic surveying are the record length, recording time, digital sampling interval, near-trace offset, far-trace offset, group interval, shot interval, and the fold of cover. The spread configuration has to be chosen to provide these parameters for efficient roll-along acquisition with the number of recording channels available. The choice of parameters is determined by balancing the competing demands of achieving the survey objectives whilst minimizing costs, bearing in mind the theoretical geophysical limitations, and the capabilities of the equipment and personnel available.

The Parkside [NZ 2992 1289] investigation site (Figure 3.1) geological control is provided by the Geneva borehole (Figure 3.2) over which a test record (Figure 3.3) was acquired to define the acquisition parameters. A 5 g saluting blank charge of black powder was detonated at a depth of 1 m in a pre-drilled hole by a buffalo gun into a line of 24 geophones placed 2 m apart. The buffalo gun (Pullan and MacAuley, 1987), is capable of generating an input pulse rich in high frequencies (Miller et al., 1986; Miller et al., 1994). The shot point was located to the north of the borehole near to the railway embankment, with the near channel only 1 m from the shot point. With only an AGC gain function applied, the shot record can be divided broadly into two sections. The upper 120 ms of the record has high-frequency events extending across all traces; these are the reflection arrivals from the sub-surface interfaces and the refraction arrival from the water table. The lower part of the record

is dominated by ground roll with a dominant frequency of 30 Hz. At short two-way travel times on the near traces, the reflection events are masked by the ground roll.

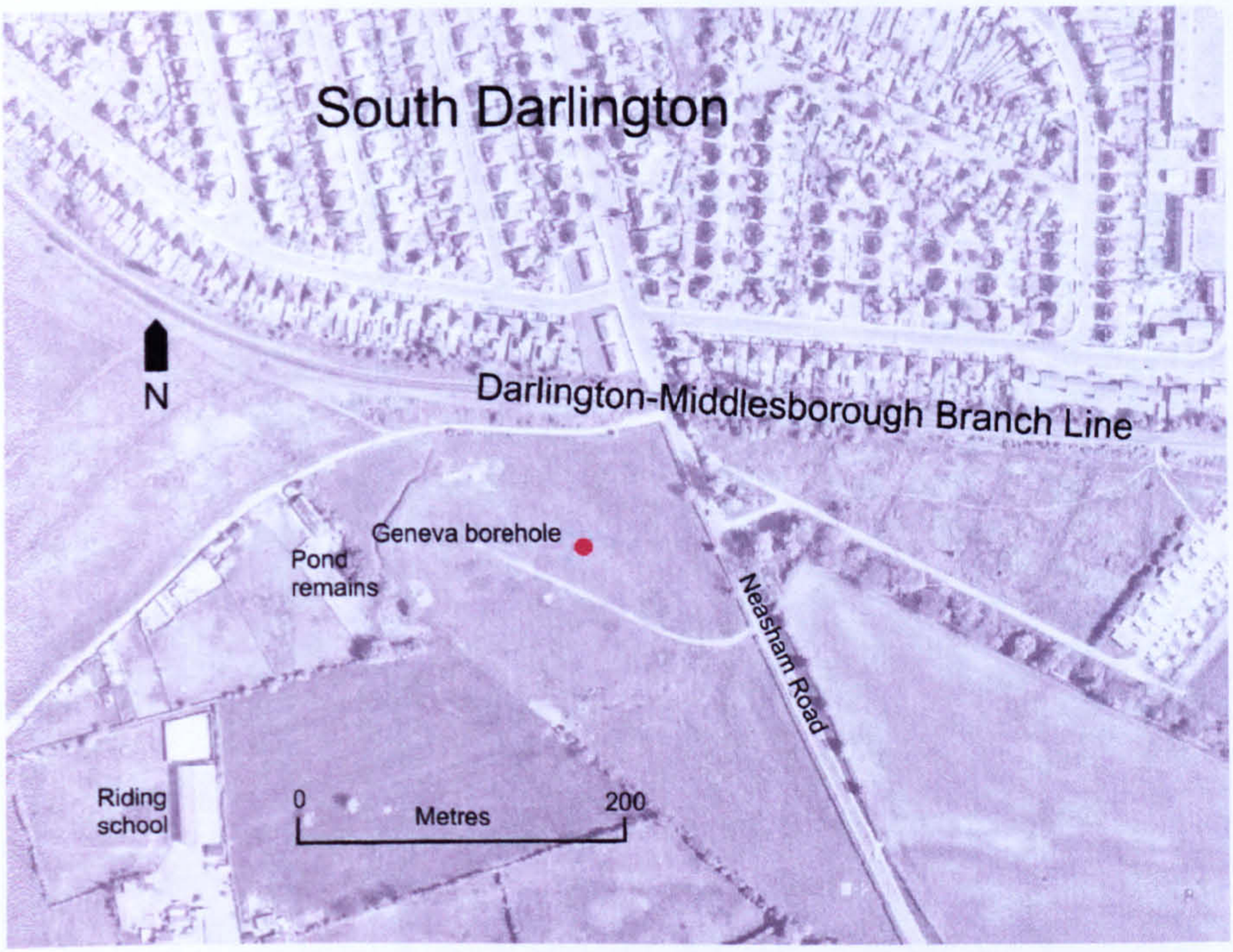


Figure 3.1: Aerial photograph taken in 1988 of the Parkside survey site.

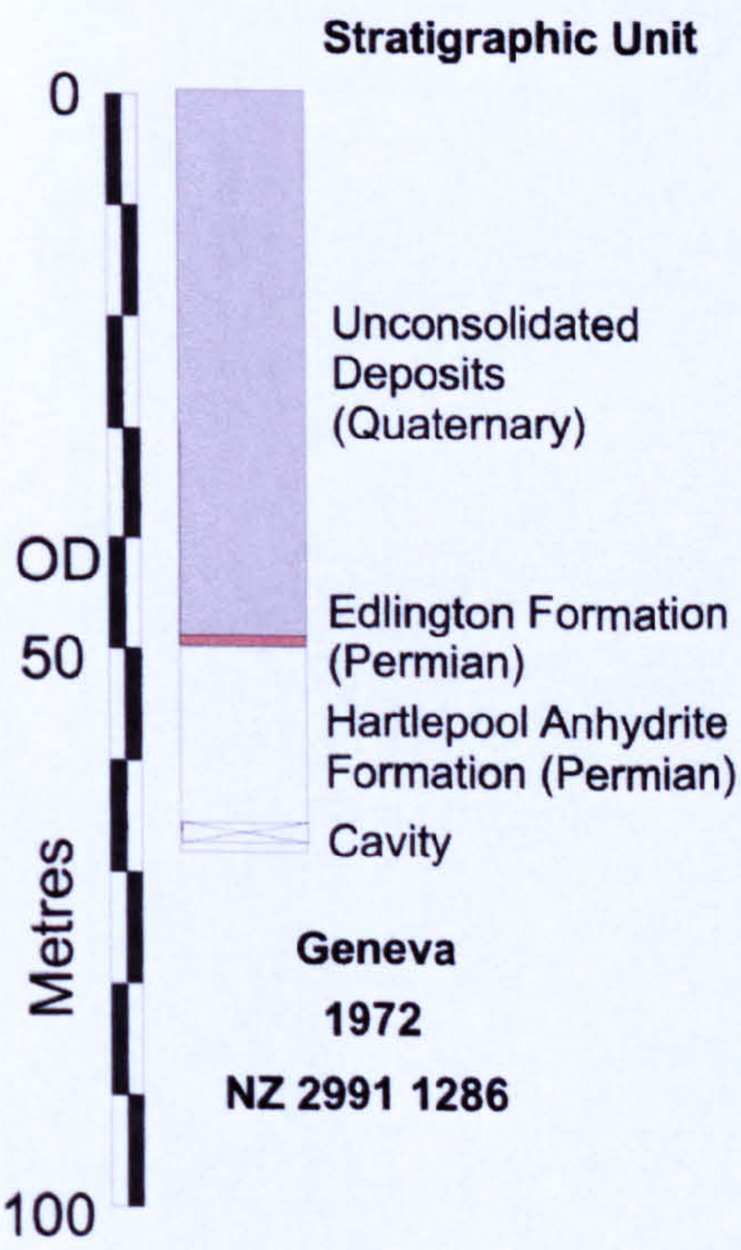


Figure 3.2: Geneva borehole geological succession.

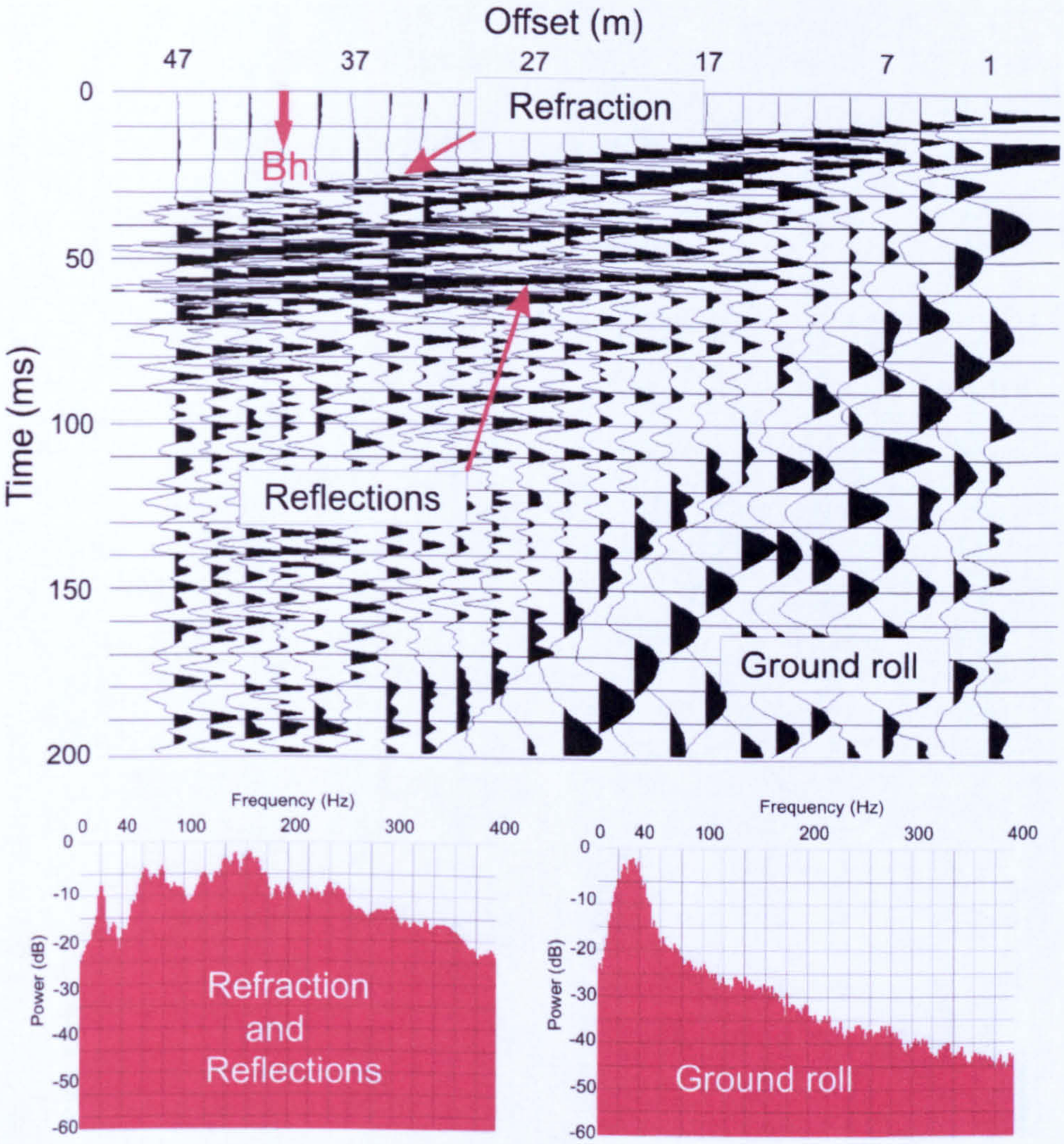


Figure 3.3: Trial wave test at the Parkside survey site.
The seismic data are displayed with a 100 ms AGC sliding window before being cropped at 200 ms. The different sections of the trial shot record were split by surgically muting the unwanted portion prior to spectral analysis.

A number of strategies can be employed to suppress the unwanted ground roll. Traditionally, a commonly used technique was to deploy linear arrays of n geophones in which the distance between neighbouring geophones was chosen to be λ/n, where λ is the dominant wavelength of the ground roll. The ground roll is then suppressed by destructive interference. However, even for small arrays there will be small time differences in the arrival from a reflector between each individual receiver with in the array, so the higher frequencies in the reflection signals will be attenuated (Ziolkowski and Lerwill, 1979; Steeples et al.,

1990). High-resolution is essential to image sub-surface geological structures at the metre scale, so high-frequency signals need to be preserved.

The choice of 23 m as the near-trace offset ensured that the reflected energy and ground roll do not overlap on the shot record. With this near-trace offset, the reflection energy is also sufficiently separated from the refraction arrivals. The reflection signal is maximized when placed within this optimum window (Hunter et al., 1984).

At Parkside the target zone was the Hartlepool Anhydrite bed and a specific objective was to image the cavity intersected at a depth of 66 m by the Geneva borehole. Therefore, the maximum depth of interest is approximately 70 m. A geophone spacing of 2 m and a near-offset of 23 m imply a maximum offset of 69 m for a 24-channel recording system. This off-end shooting arrangement is suitable for good velocity analysis down to the target depth: any reflection from the top of the Hartlepool Anhydrite on the far offsets would not suffer excessive normal moveout stretch, and so all traces could potentially provide useful signal from the target for inclusion in the stacking process.

The Nyquist wavelength λ_N is defined by the formula (e.g, Sheriff and Geldart, 1995):

$$\frac{1}{\lambda_N} = \frac{1}{2\Delta x} \tag{3.1}$$

where Δx is the distance between geophone stations. Hence, a minimum horizontal apparent wavelength of 4 m can be recorded without spatial aliasing when the geophone station spacing is 2 m. High-frequency air-waves and the higher frequency dispersive modes of ground roll are likely to be spatially aliased at 2 m geophone interval; but upcoming reflection events reach the ground surface at angles close to normal incidence, so they have large horizontal apparent wavelengths and therefore will not be aliased.

The minimum geophone station spacing to faithfully image dipping reflectors without spatial aliasing is inversely proportional to the sine of the angle of the dip (e.g., Yilmaz, 2001):

$$\Delta x = \frac{V}{2 f_{\max} \sin\theta} \qquad (3.2)$$

where θ is the dip of the reflector, Δx is the distance between geophone stations, V is the average P-wave velocity through the propagating medium and $f_{\max}$ is the maximum frequency of the signal. The angle of dip of the Permian strata at Parkside is less than 5° (Figure 2.7). Therefore, a 2 m group interval is well within the limit before spatial aliasing of reflection events would occur during migration.

In the common midpoint (CMP) method of seismic profiling (Mayne, 1962) the fold of coverage, F, is determined by the relationship between the geophone and shot point intervals (e.g., Stone, 1994):

$$F = \frac{n}{2s} \qquad (3.3)$$

where n is the number of channels recorded and s is the ratio between the source point interval and the receiver station interval. Stacking with fold of coverage F improves the ratio of signal to random noise by $\sqrt{F}$. Source and receiver station intervals of 2 m were chosen for the Parkside site. By using each shot hole twice, shooting into off-end geophone spreads in front of and behind the shot hole is equivalent to a 48-trace symmetric split-spread configuration. This acquisition configuration results in a maximum fold of 24 and a signal to random noise improvement of almost 5.

In a small refinement to the acquisition arrangement, all shot holes were drilled laterally offset from the line of geophones by 2m. The reason was to ensure that all waves passed through undisturbed ground, avoiding the compacted and fractured soil around the detonated blank cartridge, so that the receiver static at each geophone station was not altered during acquisition. Where possible, the shot holes were drilled to a depth of 1 m below the ground surface. Shot holes were tamped with water before detonating the explosive cartridge in the buffalo gun, a shooting technique which has been proved to aid shot coupling and diminish the strength of the air coupled wave (Miller et al., 1994).

At Parkside, shot points were located midway between the geophone stations in the in-line direction to fulfil the criterion for the stack array (Anstey, 1986). The idea is to have a uniform distribution of source-receiver offsets in the CMP gather for maximum suppression of ground roll.

The digital data migration process moves reflection events to their true locations in offset-time space. Dipping horizons are moved up dip and shortened in length. Yilmaz (2001) shows seismic data must be collected over an extra length beyond the sub-surface structure. The extra length is given by:

$$M = \frac{Vt \sin\theta}{4} \tag{3.4}$$

where t is the two-way time to the reflector. To ensure that the migration process will focus seismic energy from points at the edge of the prospect correctly the total length of the full coverage of a 2D profile should be further enlarged by the radius of the first Fresnel zone R (e.g. Sheriff and Geldart, 1995):.

$$R = \frac{V}{2}\sqrt{\frac{t}{f}} \tag{3.5}$$

where V is the average P-wave velocity to the target, t is the arrival time and f is the frequency. A particular target for the Parkside seismic survey was a cavity logged in the Geneva borehole. Fortunately, the borehole was located away from the field boundaries (Figure 3.1), and so 2D seismic profiles could be aligned to try to image the cavity without restrictions.

A digital sampling interval of 0.5 ms was selected for recording. The Nyquist frequency f_N is defined by the equation (e.g., Sheriff and Geldart, 1995):

$$f_N = \frac{1}{2\Delta t} \tag{3.6}$$

where Δt is the sampling interval. With a sampling interval of 0.5 ms only frequencies above 1000 Hz will be aliased. Analogue filters were applied to the output signals from the geophones before A-to-D conversion. The high-cut anti-alias filter had its 3 dB point at 500 Hz and a roll-off of 24 dB/octave, and the low-cut recording filter had its 3 dB point at 10 Hz, also with a 24 dB/octave roll-off. The SM-7 geophones deployed for the acquisition have a natural resonant frequency of 30 Hz, and are capable of recording frequencies up to 300 Hz with negligible distortion, covering the range of signal frequencies expected in shallow seismic reflection profiling.

The total recording time must be adequate to cover reflections from the target horizons and, preferably, to allow for the possibility of early triggering of the recording system. It must also be sufficiently long to accommodate digital processing steps such as estimation of the autocorrelation function for computing the Wiener filter in deconvolution and migration of diffraction energy arising from the target horizons. A total recording time of 512 ms was considered to be ample.

A wide loose grid of four 2D seismic profiles was laid out at the Parkside survey area (Figure 3.4), and was acquired using the shooting template shown in Figure 3.5 with the instrument, source and receiver parameters defined in Table 3.1. Profiles 01 and 02 were arranged to intersect each other over the location of the Geneva borehole. Later, more accurate post-plotting positioned the borehole 8 m to the south of the intersection point of profiles 01 and 02. The two long profiles, 01 and 04, were 215 m in length between the start and end receiver stations and were orientated parallel to the Neasham Road hedge line. The two shorter profiles, 02 and 03, ran from the Neasham Road hedge, cutting profiles 01 and 04 obliquely, and were curtailed by the fence line at the south-west boundary of the field.

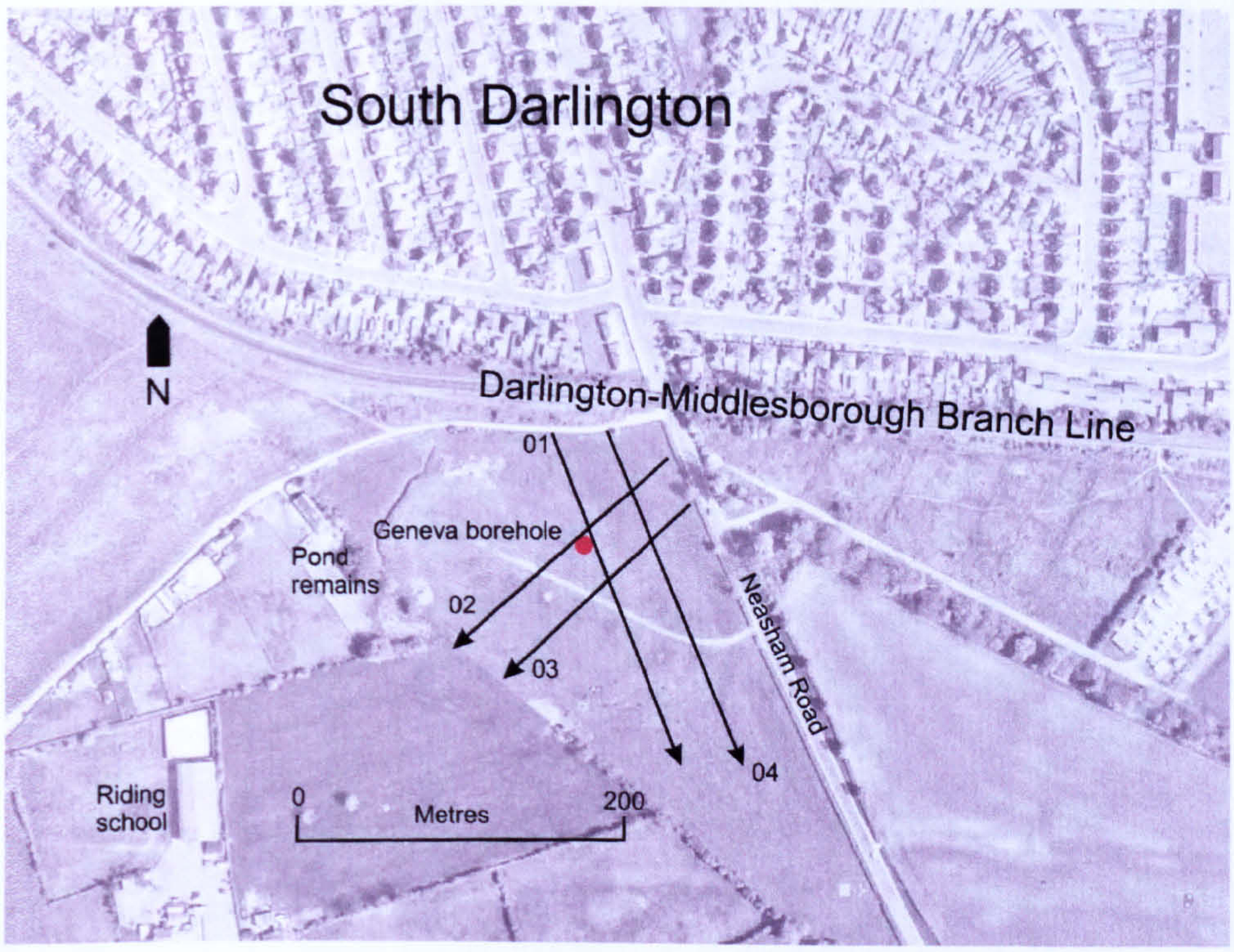
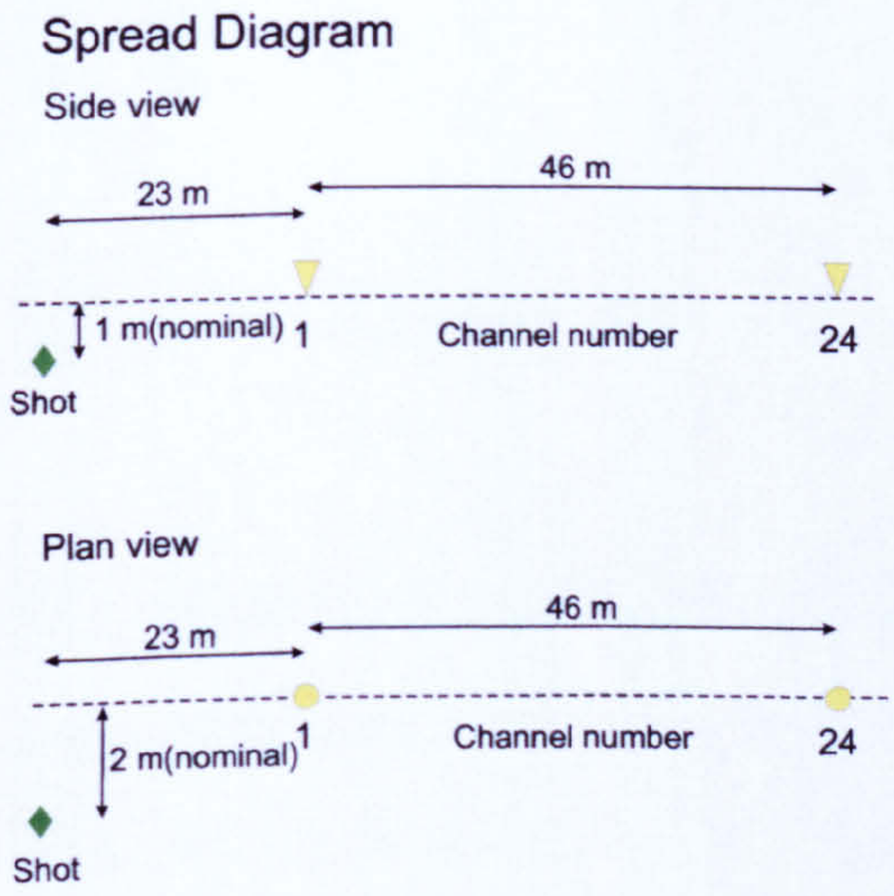
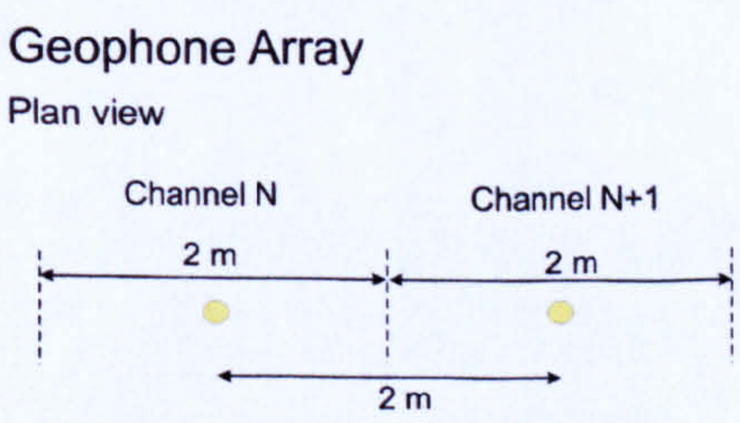


Figure 3.4: Parkside survey 2D seismic profiles layout.





Diagrams not to scale

Figure 3.5: Parkside 2D seismic profiles shooting template.

Instrument Parameters	
Recording instrument	Geometrics SmartSeis S12
Format	SEG-2
Data channels	24
Pre A/D converter low cut filter	10 Hz
Pre A/D converter high cut filter	500 Hz
Sample rate	0.5 ms
Record length	512 ms
Delay	0 ms

Source Parameters	
Source type	Buffalo gun, 5 g black powder blanks
Shot interval	2 m
Shot depth	1 m
Shot in-line skid relative to geophones	1 m
Shot cross-line offset relative to geophones	2 m
Off end shooting arrangement, forward and reverse shots to simulate symmetric split-spread.	
All shot holes tamped with water before firing.	

Receiver Parameters	
Geophone type	SM-7/30 Hz
Group interval	2 m
Geophones per group	1
Near-offset	23 m
Far-offset	69 m

Table 3.1: Parkside 2D profiles acquisition parameters.

3.2 3D seismic acquisition parameters and survey design

Good results were achieved by the 2D seismic profiles collected at the Parkside survey site. The final time-migrated section of profile 04 (Figure 3.6) imaged several reflections including a very shallow event at 30 ms TWT. Therefore, it was decided to acquire a 3D seismic volume over the Geneva borehole with small alterations to the acquisition parameters from those used to acquire the 2D profiles. A number of 3D case studies have reported on

structures imaged at shallow depths within unconsolidated sediments (Lanz et al., 1996; Siahkoohi and West, 1998, Büker et al., 1998, Spitzer et al. 2001).

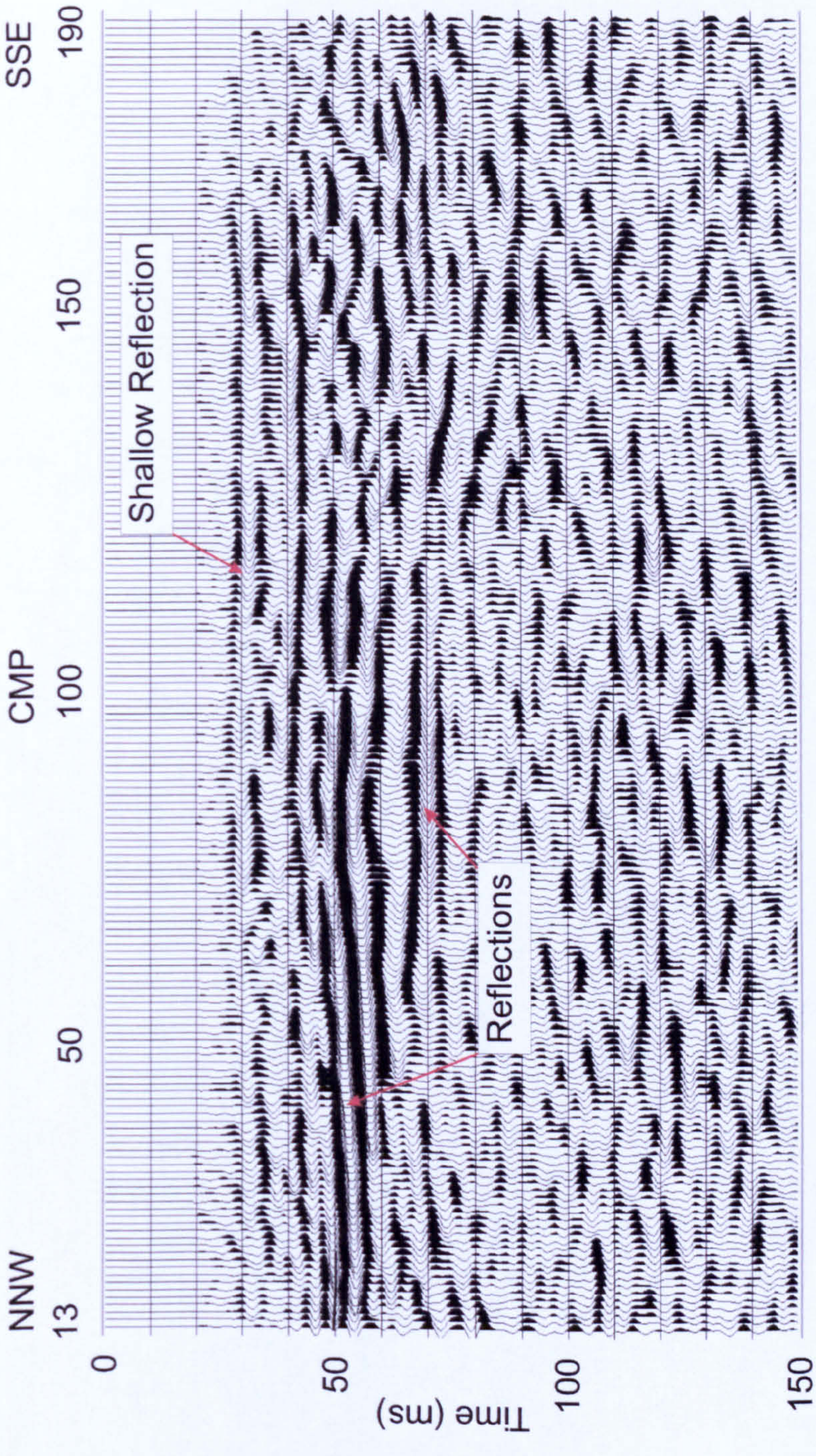


Figure 3.6: Final time migrated section of Parkside 2D profile 04.
The section is displayed with a scalar multiplier. The distance between CMP traces for all Parkside 2D profiles is 1 m. The CMP numbering has been adjusted to represent the distance along the profile from the first receiver station.

The in-line and cross-line extent of the 3D survey (Figure 3.7) was constrained by the shape of the field, a large mobile telephone installation on the roadside fence close to the main field entrance, and the presence of an extensive mound of building rubble at the end of the rough track. The location of the obstructions influenced the basic acquisition template (Figure 3.8), which was an off-end shooting arrangement with a shot firing into a linear spread of 24 geophones. The near-offset was reduced from 23 m to 16.5 m without incurring any significant interference from the high-amplitude ground roll. The geophone station spacing was increased to 3 m, still sufficient to preserve high-frequency reflection energy without spatial aliasing, and gave a far-offset of 85.5 m.

All the seismograph instrument parameters and geophone type (Table 3.2) were kept unchanged from the Parkside 2D acquisition set-up. However, instead of the blank saluting cartridges containing 5 g of black powder, larger yachting blanks of 7 g of black powder were used.

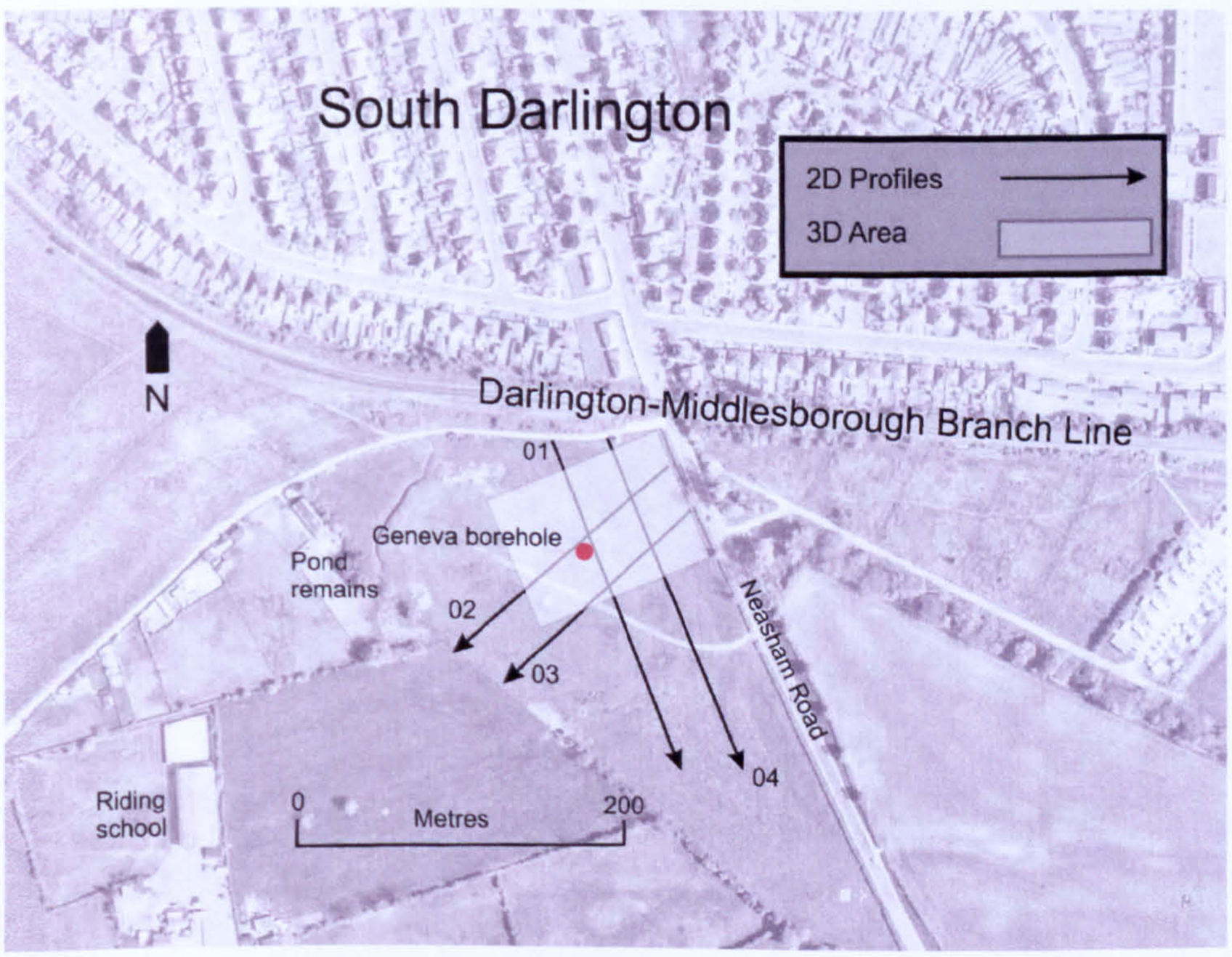


Figure 3.7: Parkside 3D seismic volume layout.

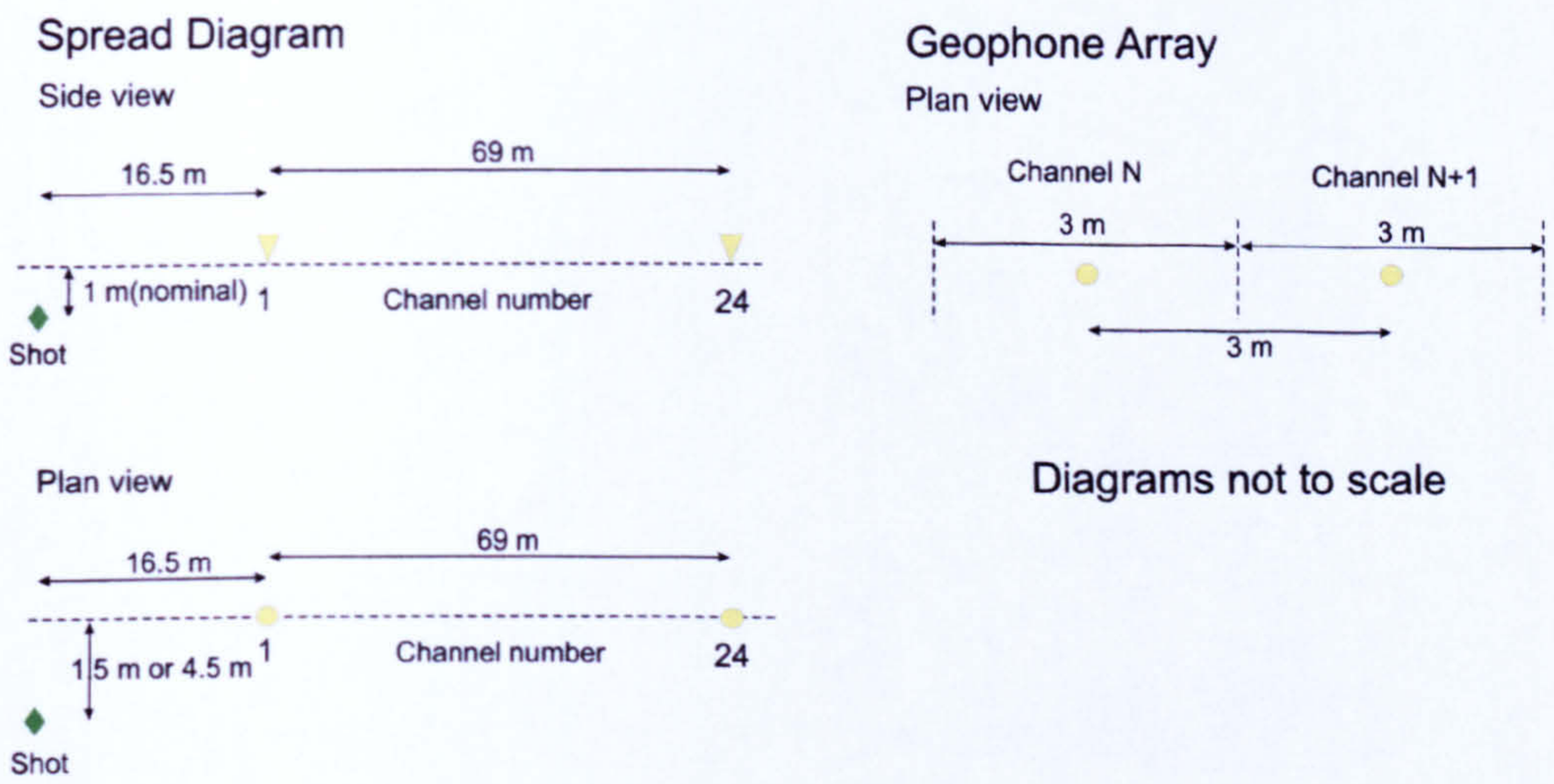


Figure 3.8: Parkside 3D seismic volume shooting template.

Given the geographical constraints, 28 parallel receiver lines were laid out running south-west towards the end of the rough track from the Neasham Road (Figure 3.9). Each receiver line had just 36 receiver stations. The distance between receiver stations was 3 m in-line and cross-line, giving a sub-surface bin size of 1.5 m by 1.5 m. The first receiver station on each line was 18.5 m from Neasham Road hedge and the last station was 123.5 m from the hedge along the line of the profile.

The 3D survey was also positioned to maximize the use of the excellent shot coupling where stiff clay capped the ground surface in the north-east corner of the triangular field. Towards the Geneva borehole the ground conditions become sandy and so the shot coupling conditions became poorer.

The shot holes were each drilled to a depth of 1 m on a grid spacing of 6 m in-line and cross-line. The shot grid consisted of 15 lines of shots orientated parallel to the receiver lines with 15 holes drilled in each line. The first shot point in each line was located 2 m from the Neasham Road hedge. The shot grid was offset from the receiver grid by 1.5 m in both in-line and cross-line directions.

The basic shooting pattern was rolled along the line of receiver stations until only 8 live channels were recorded at the last shot point in each line. Then the geophone spread was shifted to the next line of receiver stations. In total, 56 parallel sub-surface lines were

acquired for the Parkside 3D seismic volume. The Parkside 2D profiles proved that the sub-surface geological interfaces are approximately planar, and therefore could be adequately managed by the very narrow azimuthal coverage of the 3D acquisition scheme.

Instrument Parameters	
Recording instrument	Geometrics SmartSeis S12
Format	SEG-2
Data channels	24
Pre A/D converter low cut filter	10 Hz
Pre A/D converter high cut filter	500 Hz
Sample rate	0.5 ms
Record length	512 ms
Delay	0 ms
Source Parameters	
Source type	Buffalo gun, 7 g black powder blanks
Shot in-line interval	6 m
Shot cross-line interval	6 m
Shot depth	1 m
Shot in-line skid relative to geophones	1.5 m
Shot cross-line offset relative to geophones	1.5 m or 4.5 m
Off-end shooting arrangement.	
All shot holes sprung with a dummy shot and tamped with water before firing.	
Receiver Parameters	
Geophone type	SM-7/30 Hz
Group in-line interval	3 m
Group cross-line interval	3 m
Geophones per group	1
Near-offset	16.5 m
Far-offset	85.5 m

Table 3.2: Parkside 3D seismic volume acquisition parameters.

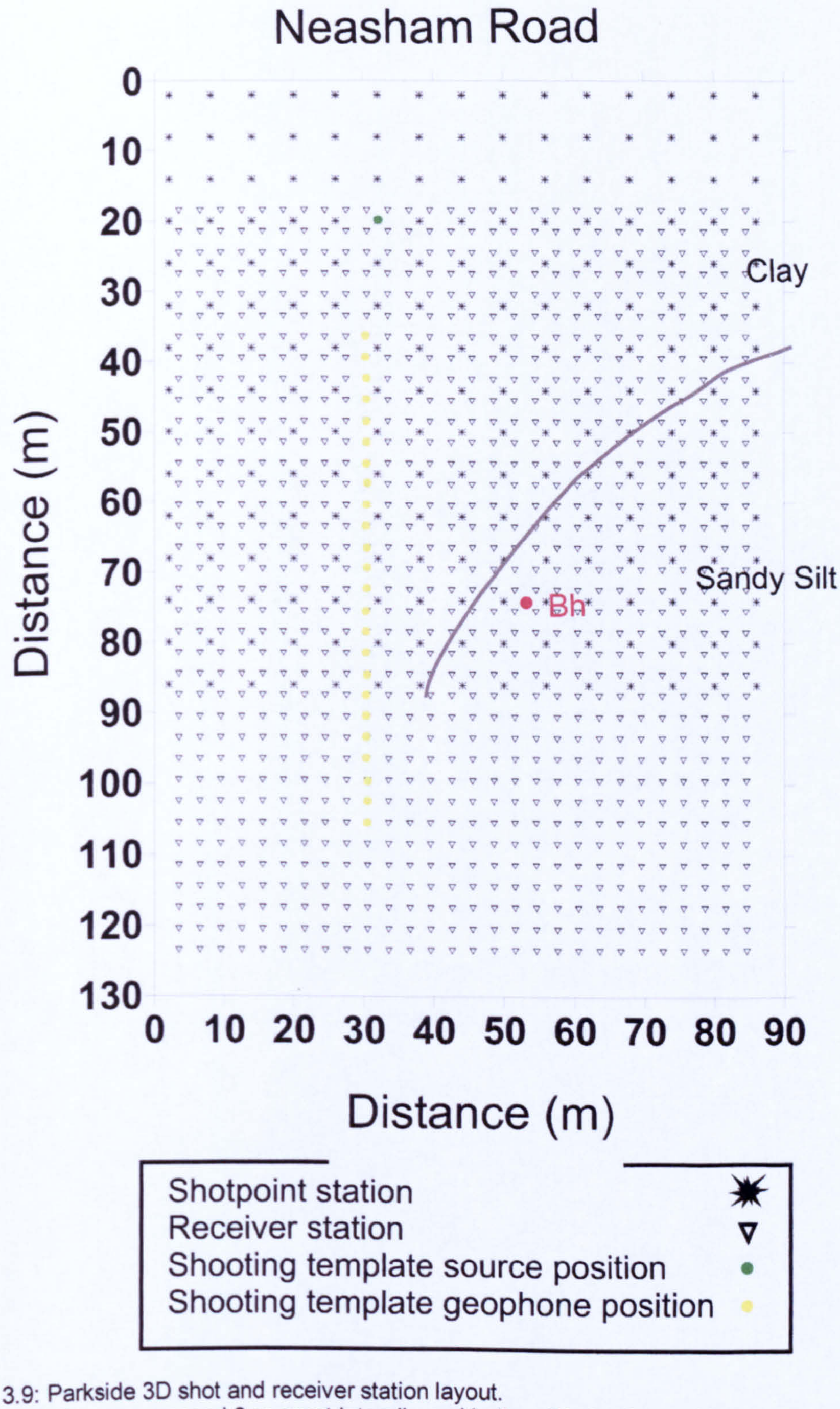


Figure 3.9: Parkside 3D shot and receiver station layout.
Receiver stations are spaced 3 m apart laterally and in-line. Shot point positions are on a 6 m by 6 m grid. The end-on acquisition template is indicated by the yellow and green coloured dots. The location of the Geneva borehole and the different shot coupling mediums are also shown.

3.3 Fieldwork procedures and equipment

3.3.1 2D seismic profile and 3D seismic grid positioning

At Parkside the main focal point of the 2D seismic profiles was the Geneva borehole, which was located as accurately as possible on the Ordnance Survey map from the grid co-ordinates of the borehole provided by the British Geological Survey database. Distances were measured on the map from the borehole position to prominent points in close proximity, clearly marked on the map, such as field boundary corner points. The location of the Geneva borehole was then marked on the ground from the prominent features using tape measures of 30 m and 50 m lengths.

Profile 01 was located to pass through the Geneva borehole, at a distance of 70 m away from and parallel to the Neasham Road hedge line. The locations of the first and last receiver stations of profile 01 were measured relative to prominent features on the Ordnance Survey map, and all receiver stations were pegged out at 2 m spacing. The distances of other significant markers, such as gateways, track crossings and fence lines, from the nearest receiver station along the profile were also noted. With the receiver line established, the positions of the shot holes relative to the receiver stations were measured off from the line of receivers in accordance with the acquisition parameters.

The shorter profile 02 was then located to cross over profile 01 at the position of the Geneva borehole. Profile 03 was located 30 m south-east of and parallel to profile 02. The final profile at Parkside, profile 04, was placed 30 m away from and parallel to profile 01, nearer to Neasham Road.

To mark out the receiver and shot stations of the Parkside 3D seismic volume, two baselines were established at right angles using Pythagoras' theorem. One tape measure was run out 40 m along the side of the Neasham Road hedge line from a fixed point in the north-east corner of the survey field. A second tape measure was run 30 m from the same fixed point along a line approximately perpendicular to the hedge line. A third tape measure of 50 m length was employed to connect the two end points of the other tapes. The three tape measures were adjusted until a satisfactory right angled triangle was formed. The baselines were then extended linearly to the ends of the survey area. The in-line and cross-line

locations of the receivers and shot stations were then measured out from the two baselines with constant cross-checking for accuracy.

Positioning errors are inevitably present in both the source and receiver station positions. According to Büker et al. (1998), the maximum acceptable error as a function of timing and depth to target can be expressed as:

$$\Delta s_{\max} \leq \Delta t_s V \sqrt{5/2} \qquad (3.7)$$

where $\Delta s_{\max}$ is the maximum positioning error, Δt_s is the maximum acceptable timing error, and V is the P-wave velocity in the medium at the target depth. At Parkside, taking the maximum acceptable timing error as the acquisition sampling interval, 0.5 ms, and the P-wave velocity at the target horizon (top of the Hartlepool Anhydrite Formation) as 2000 m s^{-1}, the a maximum positioning error is 1.6 m. Where the terrain is open and flat, such as at Parkside, with good survey notes, 2D profiles and 3D grids can be re-located with confidence within the maximum positioning error, even when station positions have been marked out with tape measurements.

3.3.2 Source

The buffalo gun is of a simple construction, made from steel scaffolding tube welded together. At the base is a machined breech in which the blank cartridge is placed. A thin steel rod is dropped down the centre of the tube to detonate the cartridge by impacting on the percussion cap.

Very small charges of 5 g and 7 g of black powder were employed in the acquisition of the 2D and 3D Parkside seismic surveys. The small charges generate a wide bandwidth wavelet, a necessary requirement to image sub-surface geological features on the metre scale.

The buffalo gun was placed at the bottom of a nominally 1 m deep hole, drilled into the soil manually by a hammer and stake. All the shot holes for the 2D profiles Parkside were tamped with water prior to detonation to improve the shot coupling and minimize the air wave.

During the 3D survey, the shot holes were also initially sprung by firing a dummy shot to compact the surrounding soils, possibly enabling a greater proportion of the energy released to be transferred into useful wave energy by the second recorded shot.

The detonation of the blank cartridge causes recoil of the buffalo gun. A trigger switch sensitive to motion mounted on one arm of the buffalo gun generates an electrical pulse in response to the sharp motion from the buffalo gun on charge detonation. This signal is passed down a 150 m twin-core cable made of a very low resistance copper wiring, the trigger cable, to the seismograph to start data recording. By dropping the firing pin only a few decimetres on to the percussion cap of the blank cartridges, variations in the trigger timing are usually within a millisecond. Large trigger delays are caused by poor firing technique (Figure 3.10). Ramming the firing pin down inside the scaffolding tube, or dropping if from an excessive height results in an early trigger. Mud lodged within the central tube can obstruct the passage of the firing pin. The trigger sensitivity can be adjusted in the Geometrics SmartSeis S12 seismograph software to suit the field conditions. Large or small early trigger delays can be accounted for when the field statics are computed during digital processing, but shots that were recorded with severe trigger delays were usually discarded and the shot record re-acquired.

3.3.3 Receivers and the roll-along switch

SM-7 vertical geophones manufactured by SENSOR with natural resonant frequency of 30 Hz were employed on all the seismic 2D seismic profiles and the 3D seismic volume acquired at Parkside. The amplitude response of this design of geophone decays rapidly for frequencies below the natural frequency and above the natural frequency it has a flat response up to 300 Hz. The geophone effectively acts as a high pass filter.

If excited at the natural frequency of the mechanical system the displacement of the undamped coil is theoretically infinite. In reality a geophone is damped by approximately 20% due to eddy currents in the coil former. A 3.3 kΩ shunt resistor was soldered across the coil terminals of single geophones, damping the amplitude response at the natural frequency of the geophone by a factor of 70%. This is designed to reduce the amplitude of unwanted seismic noise at frequencies close to the geophone resonant frequency, particularly ground

roll. To ensure that the response of the geophone beyond the natural frequency is flat and that good quality raw shot records are maintained throughout acquisition, the geophones were firmly planted, vertically, into ground cleared of any debris, as recommended by Knapp and Steeples (1986).

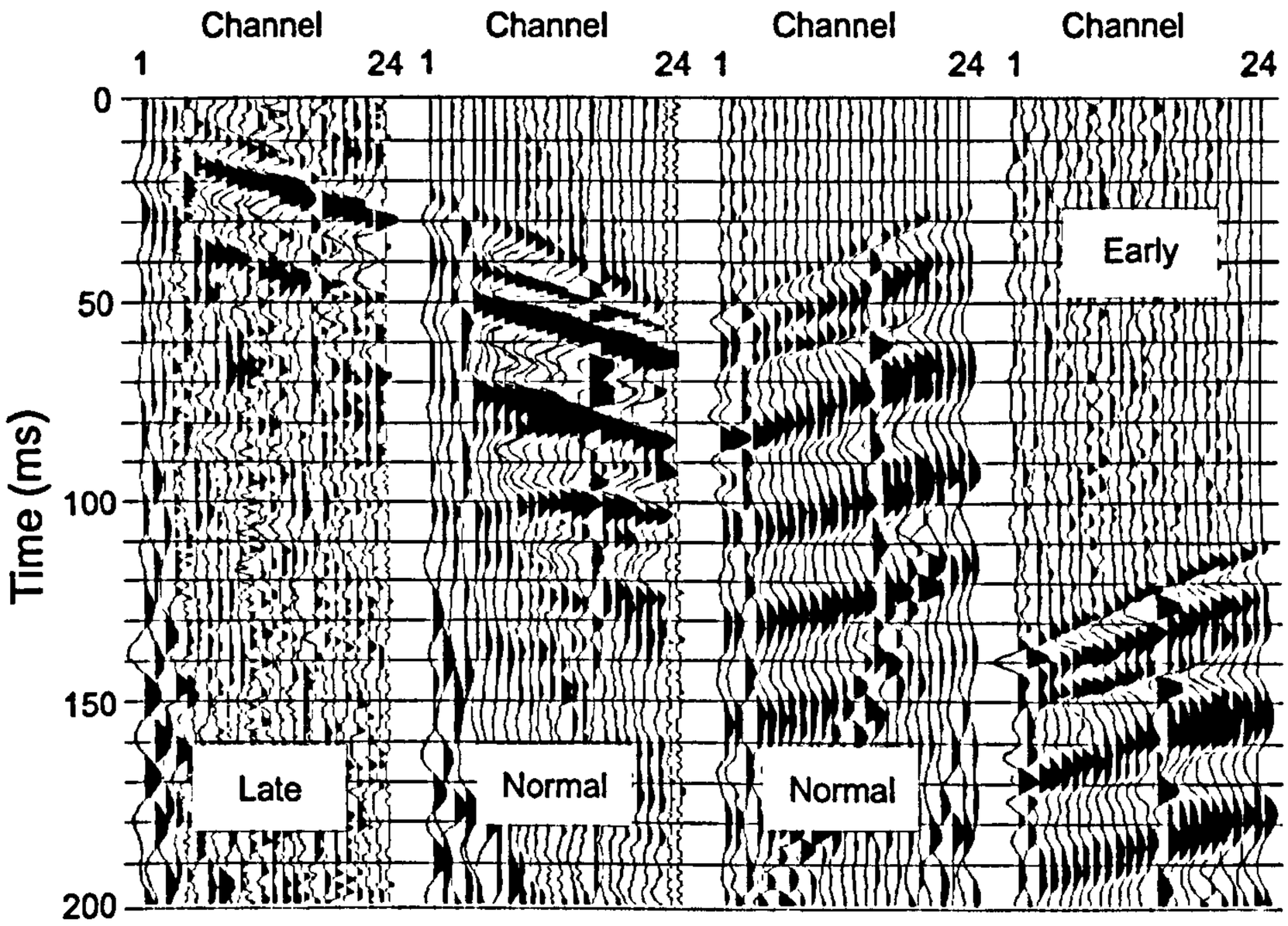


Figure 3.10: Different shot trigger delays.
Panel 1 is an example late trigger; the first breaks of the near traces are unrecoverable. Panel 4 is an example of an early trigger. The reverse polarity traces are built into the acquisition design as a field QC check. The example trigger delays are from the Hell Kettles survey data set and are displayed with scalar multiplier.

Wind noise appears on the raw shot record as low amplitude, high frequency jitter (Figure 3.11) and is increased where the vegetation cover is unkempt. The wind jitter can be mitigated by burying the geophones (Bland and Galland, 2002). However, this strategy is time consuming and increases operational costs. Laying the geophone cabling as flat as possible on the ground surface and waiting for breaks in the wind speed during recording is a more efficient method of minimizing the effects of wind noise. However, the disadvantage with this approach is that in damp conditions electrical cross-feed occurs between the different channels (Figure 3.12), an effect that can be alleviated by resting the geophone take-outs on wooden pegs.

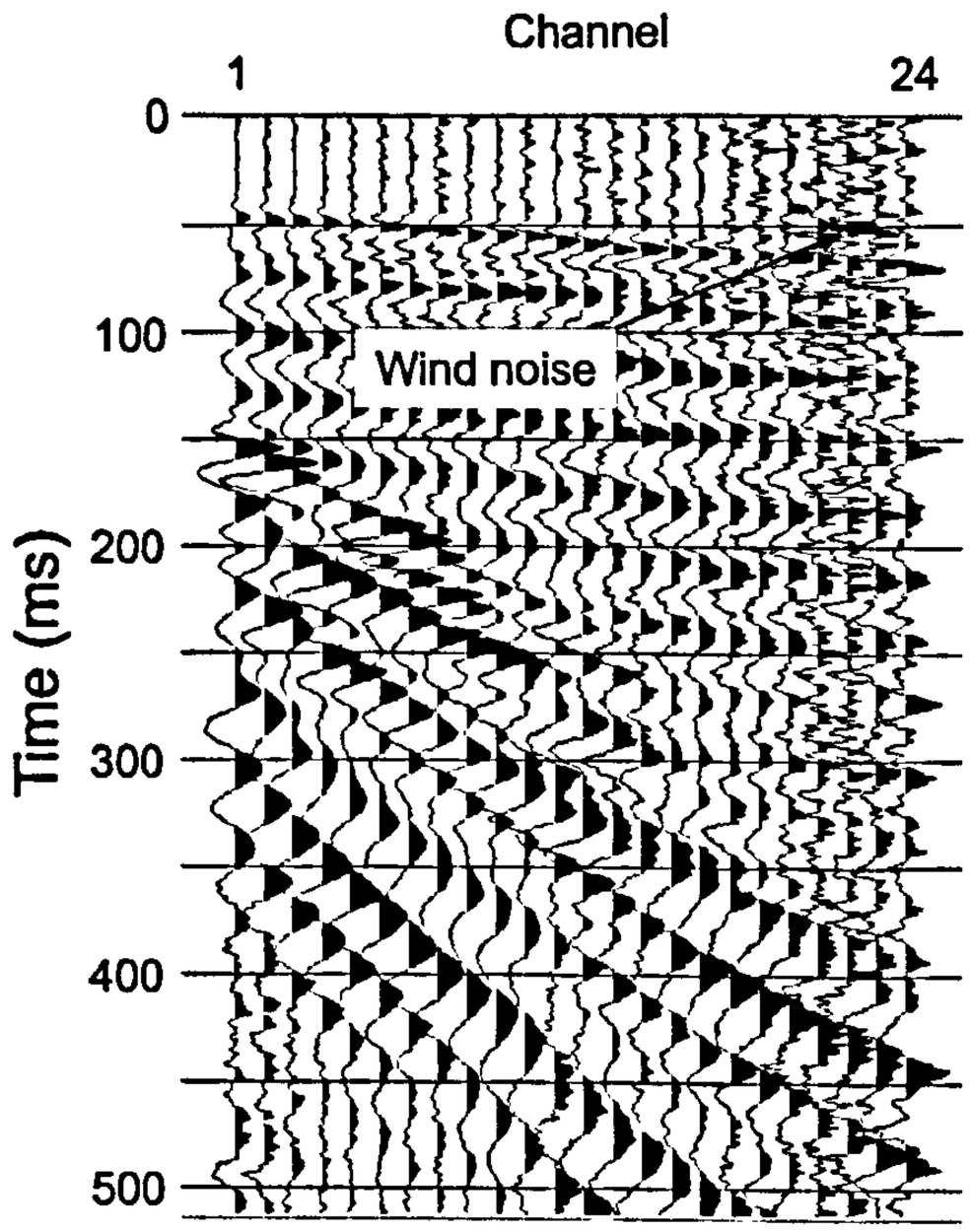


Figure 3.11: Effect of wind noise on shot record data quality.
Shot record is from the Hell Kettles survey site and is displayed with a 200 ms AGC sliding window.

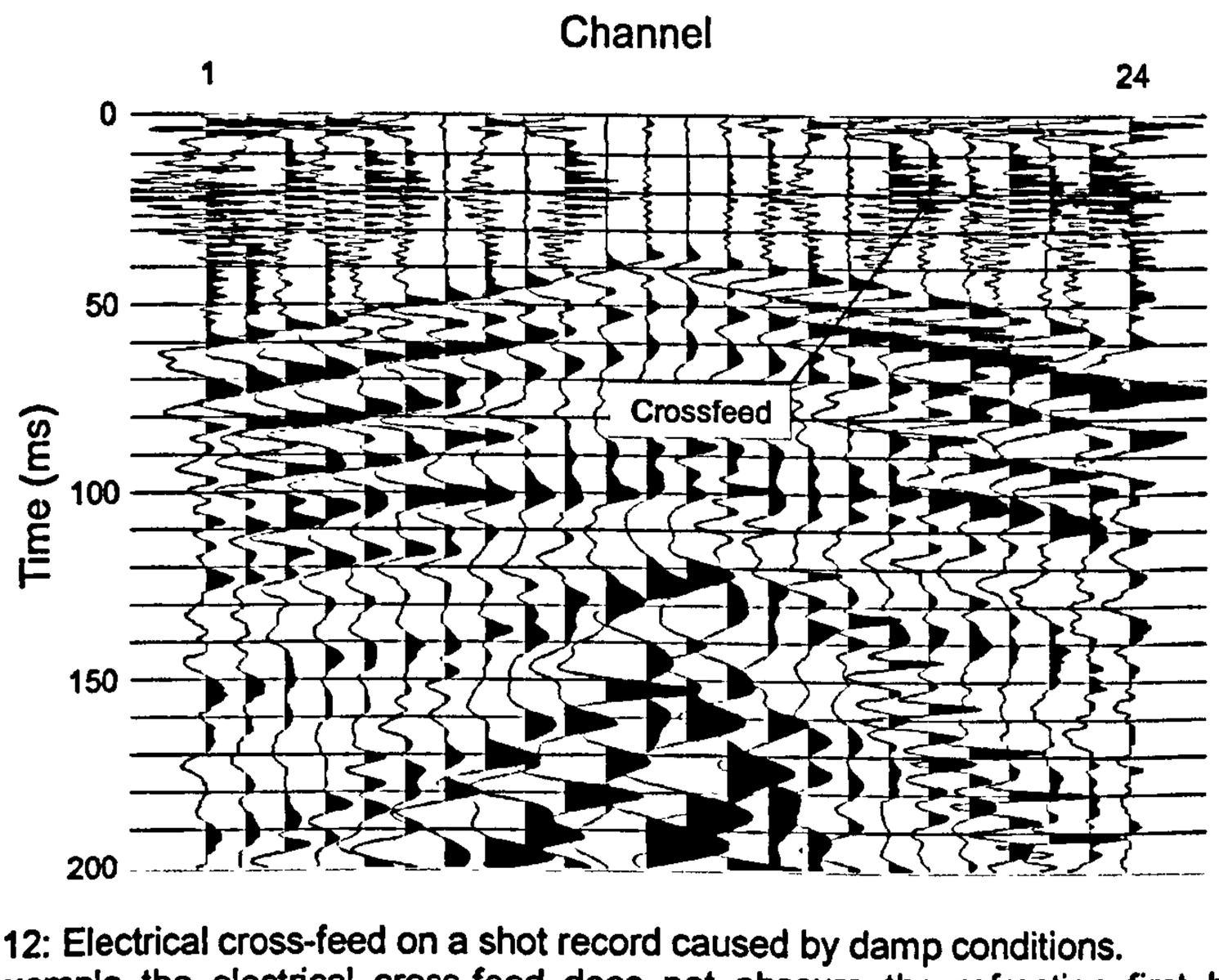


Figure 3.12: Electrical cross-feed on a shot record caused by damp conditions.
In this example the electrical cross-feed does not obscure the refraction first breaks or contaminate the wider seismic signal. Therefore, this shot record was acceptable. The seismic data is from the Hell Kettles survey site and is displayed with a 200 ms AGC sliding window and then cropped at 200 ms.

Each of the planted geophones clip on to a multi-core geophone cable with take-outs moulded on at equal intervals. A take-out consists of two connectors of different widths so that the geophone can only clipped on in one way, preserving the signal polarity. All different vintages of the geophone cables used can handle the signals from up to 12 geophones simultaneously and were of a double-ended construction, so that they are reversible and identical from either end.

Geophones can potentially be deployed along the entire length of a 2D seismic profile or across the whole of a 3D seismic grid. The electrical signals from the geophones passed along the multi-core cabling can be fed directly into the seismograph for recording, but more commonly via a roll-along switch. A roll-along switch or switches select the correct combination of geophones on the ground for a particular source location, according to the acquisition design. At each move-up step in the CMP acquisition method, the roll-along switches are adjusted to record data from the correct set of geophones.

The quality of the time-migrated seismic data will be severely degraded with the wrong selection of shot or geophone positions. Therefore, a series of reverse-polarity geophones were inserted at known points in the spreads for both 2D and 3D acquisition. Any unexpected change in the position of the reverse-polarity traces on the seismograph display could then immediately be investigated.

3.3.4 Seismograph

The Geometrics SmartSeis S12 engineering seismograph (Figure 3.13) used for data acquisition has a capacity to record 24 channels simultaneously. The incoming analogue electrical signal is transformed into digital format by passing through a 15 bit plus sign bit converter. Therefore, the theoretical dynamic range of the system is:

$$20\log\frac{A_1}{A_2} = 20\log 2^{15} = 90dB, \tag{3.8}$$

where A_1 is maximum the level of the output signal and A_2 is the minimum resolvable signal amplitude. In reality, the dynamic range is less than 90 dB due to the presence of internal instrument noise.



Figure 3.13: Picture montage of the field acquisition equipment.

In operational mode, the background noise from passing traffic, aeroplanes or wind noise was viewed on the 28 cm liquid crystal display (LCD) as a constantly updating waterfall

display. The raw shot record was stored in temporary memory whilst various filters, different gain functions, time scales and viewing formats were applied for data quality control. If further examination was required, a hard copy of the data could be printed out. Raw seismic data passing quality control were stored electronically in SEG-2 format (Pullan, 1990) on a large hard drive built-in to the system. Power for the whole system was provided by a sealed 12V re-chargeable lead-acid battery.

4.0 Processing

4.1 ProMAX digital data processing software

ProMAX operates on a Linux workstation and provides an interactive primarily mouse-driven user environment for the processing of seismic data. The software is developed, maintained and supported by the Landmark Graphics Corporation. ProMAX is used by many processing houses in the hydrocarbon exploration industry; therefore, it is reasonable to assume that all the individual processing modules within ProMAX are robust.

The ProMAX user interface is broken down into three different levels, areas, lines and flows, which enable the user to streamline the processing of the raw seismic data in a logical manner. The uppermost level is called the area level. Each area is assumed to have one or more lines. New areas can be added by clicking a mouse button on the global command "Add". Other global functions enable areas to be renamed, deleted or copied. Many lines can be nested within a single area. All information related to a specific seismic line is stored at this second level, such as the raw shot records, geometry definition and velocity fields. Global menu functions also operate at the line level. The third level is the flow level, which appears under ProMAX in a window containing the flow builder menu (Figure 4.1). Many flows can be listed under a particular line. The ProMAX software automatically builds and alters an associated Linux directory structure to handle the files made and destroyed in seismic processing as the user adds, deletes or renames the various areas, lines and flows for each project.

The Flow Builder window is divided into two halves. The left hand side is the Editing Window, where the processing flow is progressively built, whilst the right hand section is the Processes List, in which all the available modules are grouped under headers ordered in an approximate sequential processing order. Each individual module can be selected or deselected from the processing flow and parameterized by a single mouse click. On execution of a processing flow, the values of the trace headers can be monitored as the seismic data pass through the processing modules sequentially. Conditional flow control

statements, such as IF and ELSE, can be built into a processing flow and are widely used in the testing of module parameters.

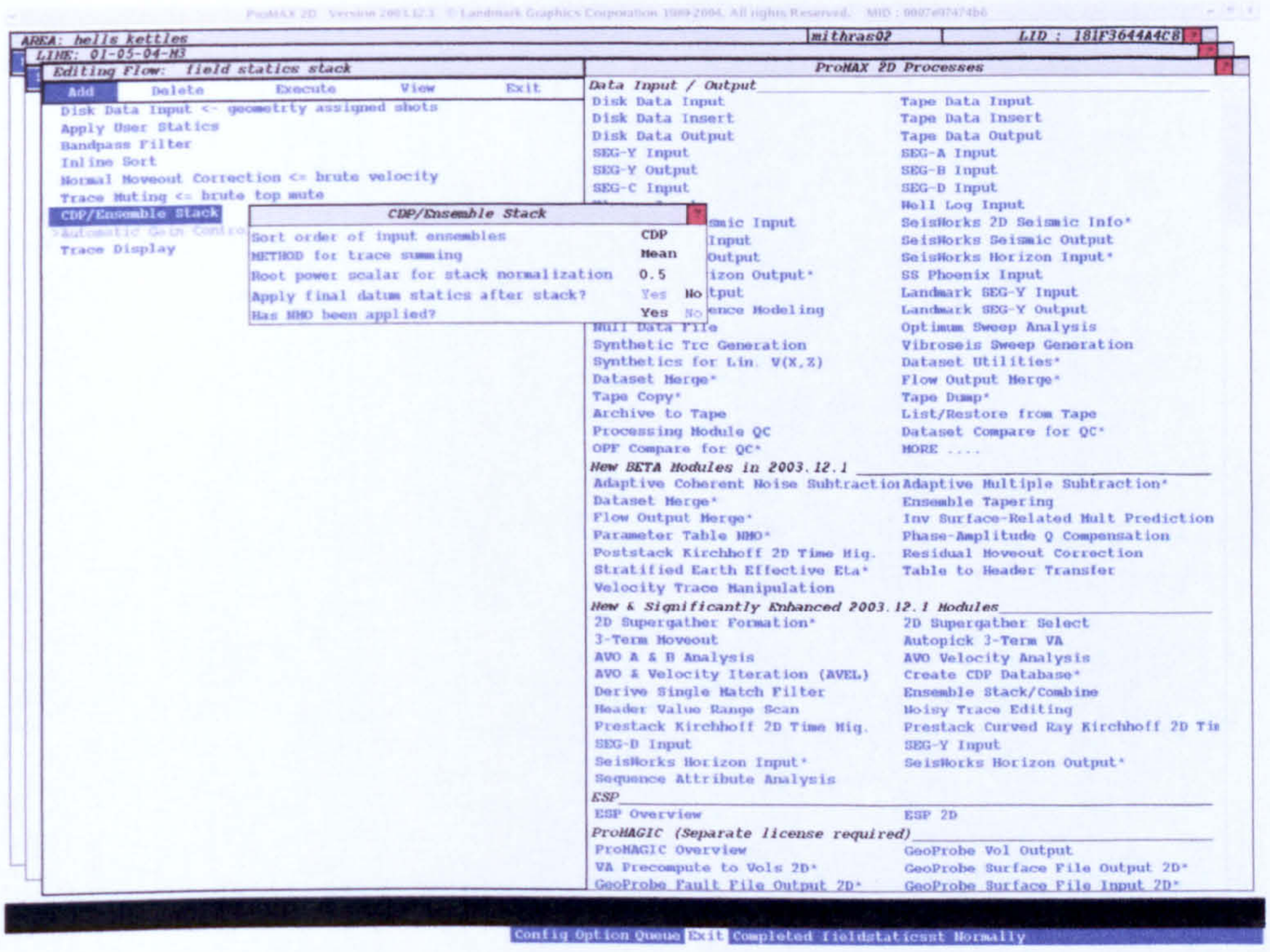


Figure 4.1: ProMAX flow builder user interface.

Deeply buried within the ProMAX system architecture are the database files which serve as a central core of information, such as data on geometry, statics, surface consistent values, and links the data to the different seismic domains, source, receiver and common midpoint (CMP). Tools are provided by ProMAX for the user to directly interrogate, manipulate and display the database attributes. This is a powerful resource; the manual alteration of the database information must be handled with care to ensure that the execution of the processing flow proceeds without errors.

4.2 Hell Kettles 2D seismic processing flow design

The objective of seismic digital data processing is to produce an interpretable image of the sub-surface geology from the raw field shot records. I selected profile 04 from the initial grid of profiles circumnavigating the Hell Kettles ponds (Figure 4.2) as the principal profile to use for choosing 2D seismic processing parameters at Hell Kettles, and I use it in this section to

illustrate the stages in the processing sequence. Each step in the development of the processing sequence was thoroughly tested and parameterized to remove seismic noise and/or enhance coherent reflected energy.

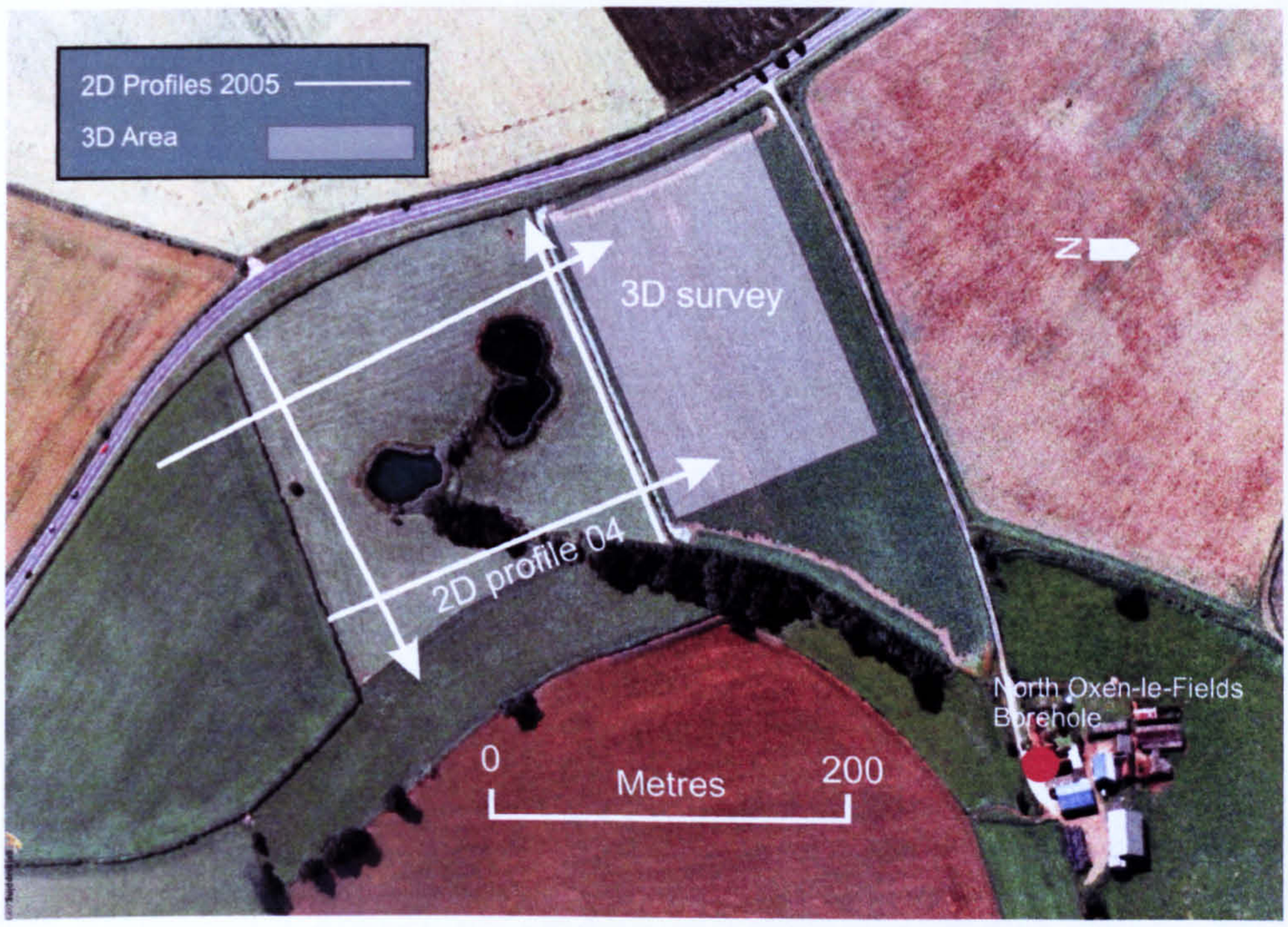


Figure 4.2: Aerial photograph taken in 2000 of the Hell Kettles survey site.

The nature of the near-surface materials has a significant impact on the seismic content of raw shot ensembles. The near-surface conditions can alter rapidly over small distances, so the processing flow was reviewed against the other profiles acquired on the same survey site and the parameters modified so that the final processing solution was suitable for all profiles over the survey area. This site-consistent approach was adopted so that the character of the seismic data in the final time-migrated sections would be similar across the whole survey area, hence aiding the interpretation process.

2D profile 04 is orientated SW—NE and crosses the complete length of the field containing the Hell Kettles ponds, extending into the adjacent field to the north. The near-surface materials are fluvial deposits typical of a river floodplain environment and the profile transects different ground conditions from water-saturated areas to very dry gravelly soil. The varying shot coupling environment generates raw shot records with different reflection,

refraction and noise characteristics and strengths that are required to be handled in processing.

The complete 239 m length of profile 04 was acquired over two days in dry, sunny conditions with light to moderate wind speeds. Shots were fired at 2 m intervals into an off-end spread of 24 geophones spaced 2 m apart with a near-trace offset of 23 m (Figure 4.3). A common midpoint (CMP) spacing of 1 m with a maximum fold of coverage of 24 was achieved by shooting from the same shot hole into geophone spreads in both directions.

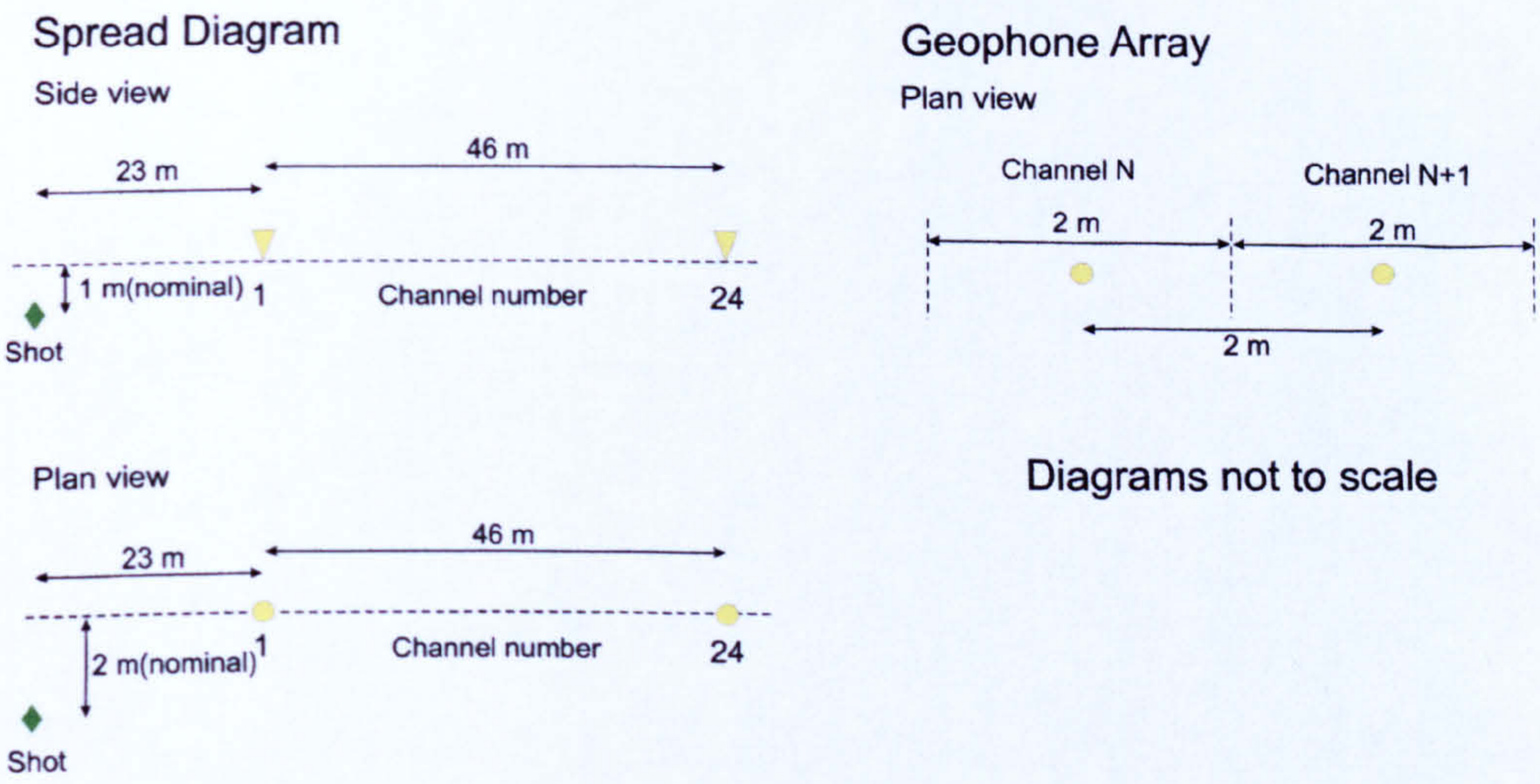


Figure 4.3: Hell Kettles 2D profile 04 shooting template.

4.2.1 Pre-conditioning

All of the raw seismic data collected in the field in SEG-2 format were uploaded to the Linux workstation platform and converted into the internal ProMAX data format. File interrogation input/output efficiency, and therefore processing speed, is greatly improved when the files are encoded in the ProMAX file format. During the file conversion procedure all unnecessary shot files, such as those tagged as "Do Not Process" in the observer's notes, were stripped out.

Hell Kettles profile 04 has a simple a straight line 2D geometry with a symmetric fold of coverage, building up evenly from the start of profile to a maximum of 24 and falling off evenly at the end of profile. Several tools are available in the ProMAX processing package to quality control the profile geometry. The CMP stacking chart is particularly effective in finding errors in the geometry assignment (Figure 4.4).

Poor traces, either due to faulty geophones that were not recognised in the field during acquisition or due to high levels of environmental or cultural noise, were selected or killed by visually scanning through all the shot records. Reverse polarity field quality control geophones were also flipped at this stage in the processing sequence.

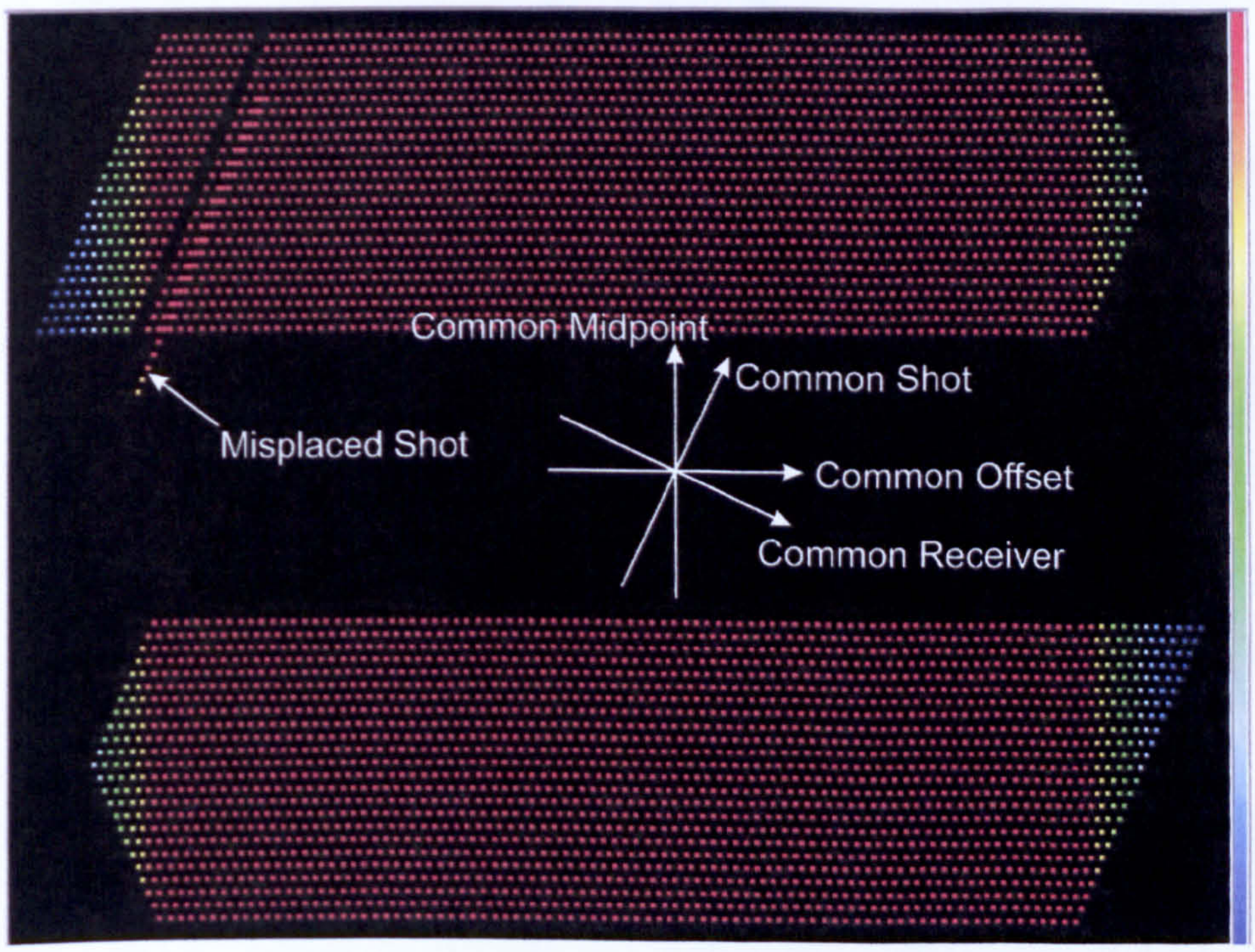


Figure 4.4: Acquisition geometry QC stacking chart.
One shot record is forced out of position by a cross line shift of 10m. The orientation of the four major processing planes, midpoint, shot, receiver and offset are indicated. High fold of coverage is coloured red.

Figure 4.5 shows the result of summing all the edited shot records of profile 04 to create a very brute stack section. The estimated P-wave stacking velocity used for normal moveout (NMO) corrections was based on the geology of the nearby North Oxen-le-Fields borehole (Figure 4.6). At shallow depths, Fairbairn et al. (1986) note the P-wave interval velocity through the Sherwood Sandstone Group as 2000 m s^{-1}. The base of the Sherwood Sandstone Group is difficult to discriminate between the siltstones and mudstones of the Roxby Formation (Smith, 1989), at the Seal Sands (Figure 2.6) 26 km to the east on Teesside at a depth of 5500 m the P-wave interval velocity grades smoothly through the Sherwood Sandstone Group and the Roxby Formation at 3400 m s^{-1}. The P-wave interval velocity of the overlying Quaternary deposits was estimated at 1800 m s^{-1} based on the water table

refraction velocity. The lower half of the section is cross-hatched by low-frequency linear noise trains. The top 120 ms of the stacked section is dominated by continuous low-frequency reverberating events. The reflection energy is present as high-frequency arrivals superimposed on the shot-generated reverberating noise.

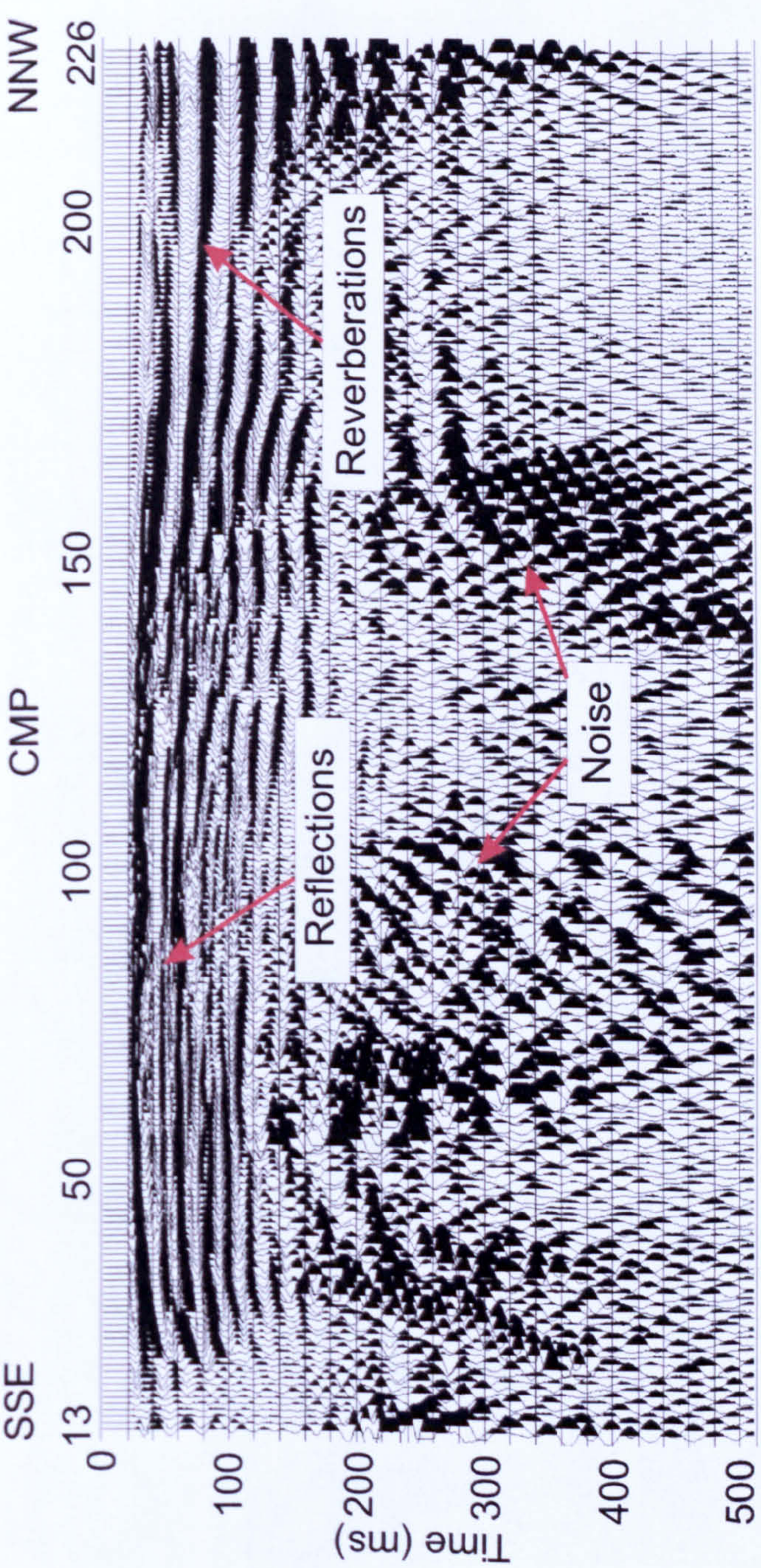


Figure 4.5: Brute stack.
Data are displayed with a scalar multiplier. The distance between each CMP trace is 1 m. CMP numbering is equivalent to the distance from the first geophone station.

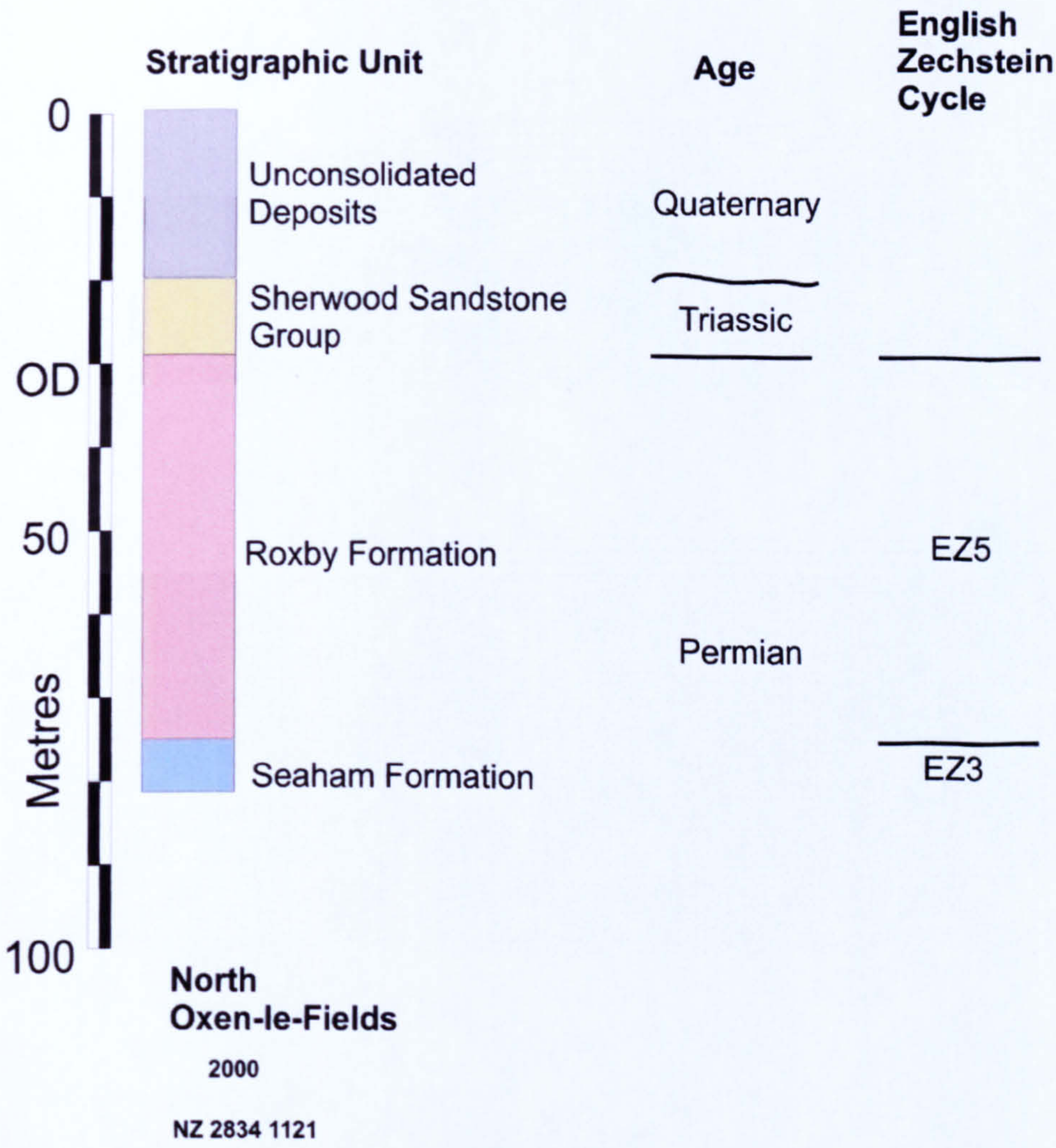


Figure 4.6: North Oxen-le-Fields borehole geological succession.

4.2.2 Shot record polarity and filtering

The first panel of Figure 4.7 is a shot recorded from a saluting cartridge of 5 g of black powder detonated in the first shot hole on profile 04, which was located next to the hedgerow on the southern boundary of Hell Kettles field. The first breaks on the far-traces are very sharp and coincide with an area of water-saturated ground. The signal on the far-channels is modified by very low-amplitude, high-frequency wind noise. Immediately following the refracted first arrivals on the far-channels is a slightly curved high-frequency arrival which may be a reflection event. The near-trace offset was selected as 23 m to ensure that the large-amplitude low-frequency ground roll does not arrive until 160 ms, and the air wave is visible as weak linear high-frequency wave train.

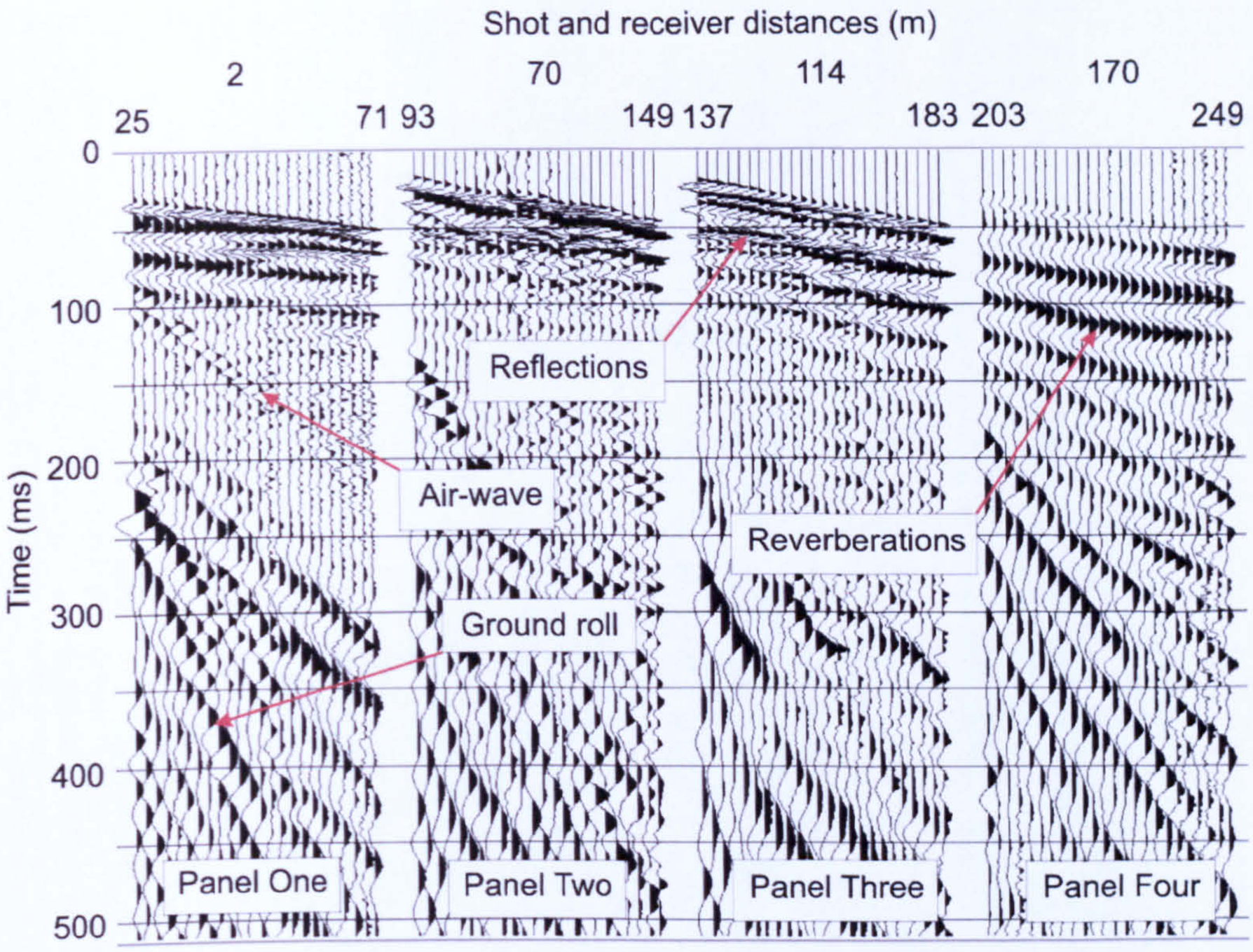


Figure 4.7: A selection of raw shot records.
Data are displayed with a 200 ms AGC sliding window.

The second panel in Figure 4.7 shows a raw shot record from a saluting cartridge fired in water-saturated ground. The sharp first breaks from head waves arising from the water table refractor do not align along a linear trend, implying a variation in ground topography and/or near-surface conditions. The third panel shows a raw shot record from a saluting cartridge detonated in a shot hole drilled into the bed of a streamlet at 114 m from the start of the profile. A reflection event can be traced from 50 ms on the near channel to the middle of the spread where it is becomes masked by a prominent series of low-frequency reverberations. A second reflection event is visible at approximately 65 ms.

Significantly weaker first arrivals were recorded on the fourth raw shot shown in figure 4.7, located in the dry pebbly soil on slightly higher ground near to the northern field boundary. Any reflection energy is completely masked by low-frequency reverberations.

In all of the raw shots the initial first break is positive amplitude motion regardless of shooting conditions. The SEG normal polarity convention is that the onset of a compression from an explosive source is represented by a white loop when displayed graphically. The first

breaks at Hell Kettles are compressional because the first arrivals are refracted head waves from an explosive source, so the data are displayed in SEG reverse polarity. All profiles were processed in SEG reverse polarity.

Bandpass filter trials (Figure 4.8) test the frequency content of the seismic data spatially and temporally. As the low-cut is shifted towards high frequencies, the high amplitudes of the shot-generated ground roll and the low-frequency reverberations are progressively reduced, revealing the reflection signals. There is no useful seismic signal above 330 Hz, only random noise.

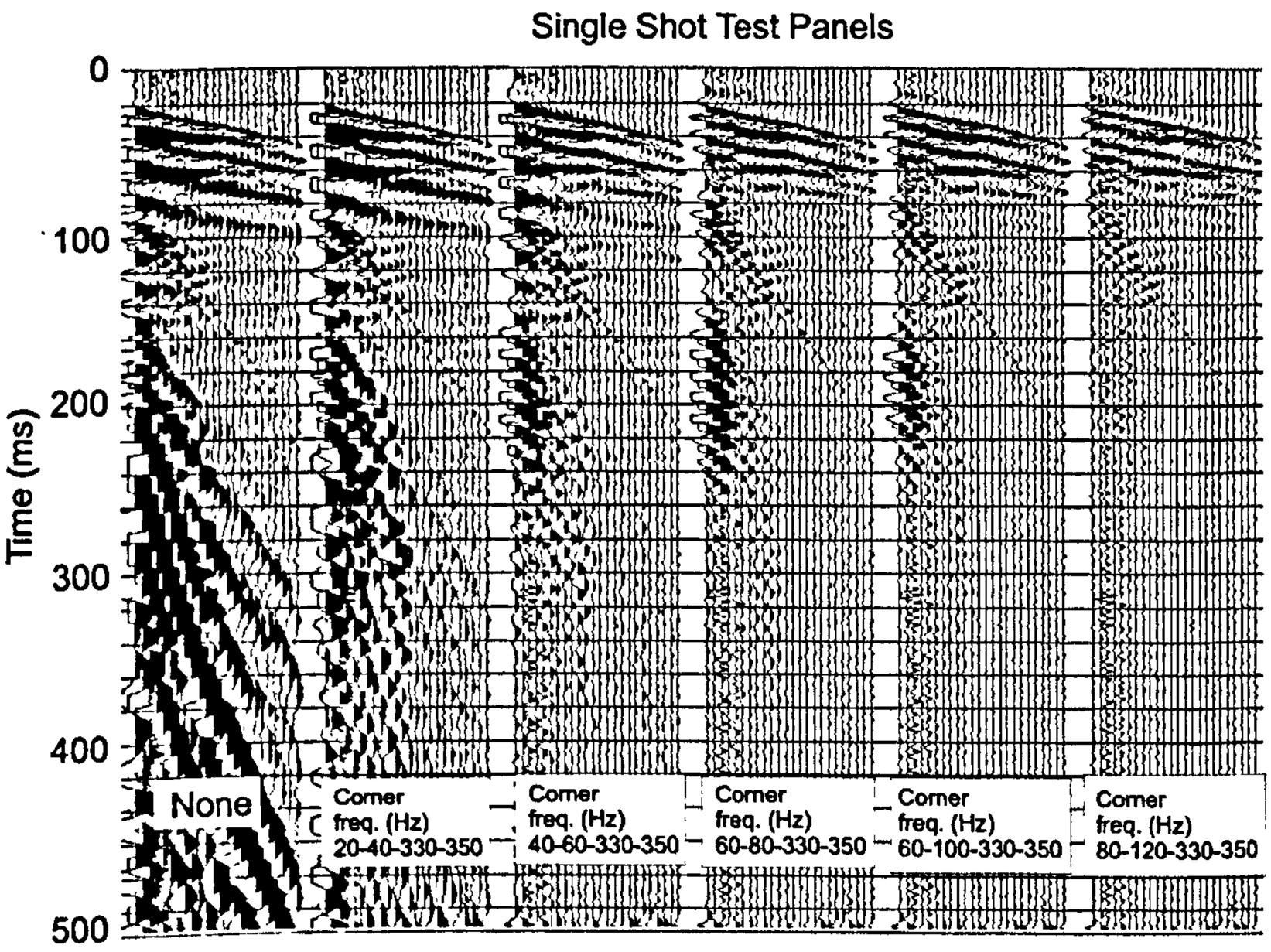


Figure 4.8: Shot ensemble bandpass filter scan.
Data are displayed with a scalar multiplier applied.

The final bandpass filter design (Table 4.1) is time variant. Frequencies less than 60 Hz are excluded over the complete shot gather. At early times, a wide frequency bandwidth of about 1.5 octaves is specified to record the high-frequency reflection energy without attenuation. No useful high-frequency energy is recorded at greater travel times, so the high-cut is linearly tapered after 90 ms, narrowing the frequency bandwidth. Computer-generated artefacts are minimised by linear tapering at each end of the passband.

Stacking the bandpass filtered shots (Figure 4.9) shows that the influence of the ground roll and low-frequency reverberations has been significantly suppressed, and the reflection events have become more prominent.

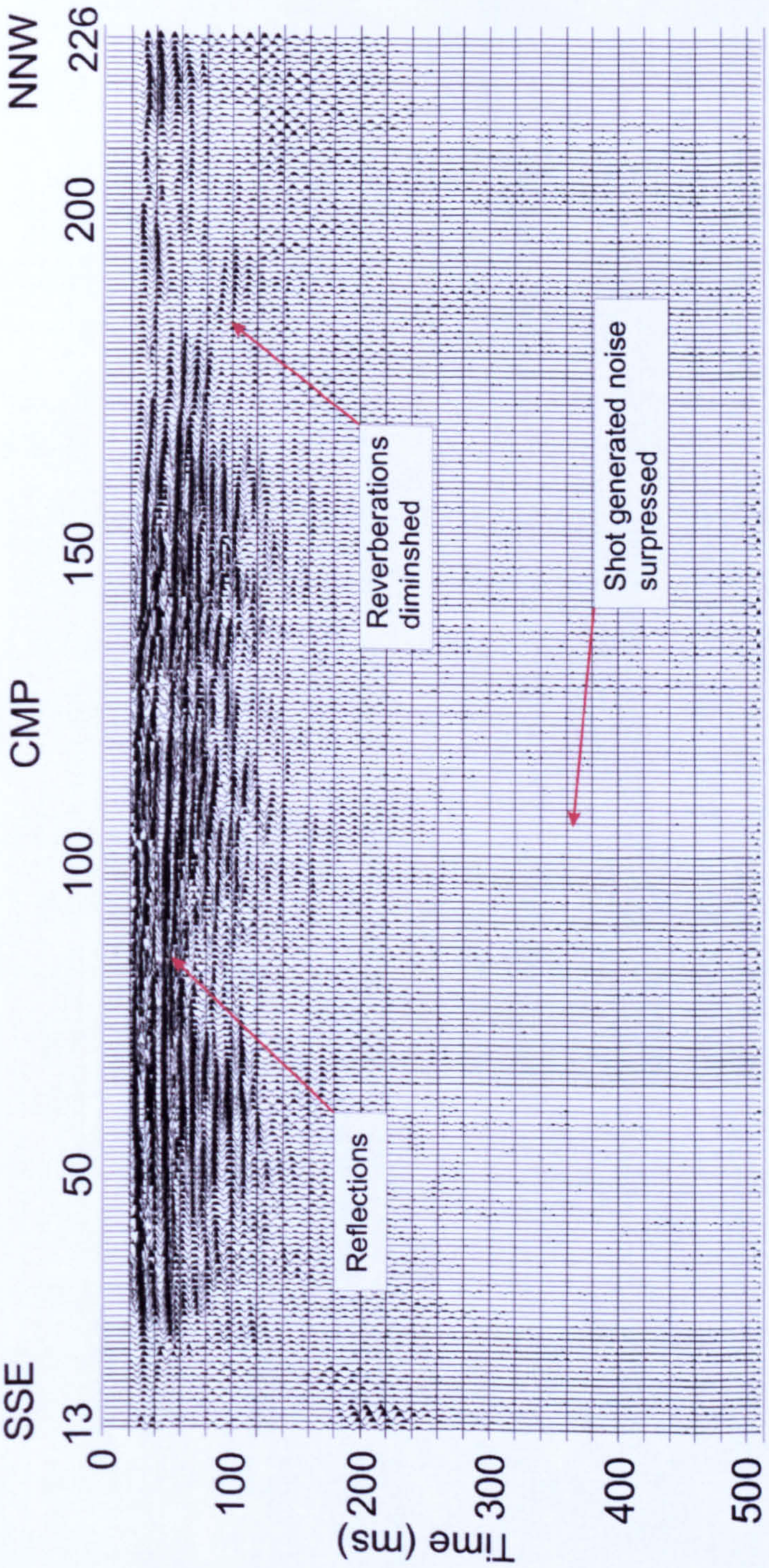


Figure 4.9: Bandpass filtered stack.
Data are displayed with a scalar multiplier.

Shot Record Bandpass Filter Design

Type	Corner Frequencies (Hz)	Time Range (ms)	Channels
Ormsby Zero phase Time variant	60 – 100 – 330 – 350	0 – 90	1 – 24
	Linear Interpolation		
	60 – 100 – 200 – 220	480 – 512	1 – 24

Table 4.1: Shot record bandpass filter design.

4.2.3 Field statics

In the expanded bandpass filtered stack section for profile 04 (Figure 4.10), a reflection event can be traced from 50 ms two-way time (TWT) at CMP 30 through to 40 ms at CMP 177 and down to 50 ms by CMP 170. This curved locus of the reflection horizon could be false, a consequence of the variation in the nature and thickness of the near-surface materials above the water table.

Downward and upward travelling reflected wavefronts will pass through unconsolidated deposits, such as lenses of gravels inter-fingering with layers of sands, perhaps with drapes of clay. It is to be expected that there will be significant differences in travel time for upward travelling wavefronts between neighbouring geophones planted upon the laterally variable fluvial deposits found at Hell Kettles profile 04. Above the water table, the P-wave velocity is slow; the P-wave velocity through dry sands ranges between 200 m s^{-1} and 1000 m s^{-1} (e.g. Sheriff and Geldart, 1995). So an increase in thickness of 1 m of the dry near-surface materials with an interval velocity of 200 m s^{-1} is equivalent to a 5 ms increase in travel time. Below the water table, variations in travel time through water-saturated unconsolidated materials are much less pronounced, since the P-wave velocity in such strata tends to lie in the range 1500 – 2000 m s^{-1}.

Placing shots and receivers on a flat plane below the surficial layer of dry soil would mitigate the undesirable effects of the dry near-surface unconsolidated soils and changes in topography. A much more convenient approach is to project the shot and geophone stations

on to an imaginary plane, a reference datum, by simple time shifts known as static corrections.

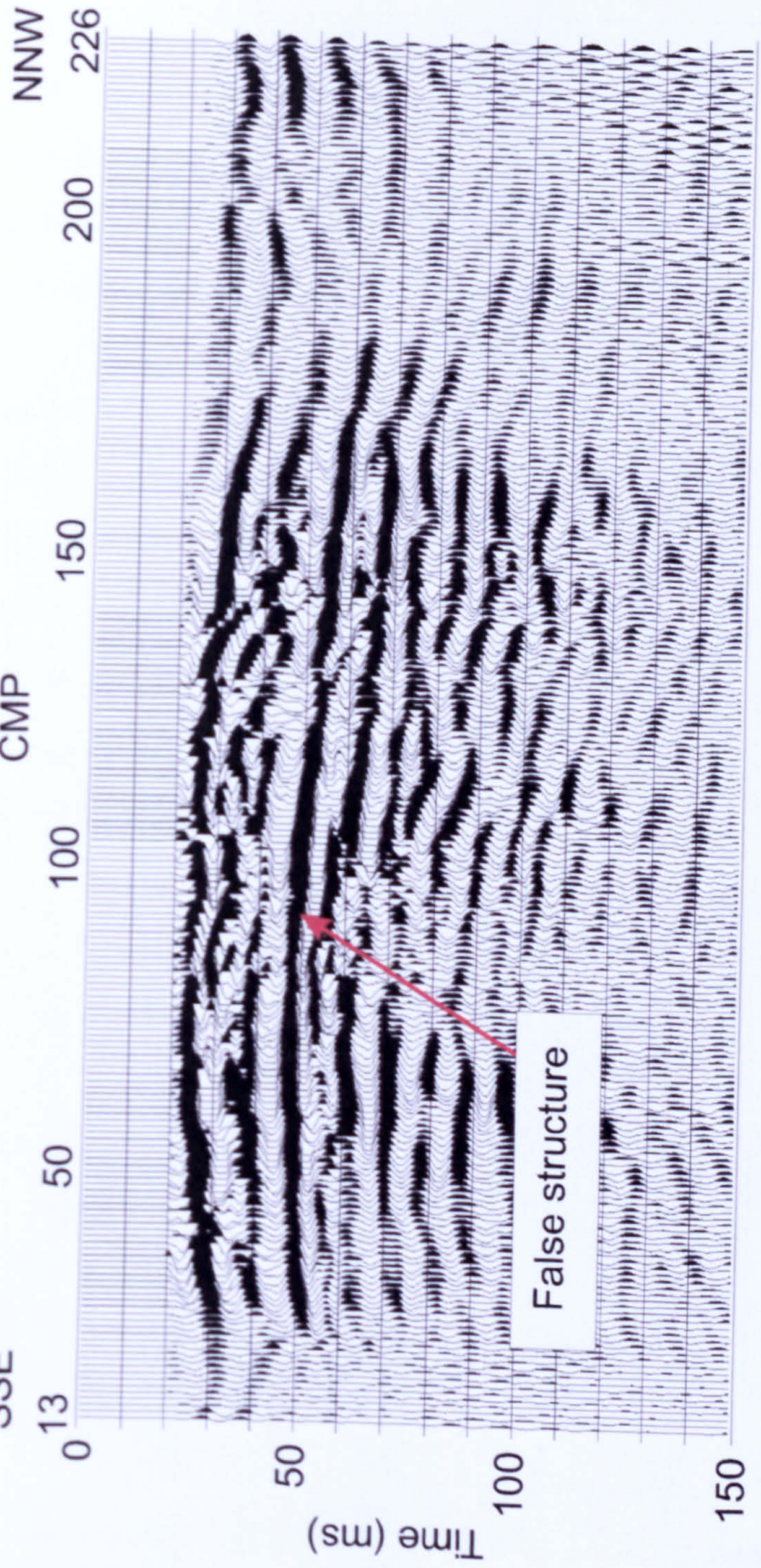


Figure 4.10: Bandpass filtered stack, expanded.
Data are displayed with a scalar multiplier.

For Hell Kettles profile 04, the first breaks on the shot records originate from the large change in physical properties between the dry and water-saturated near-surface deposits at the water table, which lies around 2 m below the ground surface. The time of each first break can be measured accurately from the seismogram, and the distance between each shot point and receiver is also known. Both these pieces of information are sufficient to be able to compute the one-way travel time between for each shot and geophone station and the water table. It is likely that the water table will vary only slowly and smoothly along the complete length of profile 04, so the water table is a good choice to act as a reference datum.

4.2.3.1 Plus-minus method

The plus-minus method of Hagedoorn, (1959) is one of a family of methods used to analyse reversed refraction profiles. Consider two perfectly isotropic media separated by a horizontal interface (Figure 4.11). Let a shot be detonated at point A. Wave energy incident at the critical angle θ_c on the interface will be refracted along it. Some of the energy travelling along the boundary in the lower medium is refracted back up to the surface to be recorded at the geophone planted at position R.

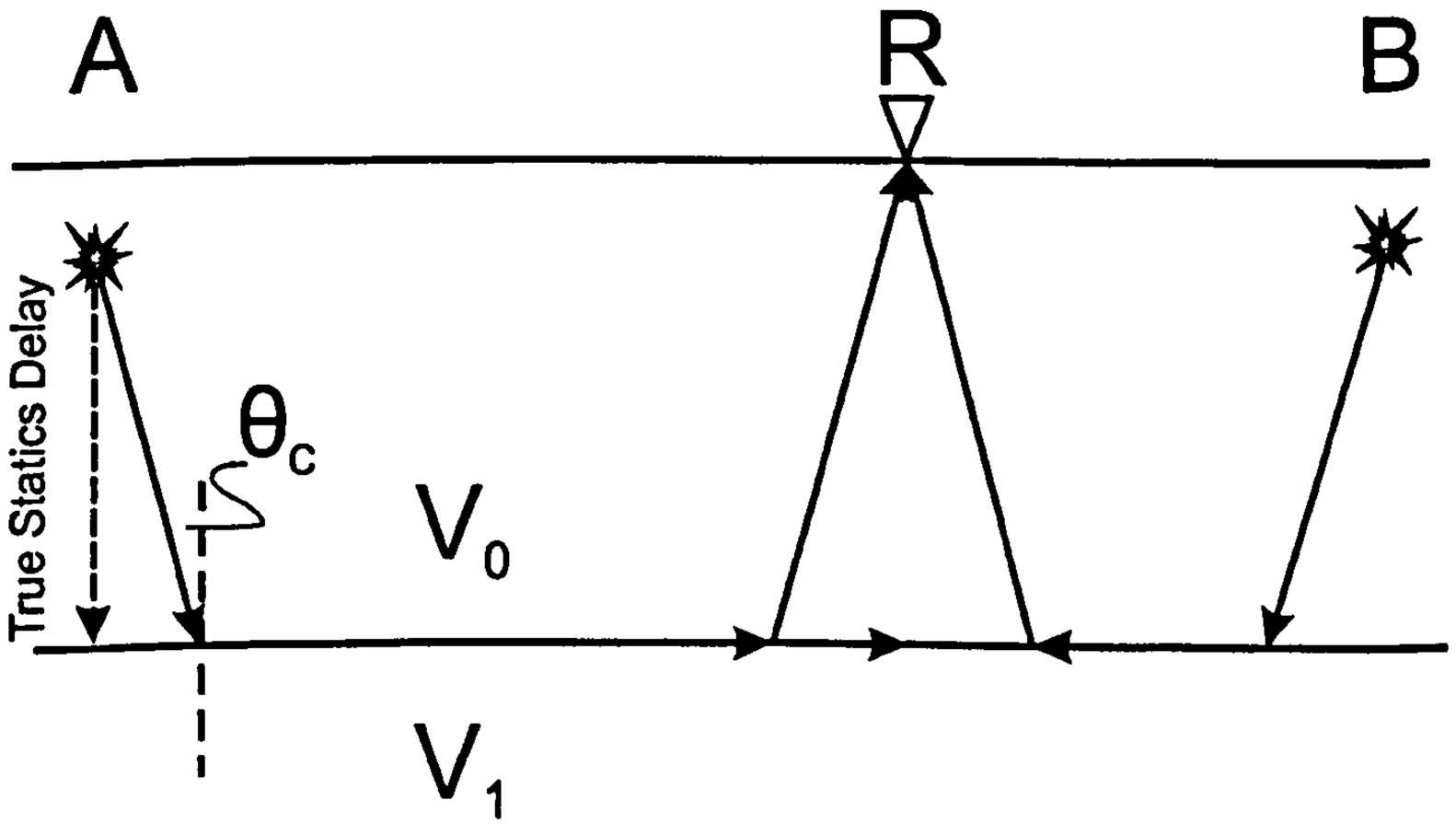


Figure 4.11: Outline of the plus-minus refraction inversion method.
Diagram modified from Cox (1995).

The travel time wave travelling from A to R t_{AR} can be decomposed into three components (e.g. Cox, 1995):

$$t_{AR} = \tau_A + \tau_R + \frac{AR}{V_1} \tag{4.1}$$

The first term on the right hand side is the delay time at shot point A. To a very good approximation, for a high velocity contrast, it equals the one-way travel time for a vertical ray between the shot point and the water table at the seismic velocity V_0 in the near-surface layer. This travel time is the shot static value τ_A for the shot placed at location A. Similarly, τ_R is the receiver static value to be for the geophone at position R. The third component is the travel time for a seismic wave to propagate along the interface in the lower medium at velocity V_1 between points on the interface that are located vertically below the source and receiver stations.

The travel time for the reciprocal shot B into receiver R is:

$$t_{BR} = \tau_B + \tau_R + \frac{BR}{V_1} \tag{4.2}$$

and the travel time between the two shot point positions A and B is:

$$t_{AB} = \tau_A + \tau_B + \frac{AB}{V_1} \tag{4.3}$$

The plus time, T^+, is defined as the sum of the travel times between the shots at positions A and B into the receiver at R, minus the travel time from shot A to shot B. Using equations 4.1, 4.2 and 4.3, it is easy to show that T^+ is twice the delay time at R, i.e., twice the receiver static value to a very good approximation:

$$T^{+} = t_{AR} + t_{BR} - t_{AB} = 2\tau_{R} \qquad (4.4)$$

T^{-} is the minus time, defined by Cox (1995) as the difference between the travel times from the source positions at A and B to the receiver at R, plus the reciprocal time. Algebraic manipulation yields:

$$T^{-} = t_{AR} - t_{BR} + t_{AB} = 2\tau_{A} + 2\frac{AR}{V_{1}} \qquad (4.5)$$

The P-wave velocity in the lower medium V_1 is found from the gradient of the minus graph in which T^{-} is plotted against distance AR. Therefore, if the head wave travel times are known from two reciprocal shots to receiver stations located between them, the static values can be calculated for all those stations. If the interval velocity V_0 of the upper layer is known, the depth to the interface along the profile can also be calculated.

4.2.3.2 Field static calculations

For relatively short profiles with only a few hundred first break data points in the complete dataset, the plus-minus algorithm is suitable for coding into a spreadsheet (Fourie and Odgers, 1995). The first step is to pick all the first breaks for every shot record of the profile. This can be done automatically within the ProMAX software. However, all shots should be examined carefully after running the automatic picking routine. In poor quality shot records, where there is a lot of environmental noise for example, the automatic picks are often misplaced and must be adjusted manually (Figure 4.12). Multi-fold 2D roll-along acquisition results in a large number of overlapping reciprocal shots. Therefore, many statics values need to be computed for each receiver and shot station and averaged to give the final static value for each station. For profile 04, the static values were computed by an alternative approach. Forward and reverse travel time graphs were constructed from a running average of the first break picks of the six nearest traces from each shot record. Using only the refraction time breaks from the near channels ensured that the refraction signals used in the calculations

were all from the uppermost refractor. As a check, the end reciprocal points on the cumulative forward and reverse travel time graphs should have values within few milliseconds.

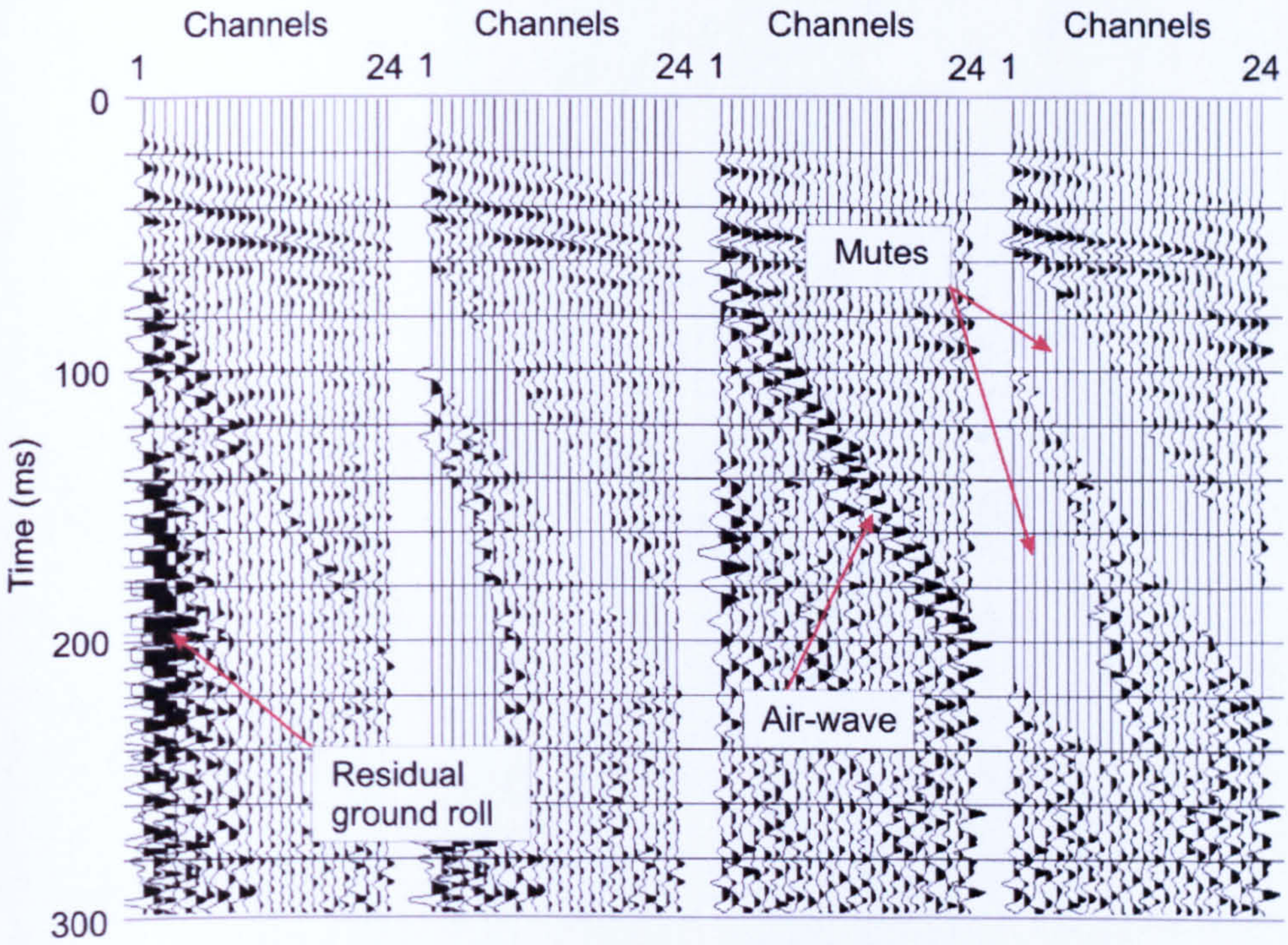
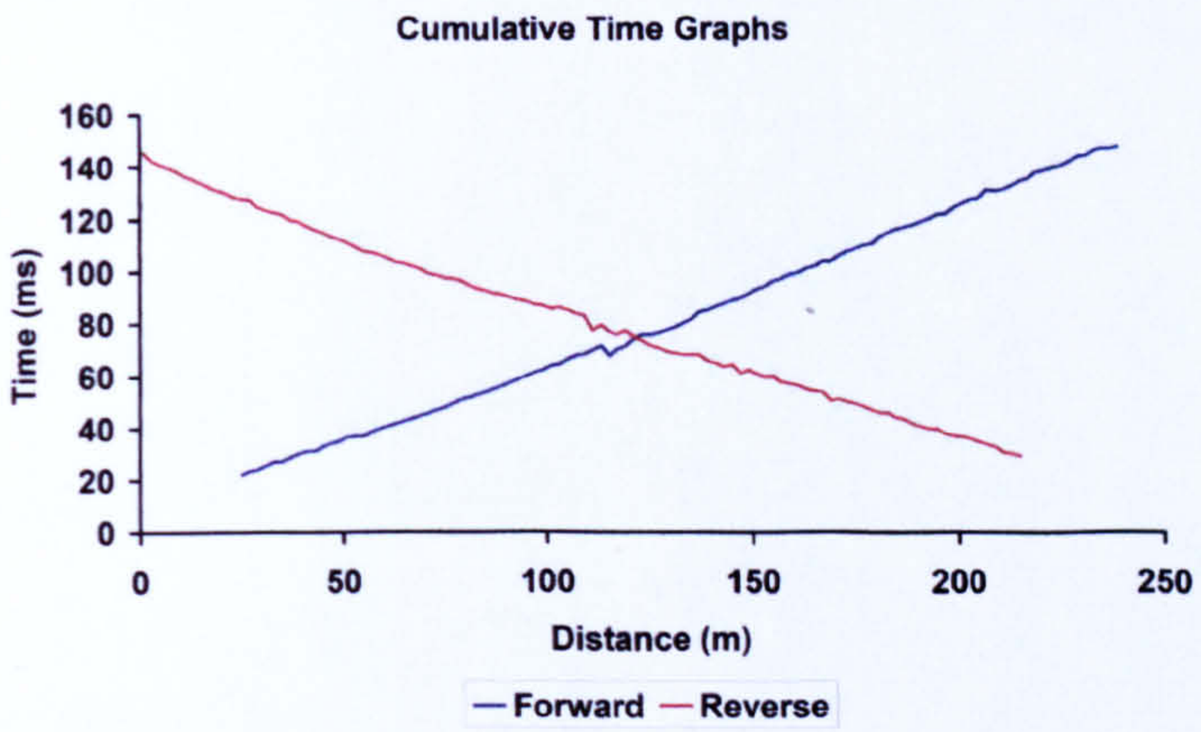
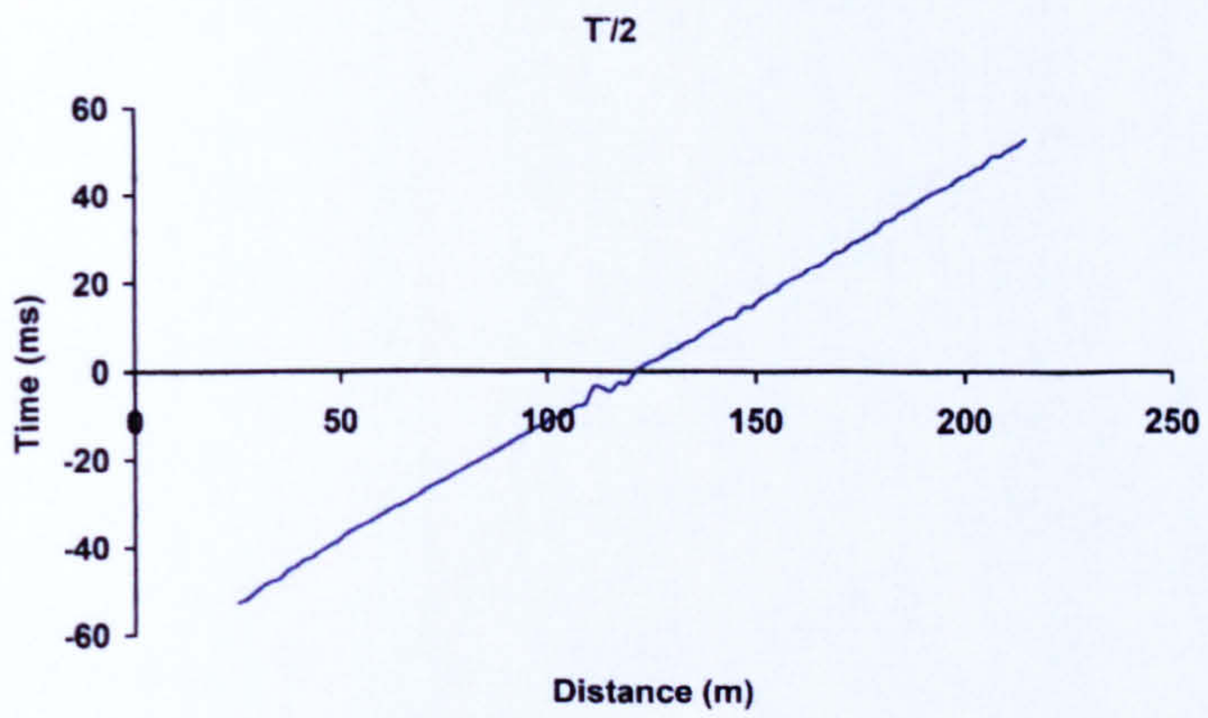


Figure 4.12: First break picking.
Automatic first break picks are displayed in blue. Final, manually adjusted picks are displayed in red. All data are balanced with a 100 ms AGC sliding window before being cropped.

Once the cumulative travel time graphs had been constructed, the graphs for the T^+ and T^- curves were computed (Figure 4.13) for all the receiver stations at points on both the forward and reverse travel time graphs. From these graphs, the refractor velocity V_1 and static values at each receiver station were calculated. For receiver positions outside the region where first arrivals were available on both forward and reverse cumulative travel time graphs, the statics were computed by manipulation of the plus-minus travel time equations. Consider a shot A fired into a receiver R_K of known static delay τ_K and into a receiver R_U of unknown static delay τ_U (Figure 4.14). The travel times to both receivers are known from the cumulative travel time graph and are given by:





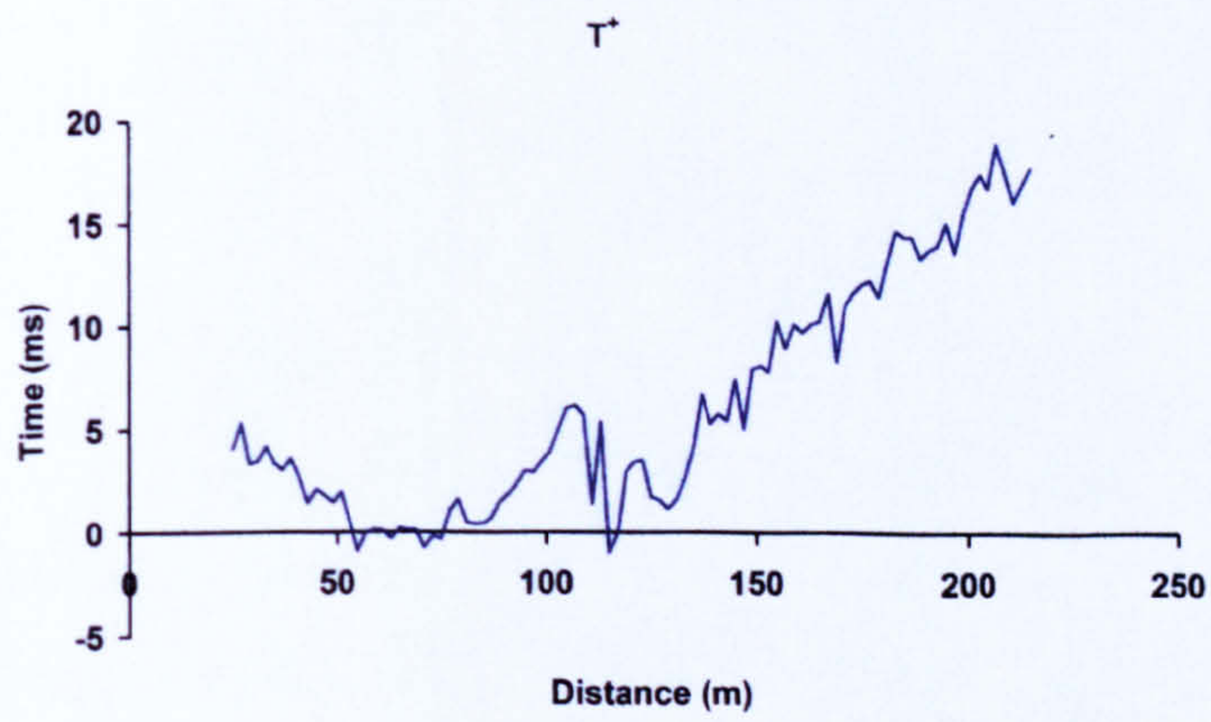


Figure 4.13: Computed plus and minus graphs.

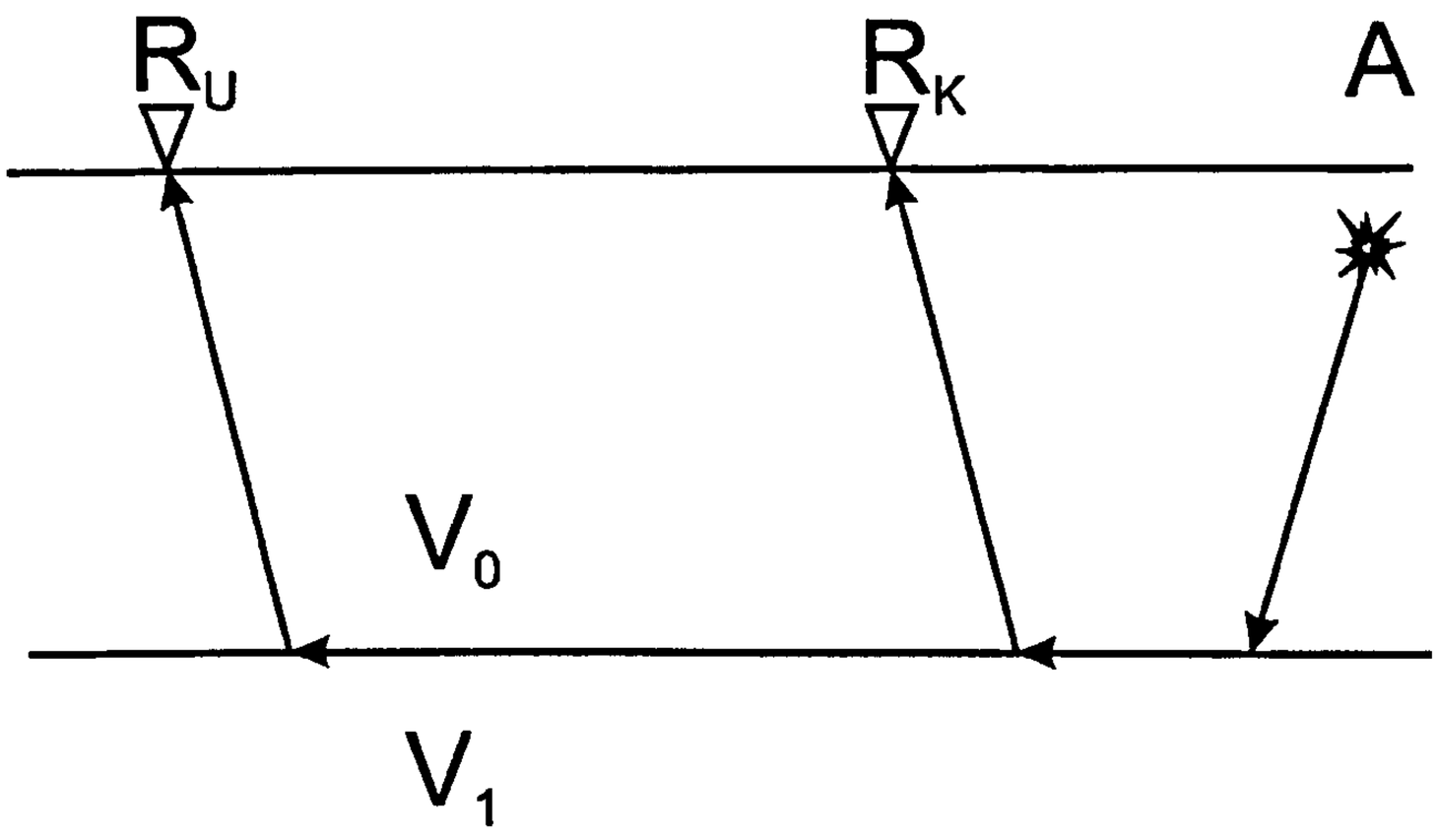


Figure 4.14: Extension of the plus-minus refraction inversion method.

$$t_{AK} = \tau_A + \tau_K + \frac{AK}{V_1} \tag{4.6}$$

$$t_{AU} = \tau_A + \tau_U + \frac{AU}{V_1} \tag{4.7}$$

Elimination of τ_A and rearrangement yields:

$$\tau_U = \tau_K + t_{AU} - t_{AK} + \frac{AK}{V_1} - \frac{AU}{V_1} \tag{4.8}$$

All terms on the right side of equation 4.8 are known, so the unknown static delay τ_U at receiver position R_U can be computed. Once all the statics values for all receiver stations along the length of the profile had been ascertained, all of the shot static values were computed. Each shot gather in profile 04 consists of a maximum of 24 traces, so the value of the shot static was taken as the average of the computed shot delay times for the traces in the shot gather. As a check on the calculations, the computed values of the shot static delay within a high quality shot gather should have a small spread.

After application of the computed field statics the shallow reflection event along profile 04 became flattened (Figure 4.15), exhibiting a gentle dip of about 10 ms across the profile, modified by small undulations on the millisecond scale. False structures caused by the lateral and vertical variations in the near-surface materials have been successfully removed.

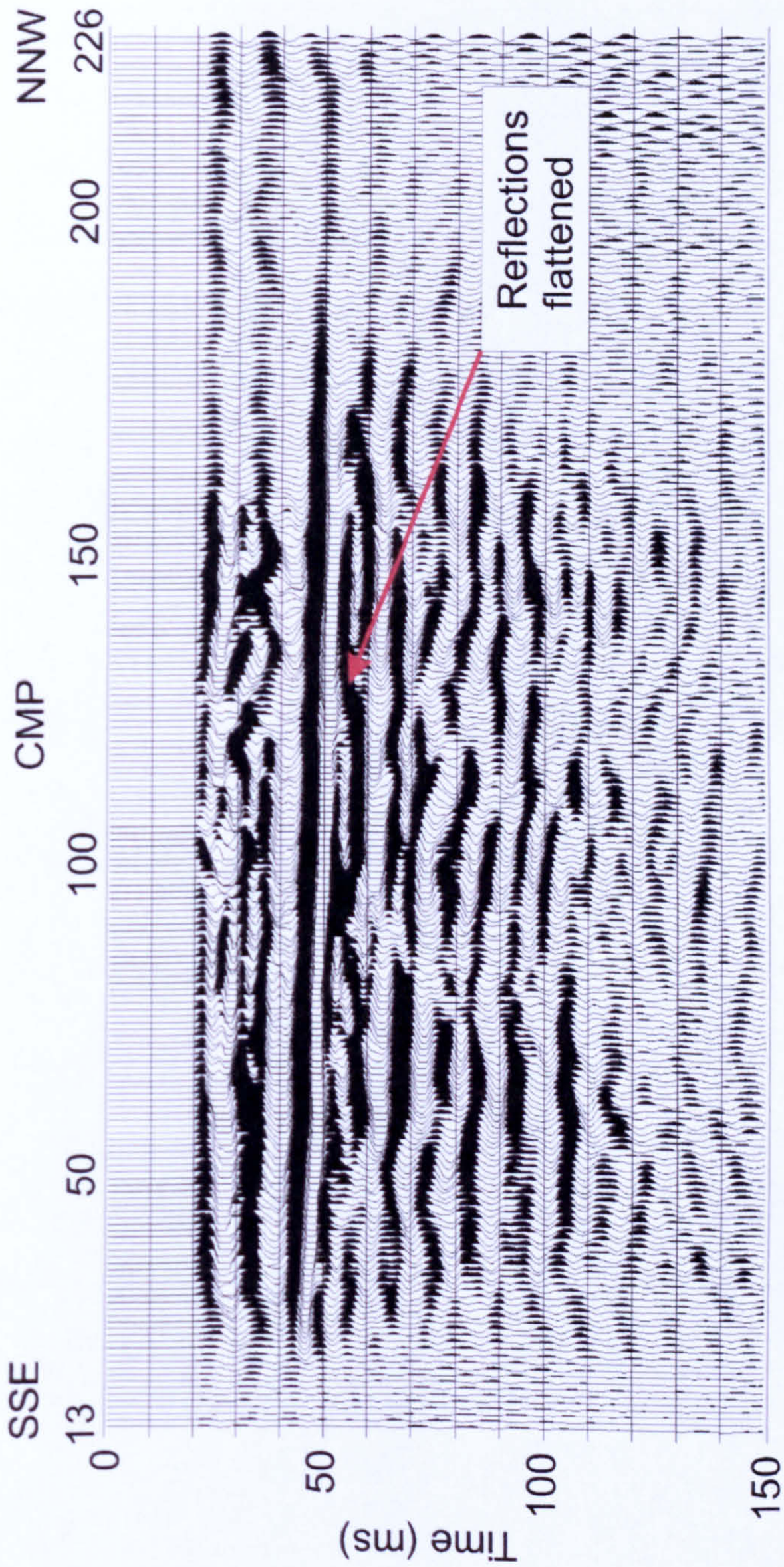


Figure 4.15: Field statics stack.
Data are displayed with a scalar multiplier.

4.2.3.3 Quality control of the field statics solution

The computed receiver statics (Figure 4.16) can be cross-referenced against the field observations of the shooting conditions and the lie of the land. A series of receiver static values close to zero centred around 70 m along profile 04 coincides with the water-saturated zone encountered before the tree line. The position of the streamlet is picked out in the geophone static graph by a sharp downward deflection. Higher receiver static values towards the end of profile are consistent with drier, pebbly conditions and increased elevation of the geophones above the water table.

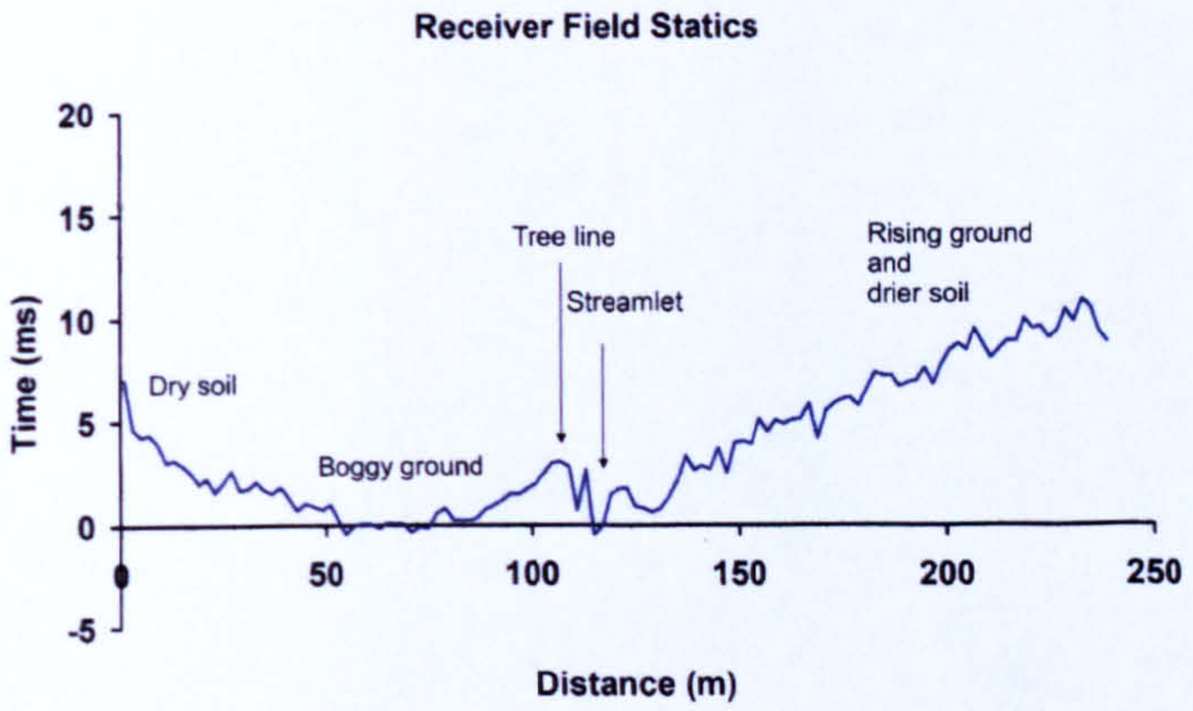
The shape of the shot static distributions for forward and reverse shooting is similar to that of the receiver statics. The large positive and negative spikes in the shot static graphs indicate early and late triggering delays, and can be checked for integrity by visual inspection of the raw shot records. Typically, the scatter in trigger time is small, within the range ±1 ms.

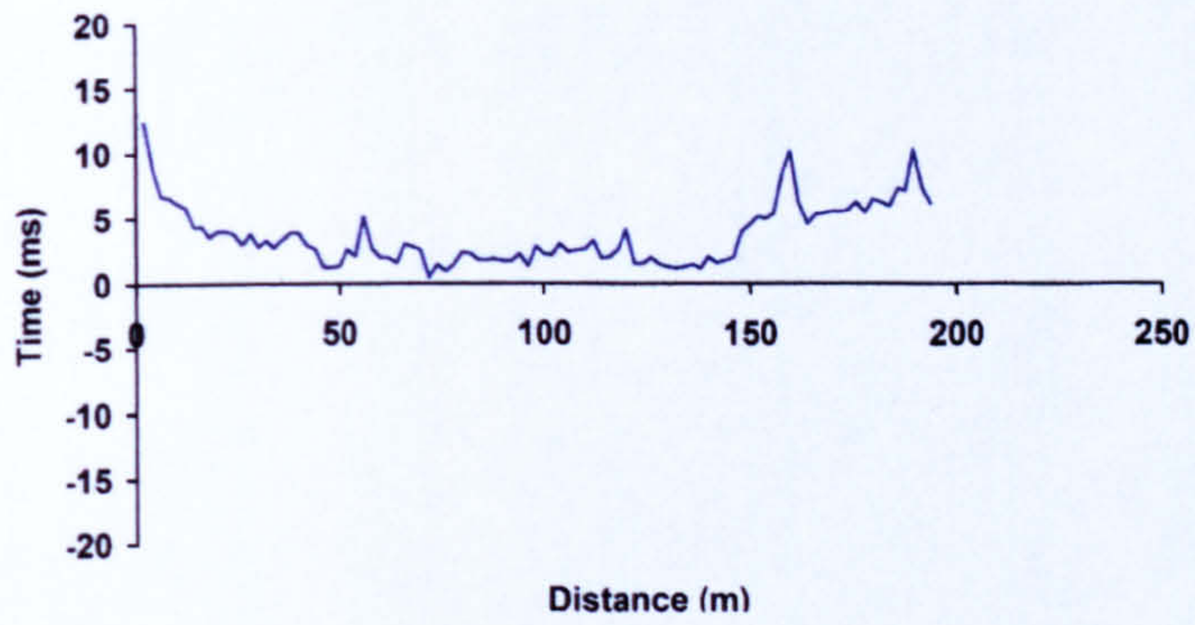
Applying the field statics to the seismic data acquired along profile 04 is equivalent to placing all the shot and receiver stations on the water table. For profile 04 the near-trace offset is 23 m and the calculated refractor velocity is 1826 m s^{-1}. Therefore, if the static calculations are correct, the first breaks on the near-offset channel for all shots should be 13 ms (Figure 4.17). As a further check, after static corrections have been applied the first breaks on each shot record should be aligned with a slope equal to the calculated refractor velocity.

4.2.4 Velocity analysis

For a reflected P-wave, the total travel time between the source and the recording geophone is a function of all the interval velocities in the beds traversed. For small offsets, to a high degree of accuracy, the travel time and P-wave velocity between a source and a receiver of a reflected wave are related by the hyperbolic equation (e.g., Yilmaz, 2001):

$$t^2 = t_0^2 + \frac{x^2}{v_{nmo}^2} \qquad (4.9)$$





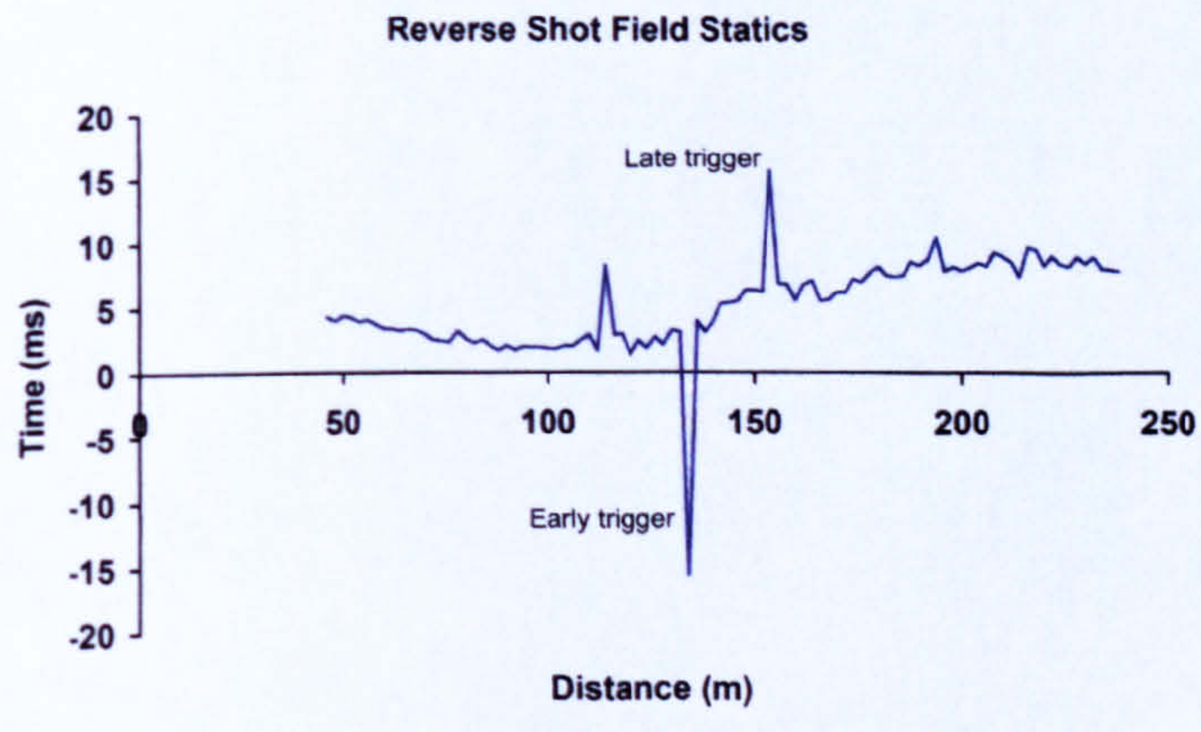


Figure 4.16: Computed field static values for shots and receivers.

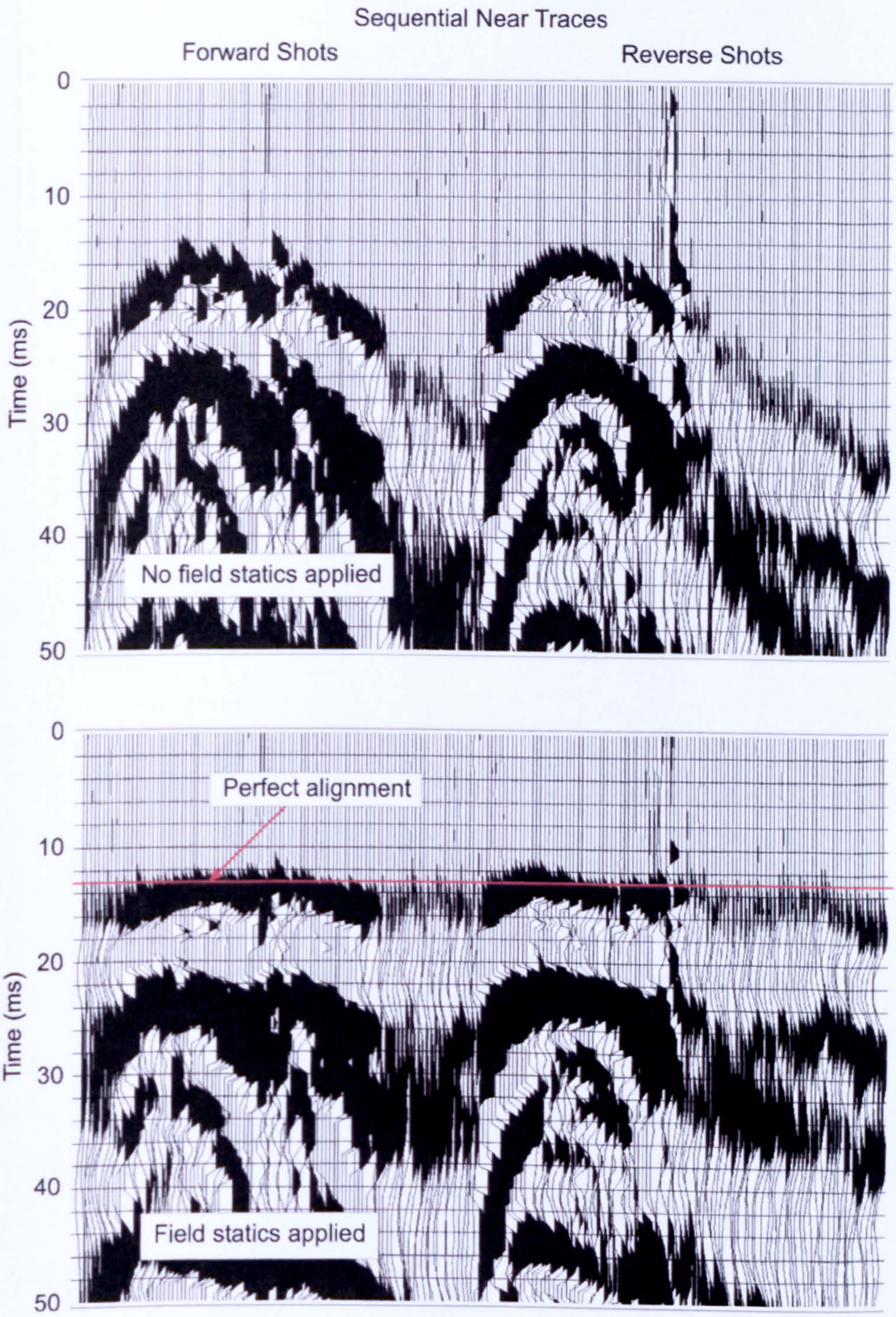


Figure 4.17: Near-trace field statics calculations QC plot.
All data are displayed with a scalar multiplier. The upper panel are the near-trace from all shots without statics applied. The horizontal red line at 13 ms is the perfect field statics correction alignment.

where x is the distance between the source and the receiver, t is the total travel time, t_0 is the travel time at zero offset, and v_{nmo} is the normal moveout (NMO) velocity.

For a homogenous simple isotropic overburden above a horizontal reflector, v_{nmo} is equal to the interval velocity of the overburden. For a stack of N horizontal layers, v_{nmo} can be approximated as the root mean square velocity, v_{rms} (e.g., Yilmaz, 2001):

$$v_{nmo}^2 \approx v_{rms}^2 = \frac{1}{t_0}\sum_{1}^{N} v_i^2 \Delta\tau_i \qquad (4.10)$$

where v_i is the interval velocity in the i^{th} layer and τ_i is the vertical two-way time through the i^{th} layer.

Velocity analysis is performed interactively within the ProMAX software. In Figure 4.18 the second panel is a CMP supergather of five consecutive CMPs centred at CMP 66 on profile 04. Where the local geology is changing slowly, the signal to noise ratio for velocity analysis is improved by the summation of adjacent CMP gathers without compromising the data resolution. The seismic signal is usually balanced prior to velocity analysis by running a 100 ms automatic gain control (AGC) sliding window over the data. If the picked stacking velocity is slower than optimum, then any primary reflection events within the CMP gather will be overcorrected and slightly curved upwards when the NMO is applied. If the picked stacking velocity is faster than optimum, the primary reflection events will slightly curved downwards, or be undercorrected.

The first panel in Figure 4.18 is a semblance plot. Semblance is a measure of signal coherency, defined as the normalized output to input energy ratio (e.g., Yilmaz, 2001). High semblance values are computed when the hyperbolic curve for a particular velocity and time matches closely a signal within the gather under scrutiny. Usually, large values for semblance are calculated for primary reflection events; however, multiples and coherent seismic noise may give rise to large semblance values at incorrect stacking velocities.

Each strip in the third panel of Figure 4.18 is the response of the CMP supergather to the application of a single velocity function. In this display, the chosen velocity function is a

single velocity applied to the complete gather, a constant velocity stack (CVS) display. The velocities applied increase from left to right, where the velocity is close to the optimum value, the primary reflection event stacks with maximum amplitude.

The event with a high-amplitude black loop at 45 ms on the near-trace (Figure 4.18) is interpreted as the reflection from a distinct geological interface and therefore picked as a primary reflection event. A shallow weaker event with non-linear moveout is also picked at 32 ms on the near-trace. The linear refraction event should not be confused with primary reflections. The last reflection primary event is interpreted at 57 ms. At later times there some are large semblance values, but these are generated by remnant low-frequency reverberation noise and the velocity trend is picked to reflect the general trend of increasing velocity with depth within the Earth.

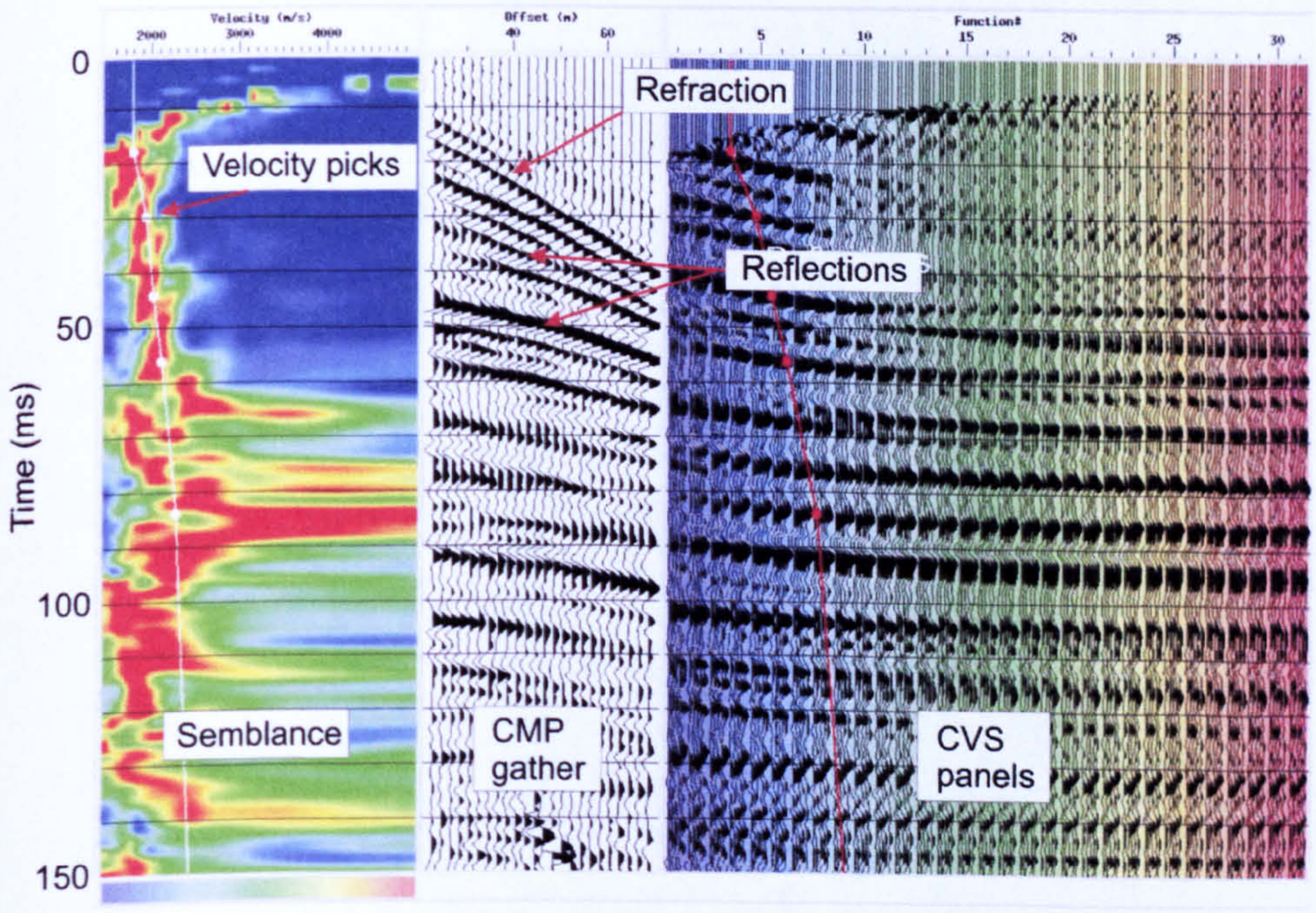


Figure 4.18: ProMAX interactive velocity analysis.

Velocity analysis is performed at regular intervals along the length of the profile, with the main picks following the lateral trend of any primary reflection arrivals with the largest amplitudes. The final velocity field forms the stacking velocity function that is used to calculate the NMO corrections and yields the optimum stacked seismic image of the sub-surface geology.

For Hell Kettles profile 04, the stacking velocity field was refined at several points during the processing sequence, in particular after the application of field statics, deconvolution, and surface-consistent residual statics. A velocity field picked at 30 m intervals has only altered the continuity of the gently dipping reflection horizon minimally (Figure 4.19) compared to the stack section (Figure 4.15) of CMP gathers corrected by a single point stacking velocity field based on the geology of the nearby North Oxen-le-Fields borehole.

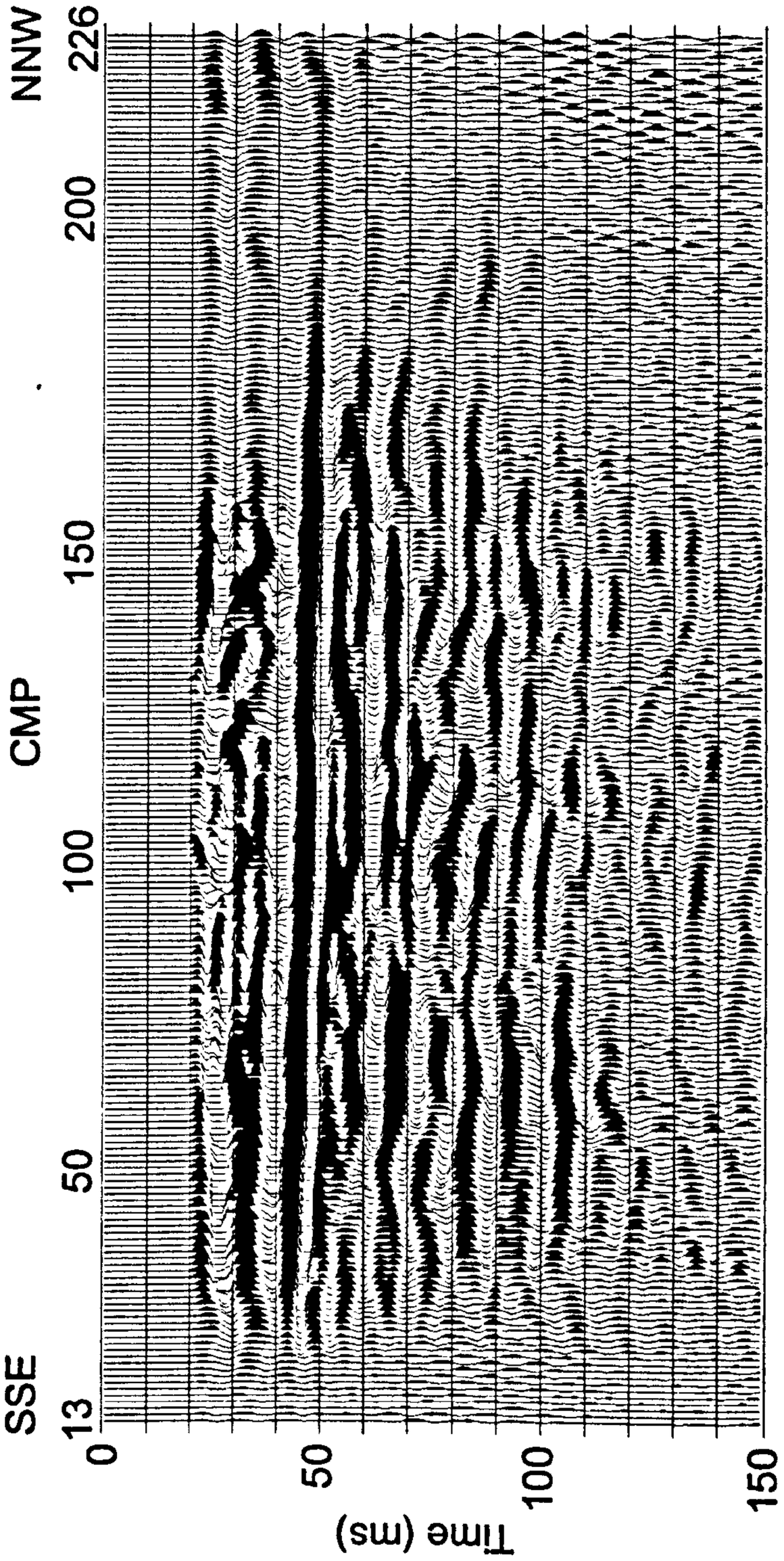


Figure 4.19: Field statics stack with multiple point stacking velocity field.
Data are displayed with a scalar multiplier.

4.2.5 Gain recovery

Suppose a perfectly spherical explosive charge is detonated within a perfectly elastic homogenous isotropic medium and assume that all the energy generated is transferred instantaneously to the surrounding medium. A sharp wavefront will propagate outwards in all directions through the medium at the same P-wave velocity. Assuming no loss of energy due to anelastic processes as the wave propagates, the amplitude of the signal will decrease inversely as the distance from the source.

In the real world, the decrease in the amplitude of the signal is more pronounced. P-wave velocity usually increases with depth, causing greater divergence of downward propagating energy. As the P-wave propagates through the rock mass, the rock dilates and contracts, and frictional and viscosity effects cause mechanical energy to be converted into heat. The quality factor Q is inversely proportional to the fraction of energy lost per cycle (e.g., Sheriff and Geldart, 1995). In many shallow seismic reflection investigations the path of the recorded signal includes a large proportion of unconsolidated deposits which have low Q values. Some P-wave energy may also be lost at geological boundaries, by reflection and mode conversions.

Signal loss can be compensated by a variety of gain functions in ProMAX including user-defined gain functions. A suite of different gain functions can be easily compared on individual shot records, analogous to the testing of different bandpass filters. In the case of profile 04, where the nature of the near-surface conditions along the profile length change considerably, a gain function proportional to $1/vt^2$ balances the signal well, where v is the picked stacking velocity. The selection of the best gain function is made by examining shot records in tandem with the seismic sections stacked with different gain functions.

The near-trace display in Figure 4.20, upper panel, shows that the signal strength recorded from shots fired in holes drilled between 20 m and 140 m along profile 04 is much greater than outside this region. Poor signal amplitudes correspond on the ground to shot points in drier soil conditions. As a consequence, the signal strength of the gently dipping reflection event at around 40 ms decreases at beginning and end of the stacked section of profile 04 (Figure 4.19).

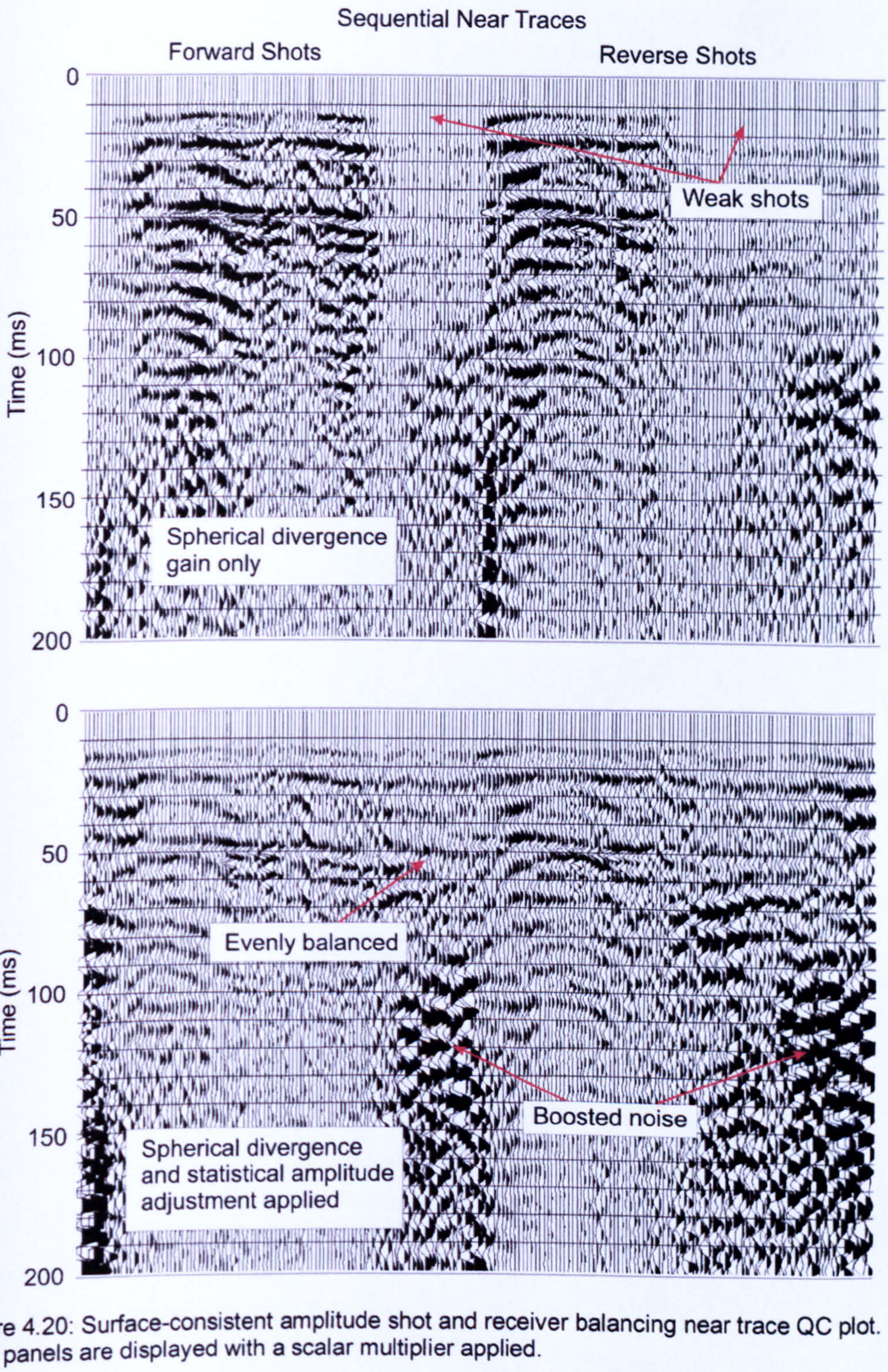


Figure 4.20: Surface-consistent amplitude shot and receiver balancing near trace QC plot. Both panels are displayed with a scalar multiplier applied.

The seismic signal along the length of the stacked section can be better balanced by normalising the relative amplitude strength of all shot records, hence improving the interpretability of any reflection events with the stacked section. This can be achieved by applying a simple AGC window over each shot record. A more sophisticated statistical approach was employed to balance amplitudes for both shots and receivers for Hell Kettles profile 04.

The surface-consistent model was originally defined to compute time shifts for residual static corrections (Taner et al., 1974), but can be extended to amplitude adjustment (Taner and Koehler, 1981), where attenuation is assumed to be associated at each geophone and shot location, m and n. Also defined in the surface-consistent model are structural and offset components, k and l, the midpoint and distance between the receiver and source stations. The seismic signal for each unique source-receiver pair in the frequency domain separates into amplitude and phase components. The amplitude component is represented by (Taner and Koehler, 1981):

$$f_{nm} = s_n + r_m + c_k + d_l \tag{4.10}$$

where f_{nm} is the natural logarithm of rms amplitude of trace with its source and receiver at surface positions n and m, respectively, and s_n, r_n, c_k and d_l are source, receiver, sub-surface and offset components.

There is one equation for each seismic trace within the seismic dataset and each source-receiver pair can be cross-correlated against another. In a typical 2D profile there will be a large amount of redundancy and the adjustment of the amplitude of the source, receiver, structural and offset components at each station can be solved by minimizing the sum of the squares of the errors by a least squares iterative algorithm.

For Hell Kettles profile 04, the cross-correlation signal for each trace was limited by a user-defined window around the coherent reflection energy, excluding the refraction arrival and the deeper noise-laden sections of the shot ensemble from the statistical calculations. Although all four different components of the surface-consistent model are calculated, only

the source and receiver values were applied to the seismic data. The near-trace display shot strength following surface-consistent amplitude adjustment is much better balanced (Figure 4.20, lower panel). Applying a gain function and surface-consistent amplitude balancing in the shot and receiver domains to the seismic data of profile 04 has pulled through the dipping reflection event at the beginning and end of the profile (Figure 4.21), but with an increase in noise amplitude in the lower half of the stacked section.

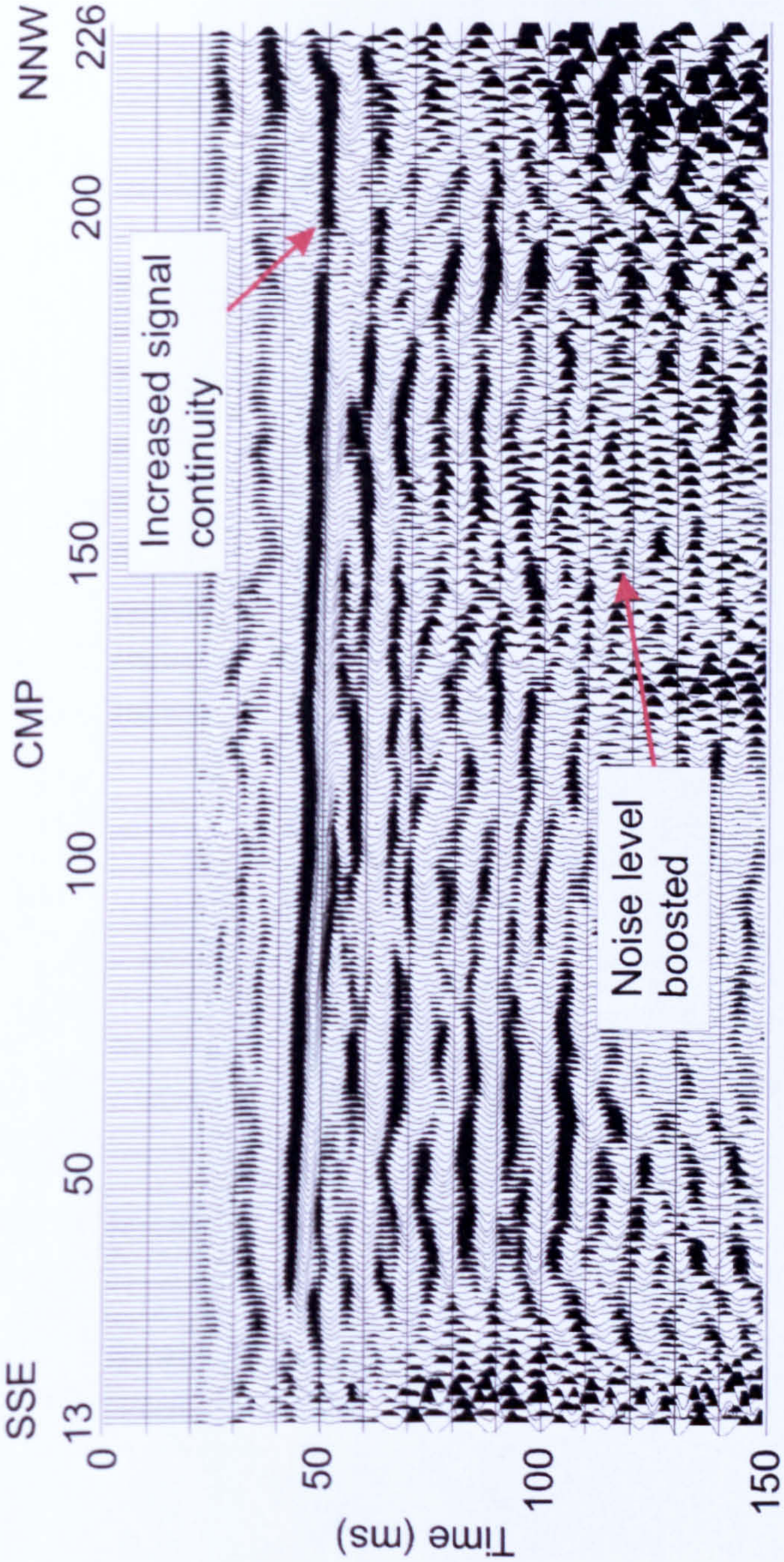


Figure 4.21: Shot and receiver amplitude balanced stack.
Data are displayed with a scalar multiplier.

4.2.6 Noise muting on shot records

The boosted noise content observed in the gain balanced stacked section (Figure 4.21) falls within two categories: the steeply dipping linear cross-hatched noise which occurs in the middle and at the edges of the section; and a more disorganised, but higher amplitude noise that is prominent at the edges of the section. The individual shot records with excessive background seismic noise can be correlated to the drier, more gravelly soil conditions along profile 04. A more aggressive style of processing must be used to suppress noise artefacts and to improve the signal to noise ratio in near-surface seismic datasets than in large scale hydrocarbon exploration projects (Baker et al., 1998).

The first type of noise is the stacked representation of the audible sound travelling through the air (Figure 4.22). The air-wave interferes with the reflection events on only a few near traces, so the air-wave was removed efficiently from the shot record by a simple surgical mute. The disorganised noise is the remains of aliased higher frequency modes of the dispersive ground roll which were not eliminated by the bandpass filtering applied to the shot records. It, too, was removed by judicious surgical muting. Significant improvement in the continuity of signal was achieved (Figure 4.23) when care was taken not to remove too much data from the shot record in the mute design.

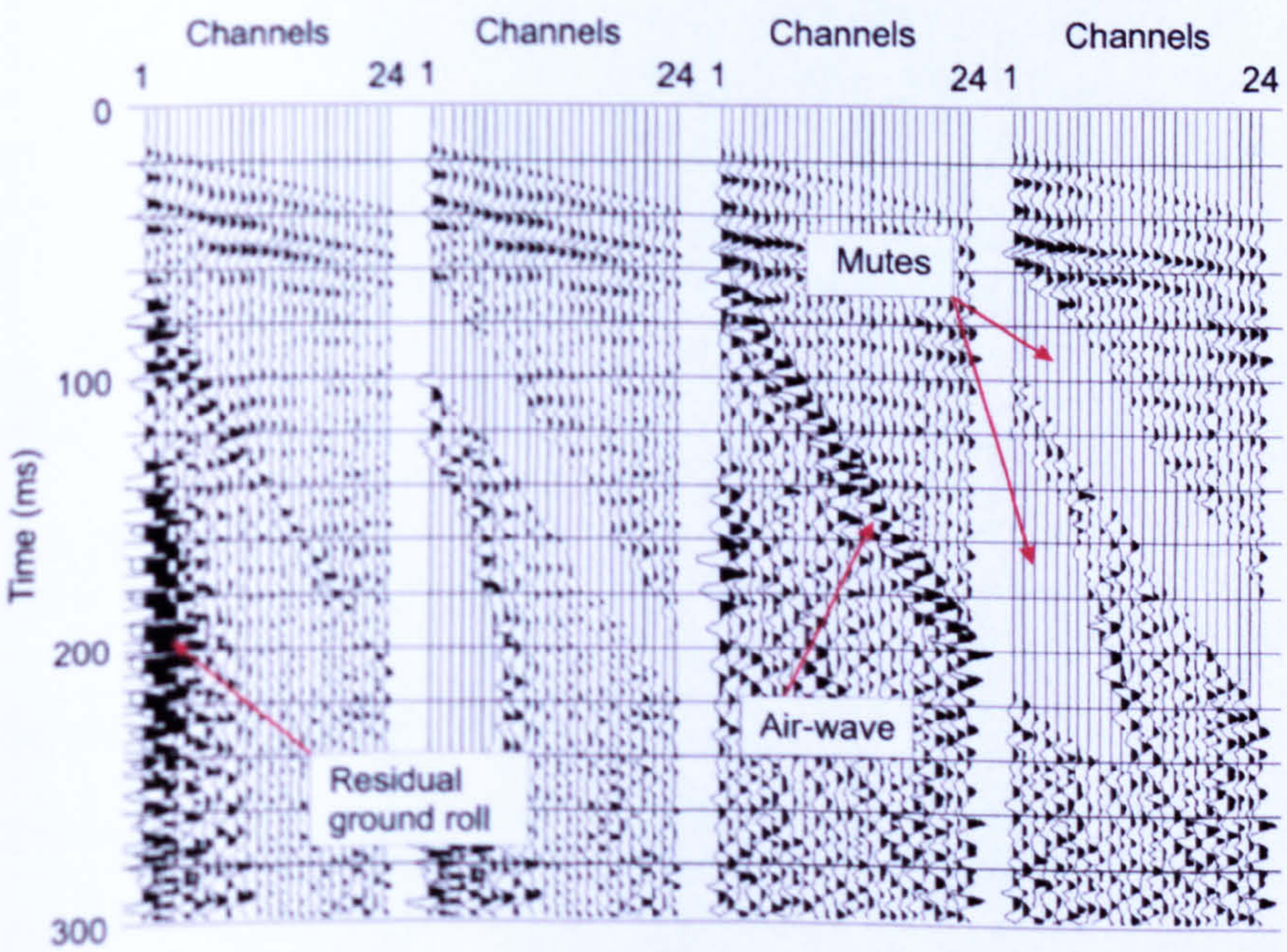


Figure 4.22: Surgical noise muting on shot ensembles.
All four panels are displayed with a scalar multiplier applied.

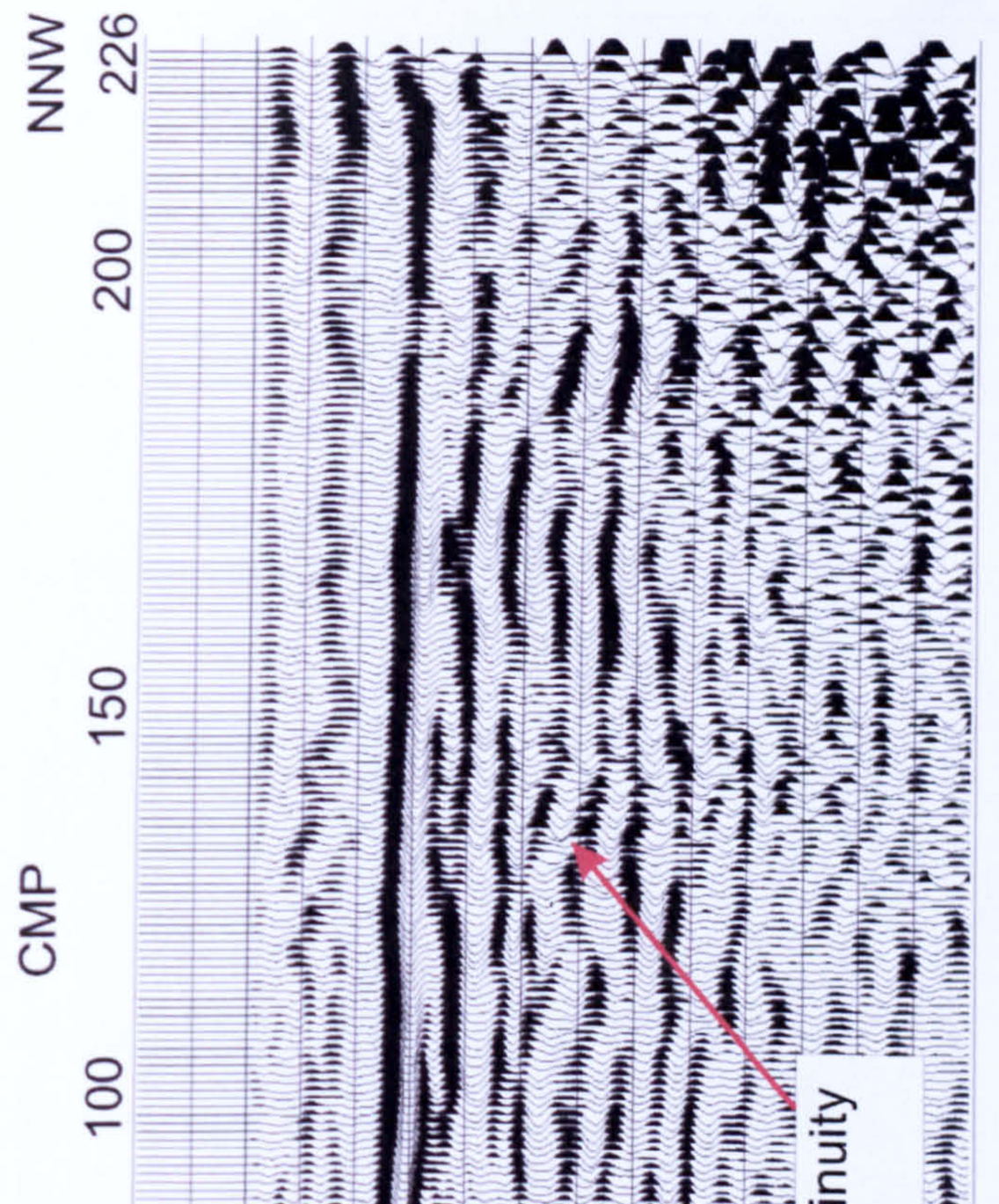


Figure 4.23: Noise mute stack.
Data are displayed with a scalar multiplier.

4.2.7 Improving the temporal resolution

A perfect shot record seismic signal from an explosive source of very short duration would be zero except for sharp pulses corresponding to reflections from the sub-surface geological boundaries. However, the recorded seismic signal not only contains primary reflections, but

also other signals such as multiples, diffractions, direct waves, head waves, surface waves and near-surface guided waves. The shape of the wavelet is also altered by absorption processes and loss of energy by wave conversions. The recorded waveform can be expressed as a convolution (e.g., Sheriff and Geldart, 1995):

$$g = r * w \tag{4.11}$$

where g is the recorded seismogram, r is the primary reflectivity, and w is the effective wavelet.

The aim of deconvolution is to extract the primary reflectivity from the recorded seismic data, but in equation 4.11 only g is known. So to improve the interpretability of a seismic section, the unknown effective wavelet within the seismic data is replaced by a more satisfactory wavelet using the process of predictive deconvolution (e.g. Sheriff and Geldart, 1995). In applying this process, it is assumed that g is a stationary stochastic signal, that the Earth's primary reflection coefficient sequence is a white noise signal, and that the effective wavelet is minimum phase. In practice, these assumptions are commonly not met in shallow seismic reflection profiling. When only a few strong reflectors may be present, the primary reflectivity will not be a white noise signal; and even if the effective wavelet in the raw data is minimum-phase, application of the gain ramp to make g appear more stationary is likely to make the wavelet both non-minimum-phase and variable in shape along the seismogram (Ziolkowski, 1984). For Hell Kettles profile 04, below the strong reflection event at 40 ms in Figure 4.23 are a series of events that are sub-parallel and of similar frequency content to the gently dipping reflection horizon, although the deeper events are less continuous in appearance.

Examination of a shot record after application of field statics (Figure 4.24, first panel) shows the strong reflection event at 50 ms on the near-trace curving down to 60 ms at the far offset. The associated autocorrelation function shows the reverberative nature of the seismic signal following the main reflection horizon. However, mixed in with the reverberations may be primary reflection events or multiples of primary reflections. Frequency analysis of the shot record reveals that the seismic signal has a flat amplitude spectrum between 80 Hz and 150

Hz, falling away by 25 dB at 300 Hz. The limited bandwidth nature of the seismic data results in the "ringy" dataset.

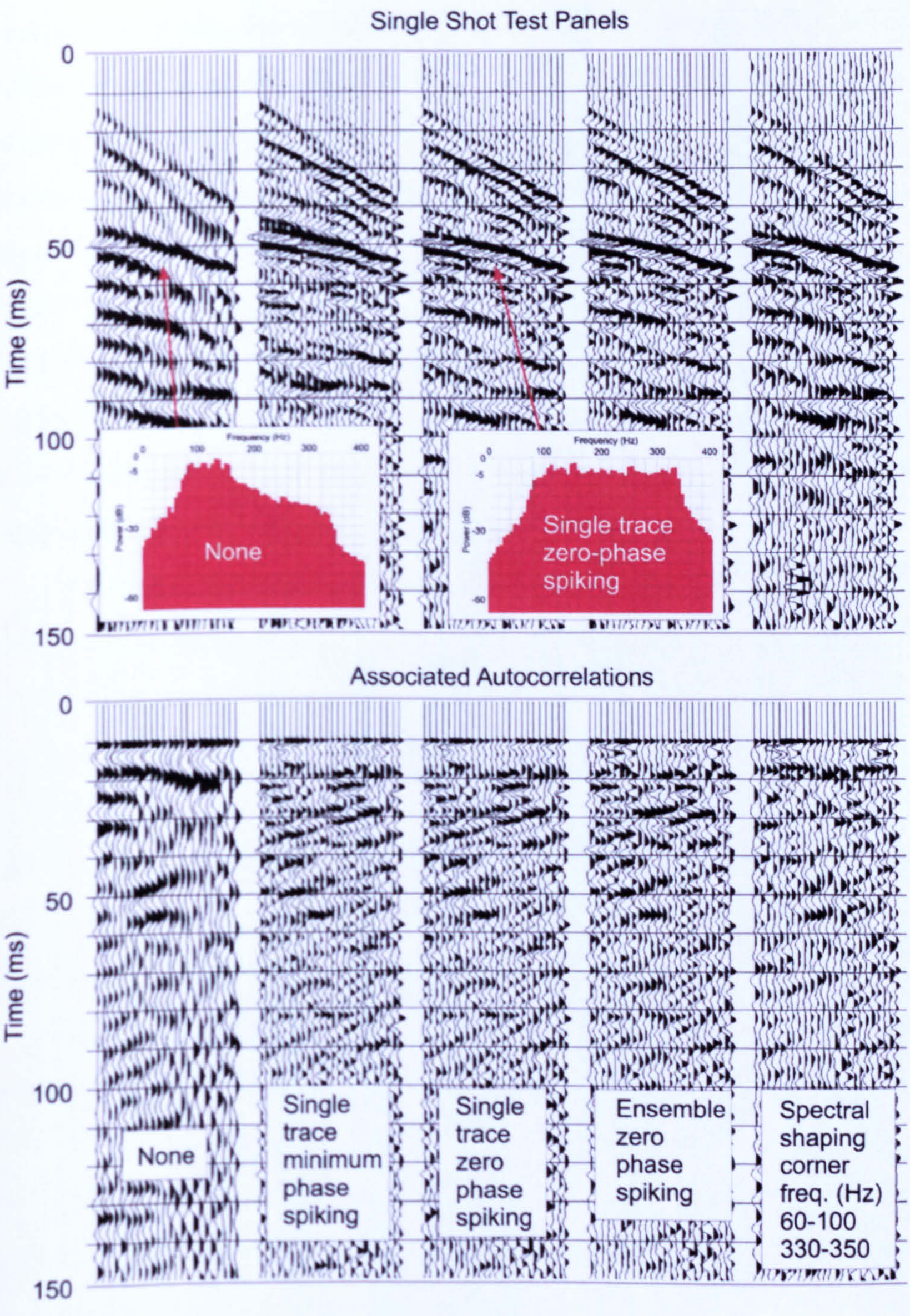


Figure 4.24: Deconvolution type test panels on a single shot record.
The test panels including the associated autocorrelations are scaled with a 200 ms AGC sliding before being cropped. Spectral analysis is performed on a window focused on the reflection energy only.

Figure 4.24 also shows the effect on a shot record of filters computed using slightly different variations of the input signal to the Wiener-Levinson algorithm and spectral shaping. In the spectral shaping trial all the amplitudes between 100 Hz and 330 Hz are forced to the same level. Outside this range the amplitudes are ramped down to zero at 60 Hz and 350 Hz. For all the Wiener-Levinson comparisons displayed in Figure 4.24 the operator length, 10 ms, white noise, 0.1 %, and correlation window are the same. The correlation window covers the area in the shot record that is dominated by primary reflection energy, excluding the refracted arrival and random noise that may alter the inverse filter operator and potentially degrade the final result. A rule of thumb to ensure spurious artefacts are not generated is that the data window over which the autocorrelation function is calculated should be a minimum of 10 times the operator length. Spurious low and high-frequency noise boosted in amplitude by application of the Wiener-Levinson deconvolution algorithm were suppressed by applying a bandpass filter with corner frequencies of 60 Hz, 100 Hz, 330 Hz and 350 Hz.

All of the outputs from the different trial deconvolution variations are broadly similar in character and frequency content, with the strong reflection event considerably sharper compared to the non-adjusted first panel. The resolving power of spectral shaping is slightly poorer than the other trials, whilst the single trace minimum-phase option produces splitting of the upper black leg of the strong reflection event on the near traces. No significant difference is observed between the single trace and ensemble zero phase spiking options, but examining the result of the different types of deconvolution on stacked sections the single trace zero-phase spiking was preferred (Table 4.2).

Zero-phase spiking deconvolution involves the computation of an inverse filter operator in the time domain by the Wiener-Levinson algorithm with the desired output being a spike at zero lag. The filter is actually applied in the frequency domain, the amplitude and phase responses of the filter being found using the Fourier Transform. The amplitude spectrum of the input trace is multiplied by the amplitude response of the filter. However, for zero-phase spiking deconvolution the phase spectrum of the inverse filter is set to zero so that the phase spectrum of the input trace remains unaltered. The output is then transformed back into time domain by the Inverse Fourier Transform, producing a deconvolved seismic

Deconvolution Design

Type	Operator Length (ms)	White Noise (%)	Correlation Window		
			Offset (m)	Start (ms)	End (ms)
Zero-Phase Spiking	10	0.1	23 69	30 55	230 255

Table 4.2: Deconvolution design.

4.2.8 Surface-consistent residual statics

After deconvolution the strong reflection event on un-muted NMO-corrected CMP gathers from profile 04 is evident at 48 ms (Figure 4.26, upper panel). Across the gather, the reflection signal has an undulating appearance, with time jitter between adjacent traces of up to 3 ms. When these gathers are summed together, the signal misalignment between traces will result in destructive interference at high frequencies, and therefore the temporal resolution of the seismic image of the sub-surface geology will be sub-optimal.

The plus-minus field statics solution has removed much of the trace-by-trace variations in travel times through the dry, near-surface materials above the water table. However, the plus-minus solution is imperfect for a variety of reasons, including picking errors on the first breaks, geophone coupling variations, shot coupling deviations, and non-vertical wave propagation.

The jitter can be removed from the seismic dataset by iteratively minimising the difference between the real travel times at each trace within the seismic dataset (Taner et al., 1974). For low fold, low signal-to-noise ratio data such as is common in shallow seismic reflection profiling this approach may not converge to a solution. Maximising the power of the stack in a surface-consistent sense (Ronen and Claerbout, 1985) provides an alternative robust algorithm. The power of a stacked section is a good measure of the data quality.

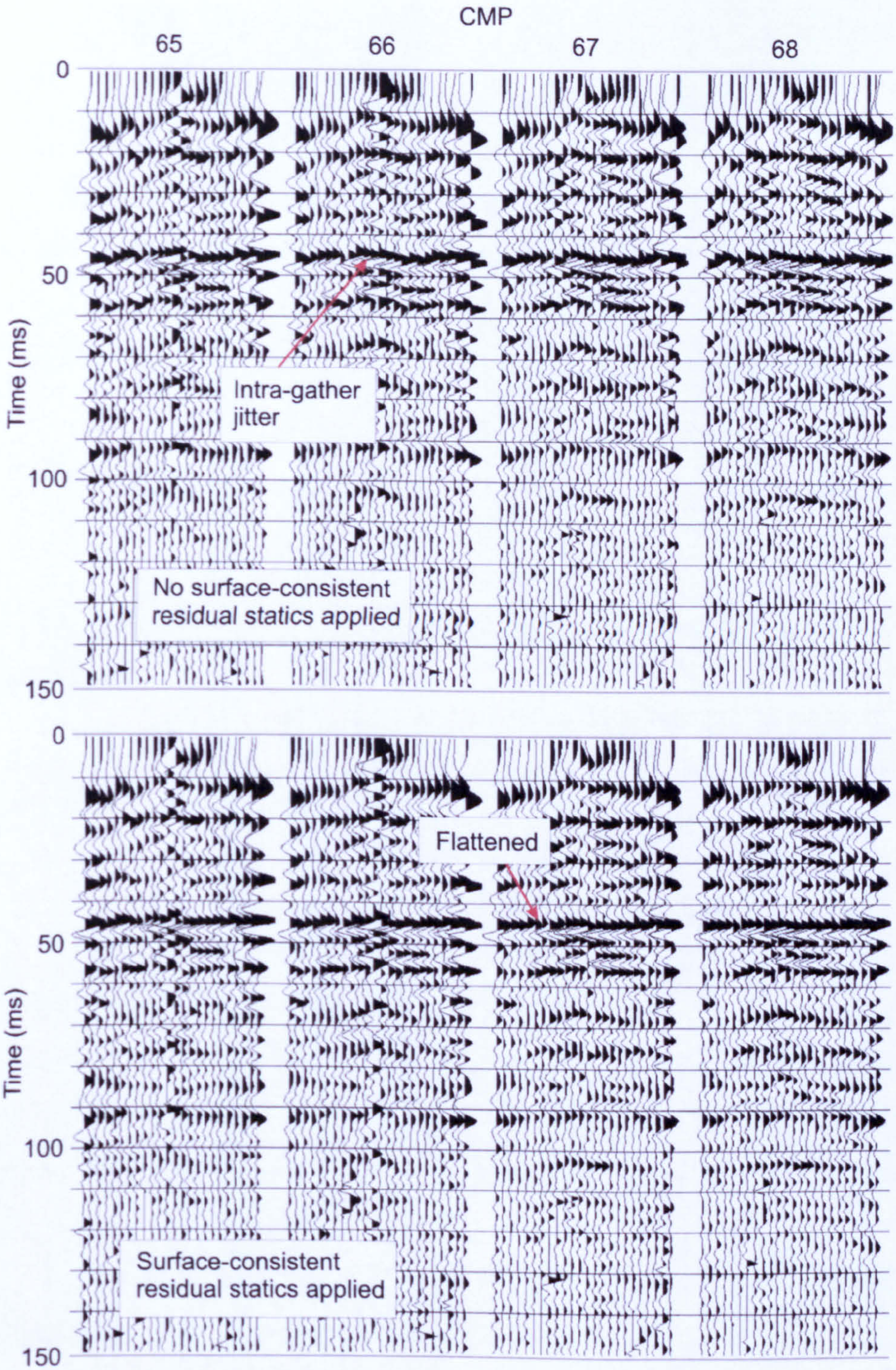


Figure 4.26:QC of the surface-consistent residual statics.
Data are displayed with a scalar multiplier.

The power in a CMP stacked trace is a function of the static shifts applied for every shot and geophone within that particular CMP gather. The highest power for the entire stacked section of a 2D profile could be achieved by testing the effect on the power value of different time shifts on all the individual shot and geophone stations within the stack section. Ronen and Claerbout (1985) used a more efficient approach, building a supertrace F from all the traces within a shot profile in sequence is cross-correlated with another super trace G of all the traces in the relevant part of the stack in sequence without the contribution of that shot. The power of the summed supertraces is expressed by (Ronen and Claerbout, 1985):

$$Power(\Delta t) = \sum_{t} [F(t-\Delta t) + G(t)]^2 \qquad (4.12)$$

Expanding the equation yields a constant term and a cross-correlation term (Ronen and Claerbout, 1985):

$$Power(\Delta t) = \sum_{t} \left| F^2(t-\Delta t) + G^2(t) \right| + 2\sum_{t} F(t-\Delta t)G(t) \qquad (4.13)$$

The algorithm is iterative with the shot and geophone statics adjusted until convergence is achieved. To aid rapid convergence to a solution, the seismic signals used in the cross-correlation calculations were restricted by a user-defined window centred on high quality reflection signal and the maximum time shifts were limited to no more than ±5 ms. Intuitively, a small localised anomaly within the near-surface will only cause a small change in travel time.

At the CMP level (Figure 4.26, lower panel), the reflection events have been flattened out after application of surface-consistent residual statics. However, the improvement in the stacked section for profile 04 is more subtle (Figure 4.27), with the reflection event slightly sharper and improved signal continuity in discrete areas. The inset shows the improvement in data quality that can be achieved by surface consistent residual statics.

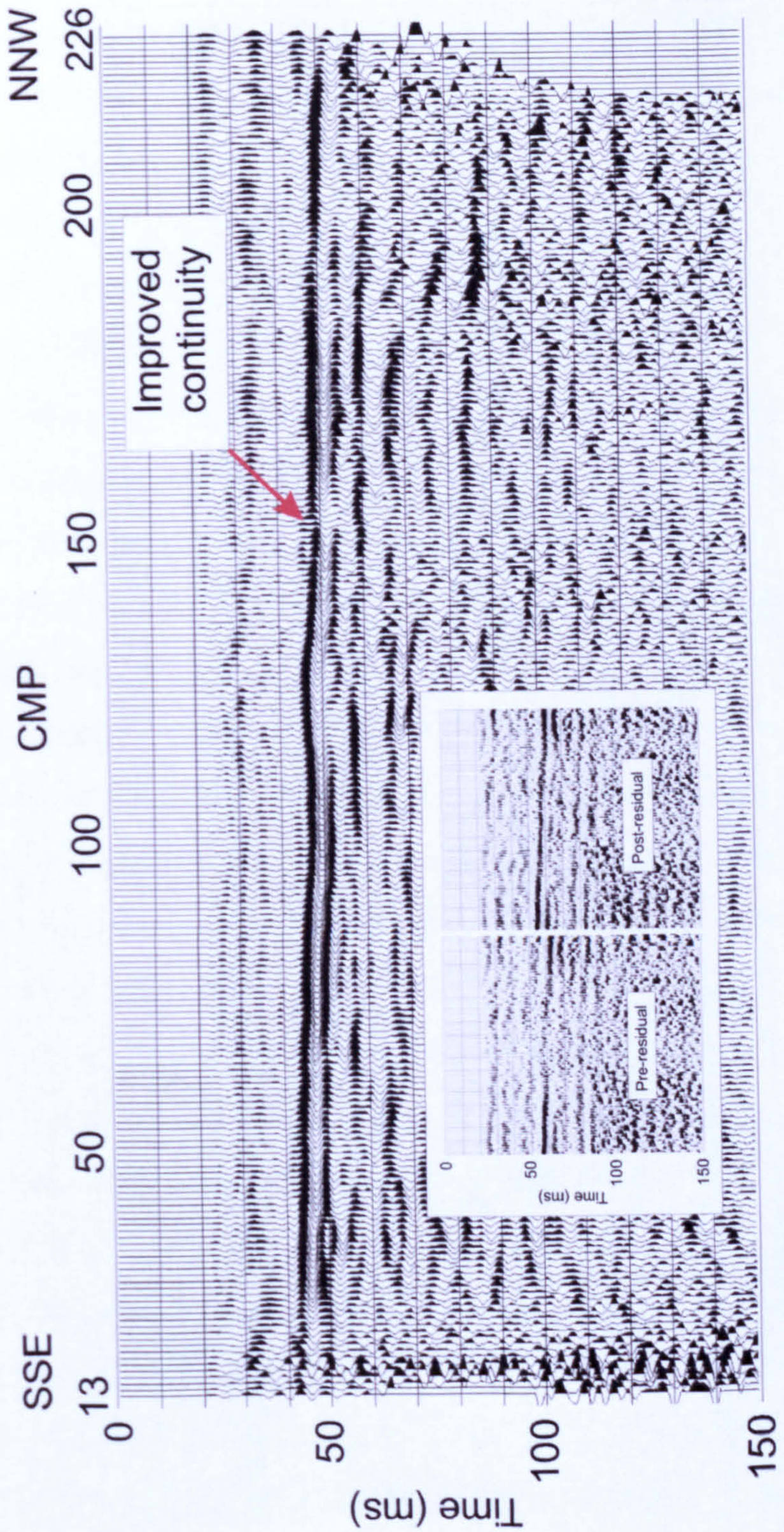


Figure 4.27: Surface-consistent residual statics stack.
Data are displayed with a scalar multiplier.

4.2.9 Remnant noise suppression

In very poor shot coupling conditions remnant spatially aliased ground roll persist even after the application of bandpass filters and mutes designed to suppress shot-generated noise. For Hell Kettles profile 04, these areas are at the very beginning of the profile and beyond CMP 130. On other profiles at Hell Kettles acquired over dry gravelly ground, this noise pollution is of high-amplitude and potentially could migrate into and degrade the reflection signal.

Canales (1984) showed that in the frequency-offset domain the Wiener filter theory can be used to estimate a least-squares approximation of the predictable part of the seismic signal for each particular frequency. The results for all frequencies within the specified bandwidth are then combined and transformed back into the time-offset domain to obtain the filtered stack section. The random noise element of the seismic dataset forms the error in the prediction process is removed.

At Hell Kettles *f-x* deconvolution filtering was designed on NMO-corrected CMP supergathers (Figure 4.28, upper panel) to reduce the remnant noise contamination. NMO flattens the primary reflection signal thereby enhancing the predictable component of the seismic dataset, and increasing the time difference between the seismic noise on adjacent traces, particularly at the far-offsets.

The chosen *f-x* deconvolution filtering parameters were applied to the entire length of the CMP supergather. To reduce the random noise below the reflection events, the *f-x* deconvolution filtering parameters were harsh and significantly degraded the reflection signal. Therefore, the signal that was removed by the filtering was re-introduced in the upper 120 ms of the dataset. This procedure is called addback. The lower edge of the addback window was tapered to create a smooth transition between the areas where the *f-x* deconvolution filtering was not in operation and where the filters were fully applied. The remnant seismic noise has been reduced on the CMP supergather (Figure 4.28, lower panel), with a similar reduction in background noise below the reflection events in the stacked section of profile 04 (Figure 4.29).

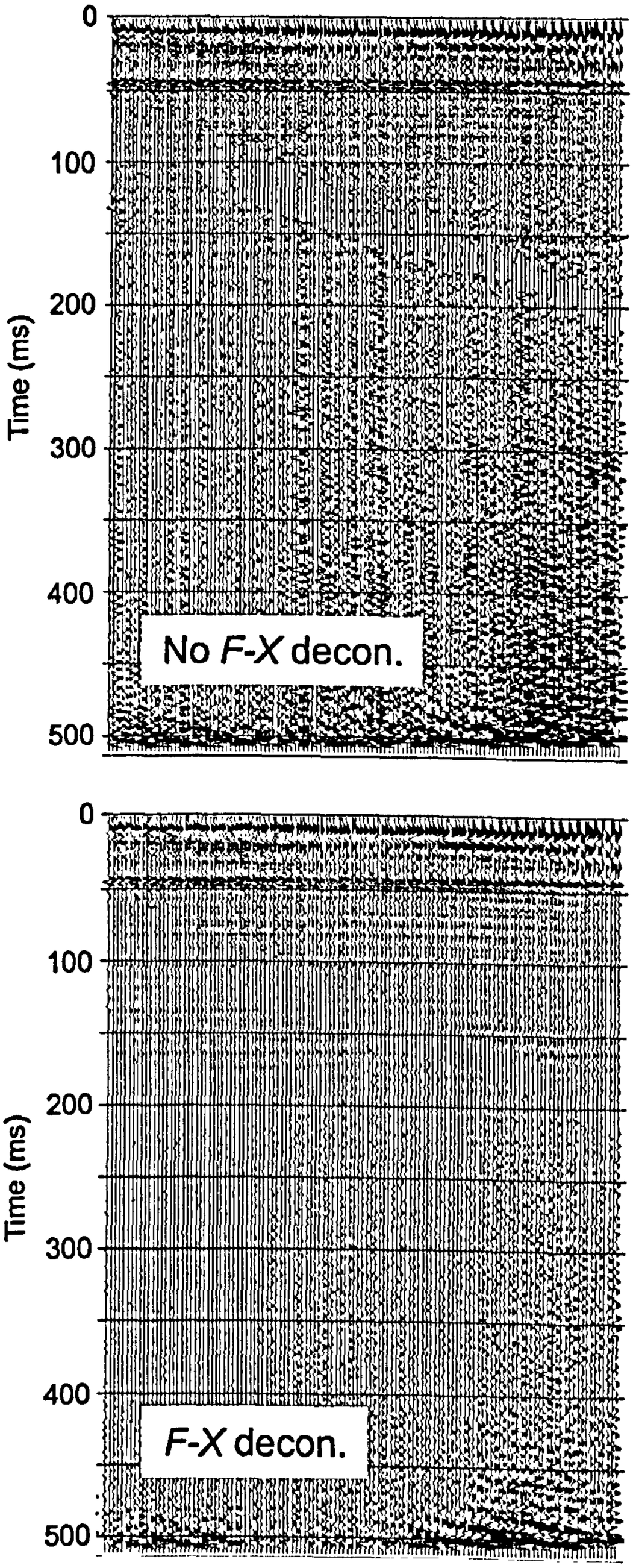


Figure 4.28:QC of the *f-x* deconvolution filtering on a CMP supergather. Data are displayed with a scalar multiplier.

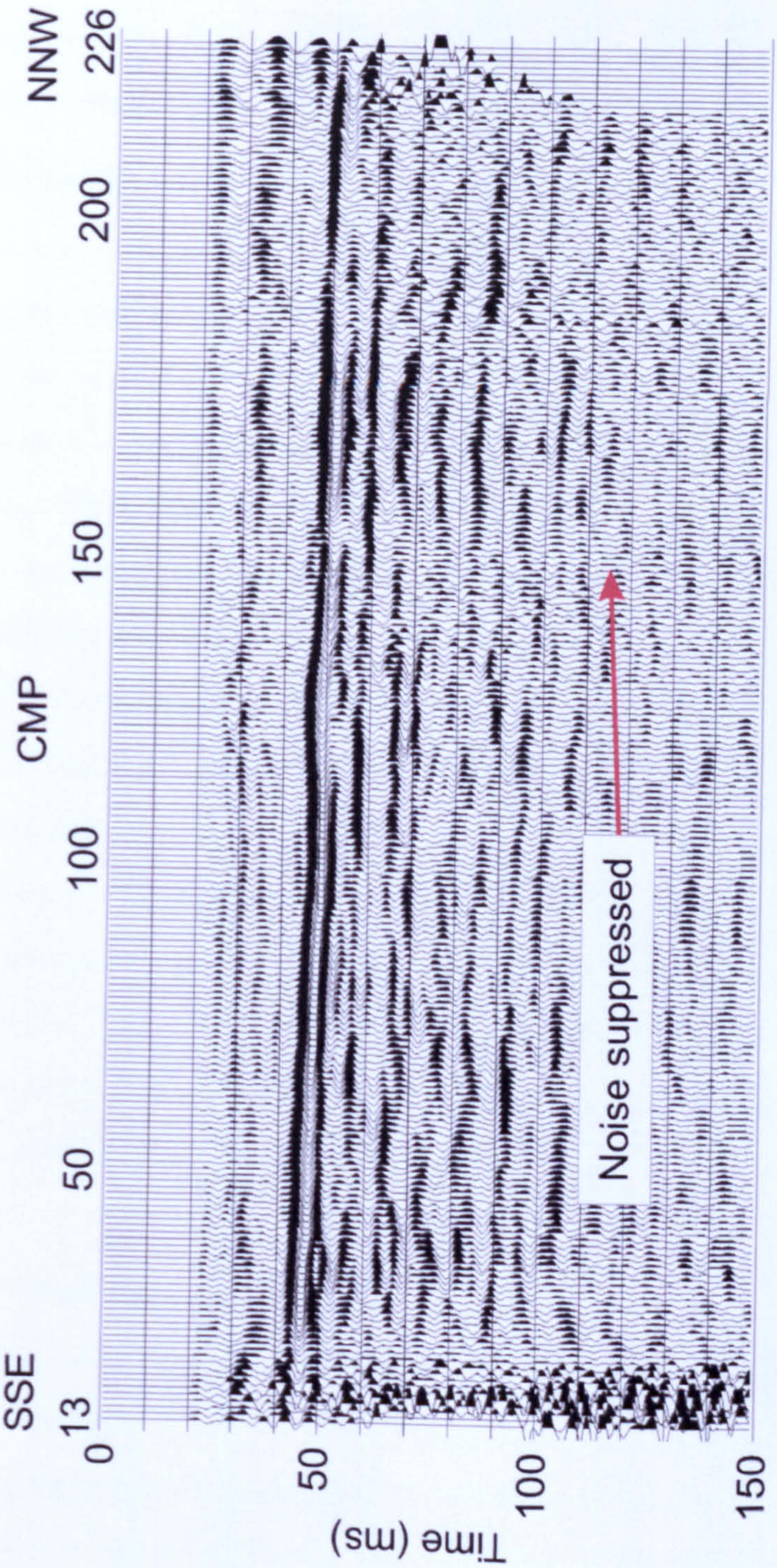


Figure 4.29: *F-X* deconvolution stack.
Data are displayed with a scalar multiplier.

4.2.10 Stack

The stacking of the NMO corrected CMP gathers is a simple but effective process to enhance the signal of the primary reflection signal relative to random background noise. The maximum improvement obtainable is $\sqrt{N}$, where N is the number of traces within the CMP gather. Stacking can also suppress multiples by weighting each trace within the CMP gather appropriately. For Hell Kettles profile 04, each trace within the CMP gather has equal weighting with the mean of the amplitudes calculated in the summation of the traces.

Flattening the primary reflection events before stacking with NMO corrections causes stretching of the reflected wavelets in CMP gathers (Dunkin and Levin, 1973), particularly at the far-offsets where the NMO is greatest, resulting in lowering of the frequency content of the reflection signal. Any excessively stretched seismic signal must be removed to prevent the degradation in resolution of the final stacked product. The mute design in the CMP domain must also exclude refracted energy, which could be construed as a reflection event if included in the stacking process.

The design of the CMP mute for profile 04 after a final pass of interactive velocity analysis provides the last tuning of the stack section. A shallow reflection event at 30 ms TWT running sub-parallel to the main gently dipping reflector between CMP 40 and CMP 120 has been enhanced (Figure 4.30). The inset shows the change in data quality for a particular CMP gather through the digital data processing flow for profile 04.

4.2.11 Time migration

The last major step in the data processing flow (Figure 4.31) of Hell Kettles profile 04 is time migration, which performs several functions. Dipping reflectors are steepened, moved up dip and re-positioned to their true sub-surface location. Diffracted energy is collapsed back to its origin, whilst random noise is suppressed. Migration improves the spatial resolution of the data.

ProMAX seismic processing software has a number of time migration algorithms available for the user to test and contrast. Yilmaz (2001) gives an in-depth comparison of the capabilities of different time migration routines.

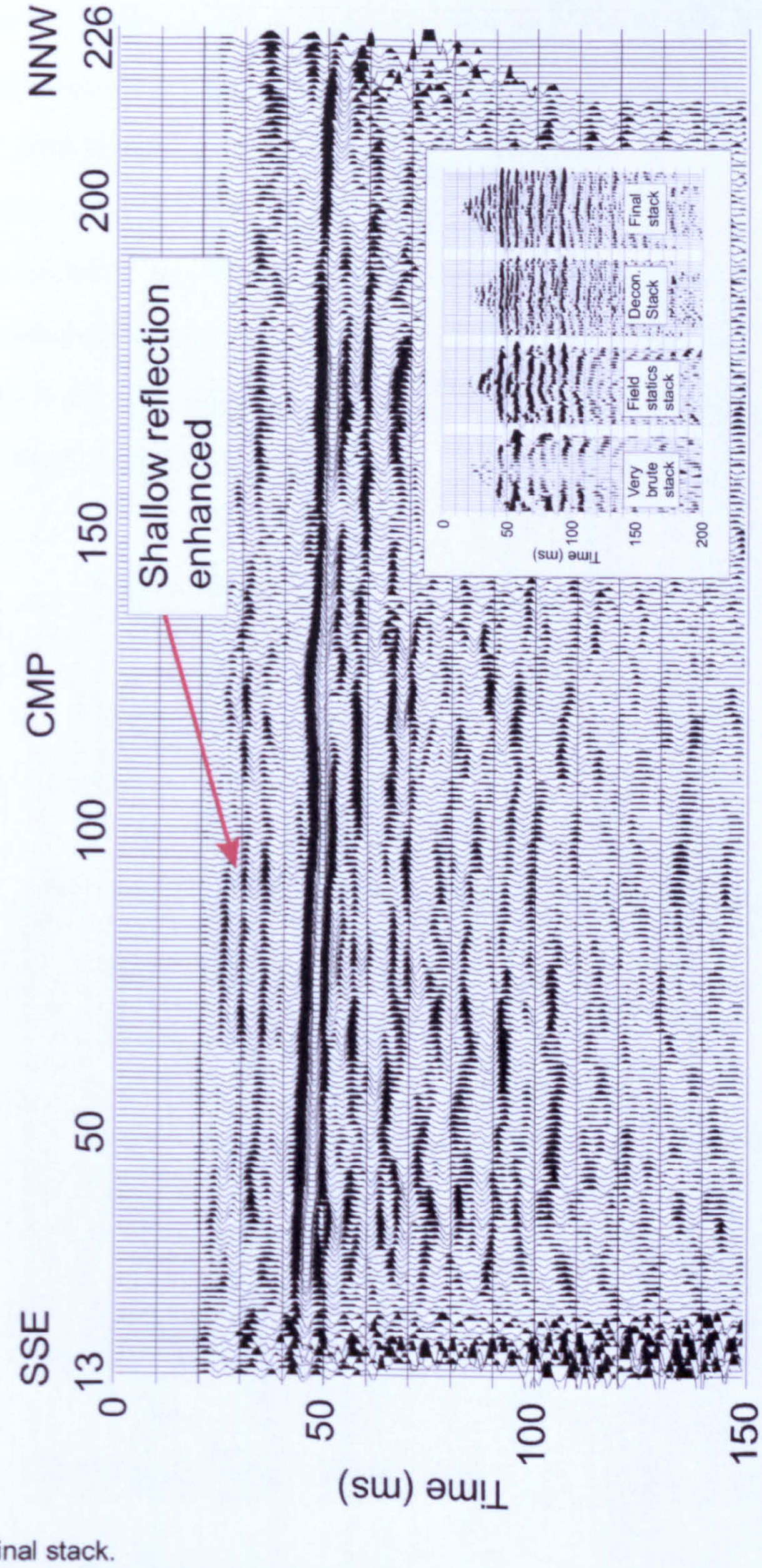


Figure 4.30: Final stack.
Data are displayed with a scalar multiplier.

Kirchhoff time migration sums the amplitudes of the seismic data over hyperbolic trajectories for a given velocity field. Corrections are also made for the variations in amplitude, phase and spherical spreading. Kirchhoff can handle steeply dipping structures and a

moderately varying velocity field. Parameters that need to be specified are the aperture width in traces and the maximum dip in milliseconds per trace. If the sub-surface geological structure is complex, too small an aperture width and too shallow a maximum dip will smear the data. Too large an aperture width may cause random noise in the deep section to invade the good shallow data, particularly in data with poor signal to noise ratio.

Finite difference time migration algorithms are based on the downward continuation of the scalar wavefield. Smaller depth size steps, limited by sampling rate, normally produce the best results. Finite difference time migration is capable of handling highly variable velocity fields, but computer generated dispersive noise is a common side effect.

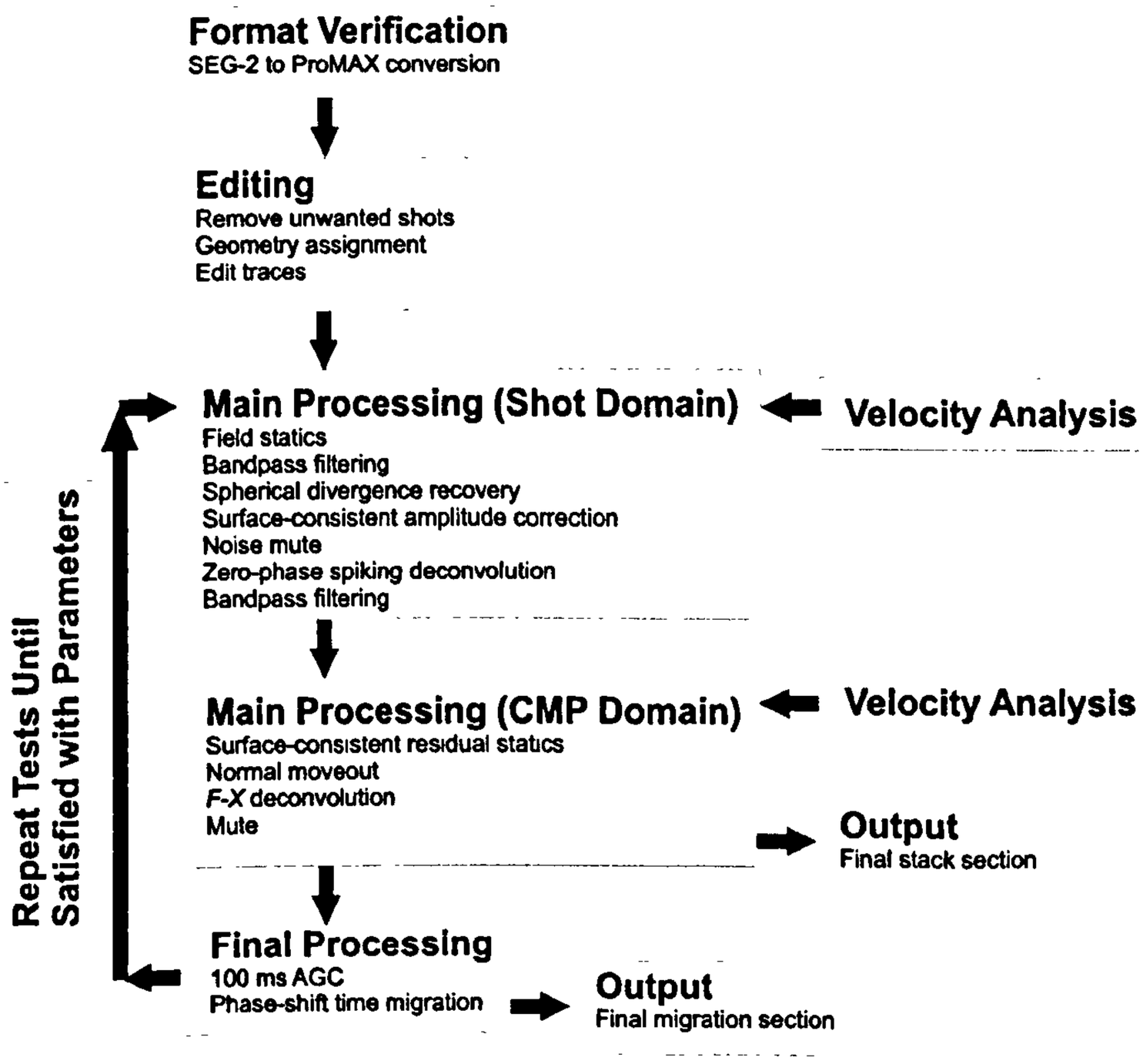


Figure 4.31: Hell Kettles survey seismic data processing flow.

The downward continuation of the scalar wavefield can also be performed in the frequency-wavenumber domain. The phase-shift algorithm generates a clean semi-circular impulse and can handle steep dips, but only gives a stable output for a vertically changing velocity field. The Stolt time migration method is further restricted by the assumption of a constant velocity medium. However, this unrealistic model of the Earth can be partially

redressed by extending the stacked section in the time direction by a variable stretch factor to simulate a vertical velocity gradient.

The true dip of a reflecting surface $\Delta\tau/\Delta x$, and the horizontal displacement d_x and vertical displacement d_t due to post-stack time migration of a point on the reflecting surface can be estimated from the equations of Chun and Jacewitz (1981):

$$d_x = \frac{v^2 t}{4}\frac{\Delta t}{\Delta x} \tag{4.14}$$

$$d_t = t\left[1-\sqrt{1-\left(\frac{v}{2}\frac{\Delta t}{\Delta x}\right)^2}\right] \tag{4.15}$$

$$\frac{\Delta\tau}{\Delta x} = \frac{\Delta t}{\Delta x}\frac{1}{\sqrt{1-\left(\frac{v}{2}\frac{\Delta t}{\Delta x}\right)^2}} \tag{4.16}$$

For Hell Kettles profile 04, the main reflector is at about 50 ms, has an apparent dip $\Delta t/\Delta x$ of 10 ms over 213 m, and the stacking velocity v is 2000 m s^{-1}. For these values, the expression $(v\Delta t/2\Delta x)^2$ is very small; therefore, negligible change in the vertical displacement and the dip of the reflection horizon for profile 04 by time migration is predicted. Post-migration horizontal adjustment of a point on the reflection surface is expected to be no more than 2 m, or two CMP positions.

The geology along profile 04 is a gently dipping structure with an associated smooth, slowly changing velocity field, and therefore is suitable for the phase-shift time migration. It was found that running a 100 ms AGC sliding window over the stacked section prior to time migration gives an improved outcome.

As predicted from the Chun and Jacewitz (1981) equations, the shape of the main reflection surface across profile 04 (Figure 4.32) is altered very little by time migration. Small details on the surface of the reflecting surface have been enhanced; the horizontal resolution

has increased, whilst remnant noise, particularly in the low fold edges of the profile, has been removed.

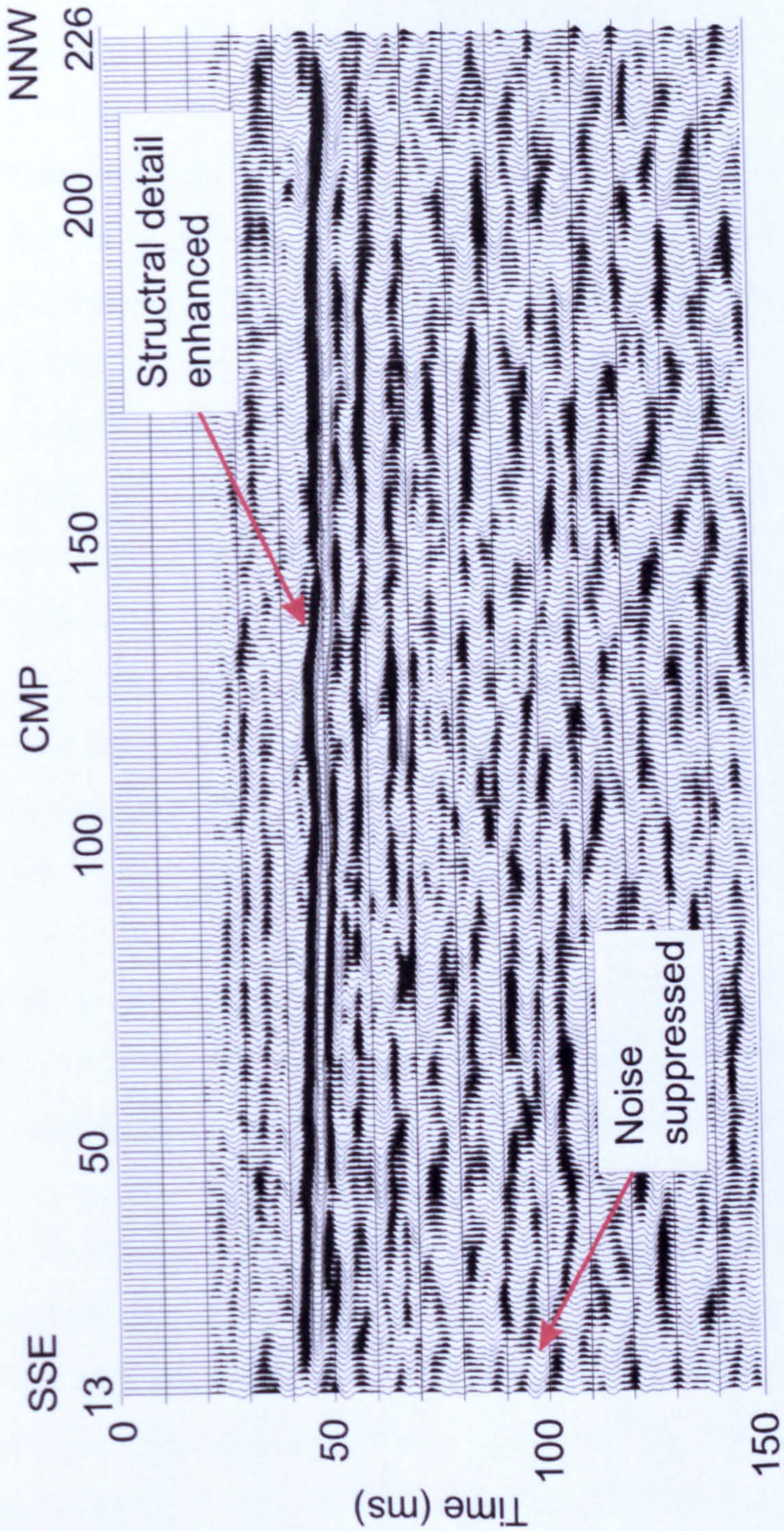


Figure 4.32: Final time migrated stack.
Data are displayed with a scalar multiplier.

4.3 Hell Kettles 3D seismic processing

To ensure that the character of the seismic image of the sub-surface shallow geology in the final stack and time migrated 3D volumes were consistent with the 2D profiles at Hell Kettles, the algorithms and processing sequence applied to the 3D datasets were the same as those applied to the 2D profiles. Only the acquisition geometry, field statics, surface-consistent residual statics, velocity analysis, the suppression of noise by *f-x* deconvolution and the time migration processes were performed in a 3D sense. Bandpass filtering, gain balancing, deconvolution and muting were again carried out on individual shot or CMP gathers.

At Hell Kettles the 3D survey was acquired with a symmetric split-spread shooting template with a geophone spacing of 4 m and a near offset of 26 m (Figure 4.33), with the receiver stations laid out on a 4 m by 4 m grid. The shot stations were on an 8 m by 8 m grid and offset by 2 m from the receiver station grid in both in-line and cross-line directions (Figure 4.34). However, the regular shot station pattern was modified to build the fold of coverage quickly at either end of the in-line direction of the 3D survey. Also, two lines with shot points at intervals 4 m were built into the survey design so that a comparison between 2D and 3D data acquisition and processing could be made. The basic shooting pattern was rolled along each line within the grid of receiver stations, creating a 3D seismic volume of a series of 64 closely spaced 2D profiles.

The basic processing geometrical unit in a 3D seismic volume is the bin. In the ProMAX seismic processing software a bin can be defined as any size. Each 3D survey has a natural bin size which is defined by the acquisition arrangement. At Hell Kettles the natural bin size is a 2 m by 2 m with a maximum of 6 sub-surface hits expected to fall within each bin. Expanding the bins to a larger size would result in more hits being captured within each bin, but trace spacing will increase, potentially decreasing resolution and incurring spatial aliasing. ProMAX demands that the in-line and cross-line grid structure follows a right-handed convention, using the eastings and northings of the national grid reference or an arbitrary user defined co-ordinate system. Quality control of the 3D geometry is achieved by interrogating the raw values in the database, checking the offset and azimuth distribution of the hits within each bin, and displaying the fold of coverage graphically.

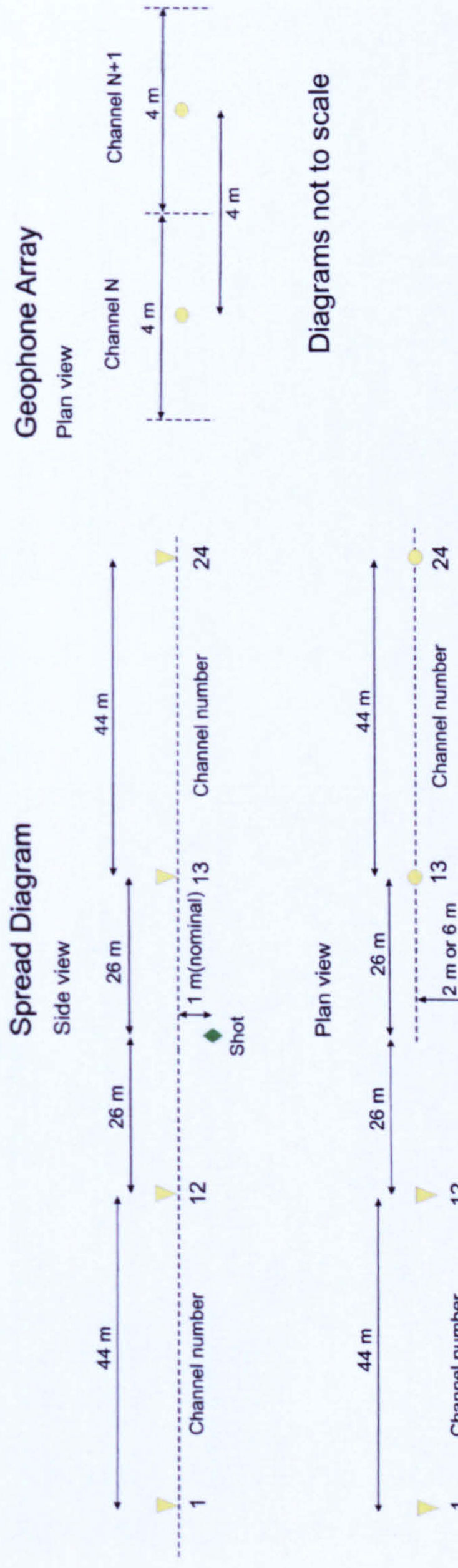


Figure 4.33: Hell Kettles 3D seismic volume shooting template.

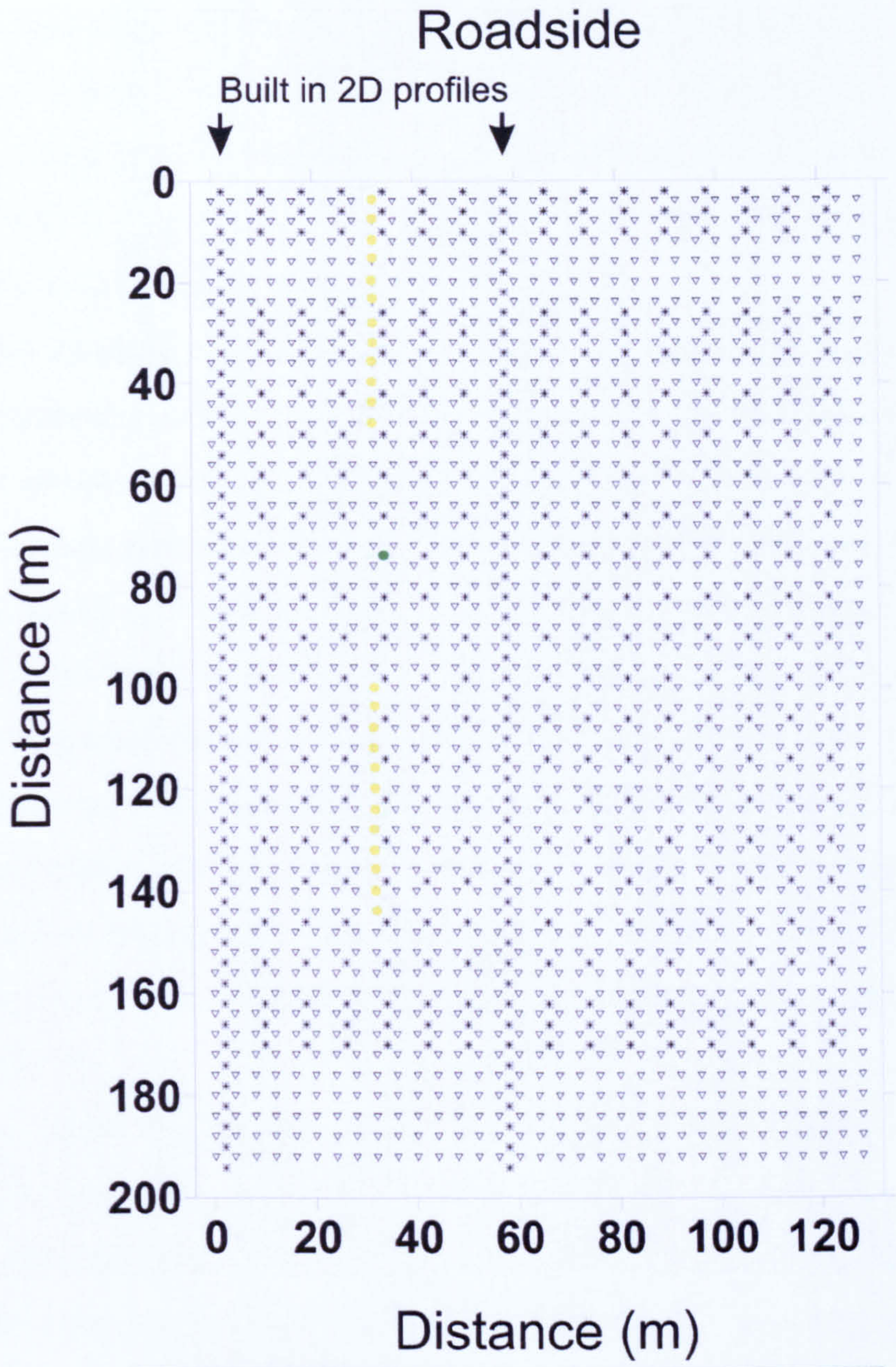


Figure 4.34: Hell Kettles 3D seismic volume shot and receiver station layout.

When the field statics on the 2D in-lines within the Hell Kettles 3D dataset are computed independently, the pattern of the receiver field static corrections across the survey is crossed by a series of linear striations (Figure 4.35, upper panel). The reason for this acquisition footprint is that the refractor velocity varies from in-line to in-line by some tens of metres per second (Figure 4.36). This variation fed through the plus-minus calculations, causing sharp inline deviations in the field statics of up to 3 ms.

These deviations may be resolved by surface-consistent residual statics at a later stage in the processing sequence. However, it was decided to subdue the acquisition footprint by fixing the refractor velocity across the whole survey as the mean of all the in-line refractor velocities. Secondly, each of the in-line 2D profiles making up the 3D volume has associated forward and reverse cumulative time graphs used in the plus-minus computations. Summed together they form two 2D matrices, one for the forward travel cumulative time graphs, and one for the reverse cumulative travel time graphs. A very light blurring filter in the form of a 5-sample running mean with equal cell weights was run across the cross-line line direction of the matrices further smoothing out the jumps between adjacent in-line 2D profiles of the Hell Kettles 3D volume. This approach reduced the linear striations (Figure 4.35, lower panel) with only minimal impact on real deviations in the field statics caused by local variations in near-surface conditions.

The ProMAX max-power surface consistent residual statics algorithm is the best residual statics process to use for the very low fold, low signal-to-noise ratio Hell Kettles 3D dataset. Quality control of the residual statics solution was made by a visual inspection of the CMP gathers, CMP supergathers and stacked section before and after application of the residual statics solution

For 3D seismic processing interactive velocity analysis was performed on CMP supergathers which comprised nine CMP gathers. Eight immediately neighbouring gathers were included in the supergather around a central CMP gather located at the specified velocity analysis point. The individual velocity analysis points were chosen at regular intervals in-line and cross-line across the 3D grid. Similarly, CMP supergathers built from clusters of nine CMP gathers were used to suppress excessive background noise by passing an *f-x*

deconvolution filter passing over the CMP supergathers. The time migration phase-shift algorithm used in processing the Hell Kettles 2D profiles was applied in 3D mode.

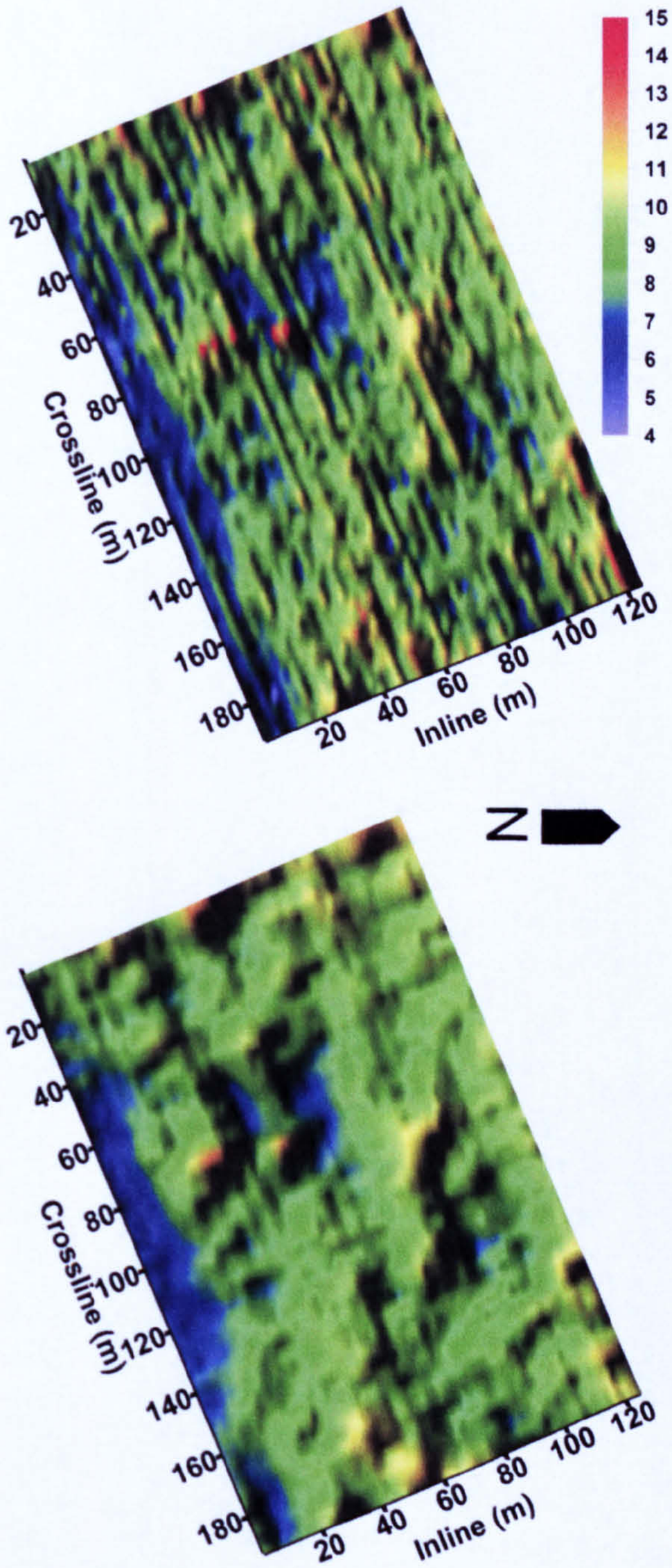


Figure 4.35: Reduction of the acquisition footprint in 3D receiver statics.

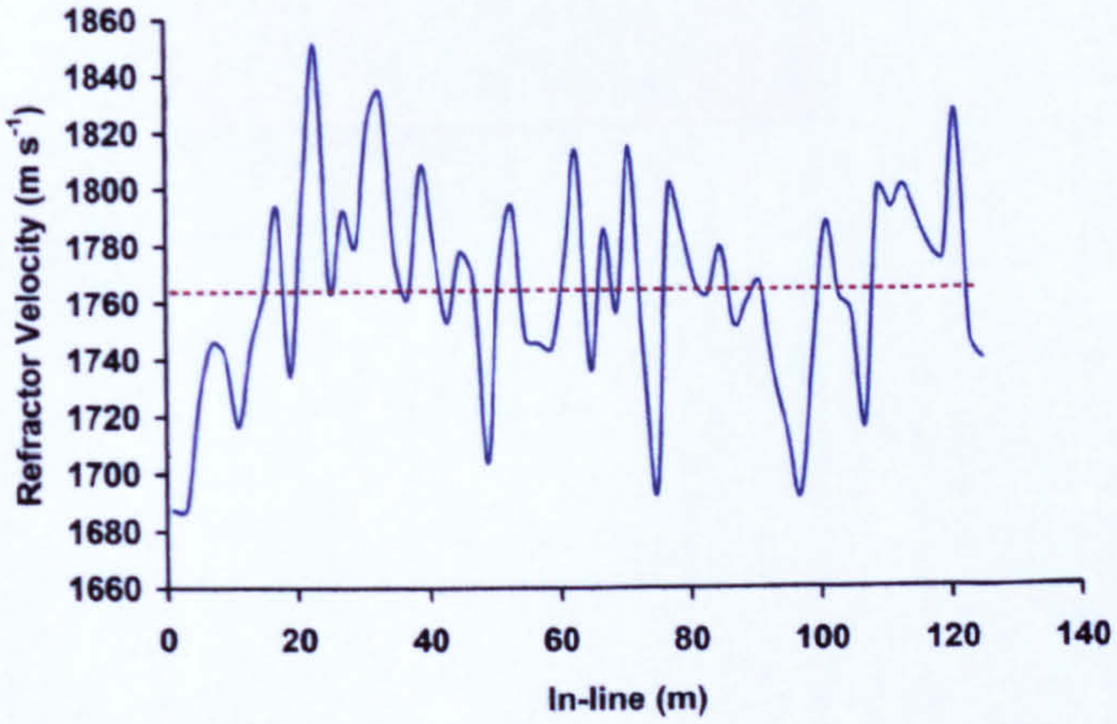


Figure 4.36: Individual 3D Sub-line refraction velocities.